RESEARCH STUDY ON MATERIALS PROCESSING IN SPACE EXPERIMENT M512

DRAFT

FINAL REPORT

By

M.R. Brashears
S.J. Robertson

1 December 1973

Prepared under Contract No. NAS8-28729

Lockheed Missiles & Space Company, Inc.
Huntsville Research & Engineering Center
Huntsville, Alabama

For

NASA-GEORGE C. MARSHALL SPACE FLIGHT CENTER

FOREWORD

This final report summarizes the results of the overall performance of Contract NAS8-28729. This effort was performed by personnel in the Fluid Mechanic Applications Group of the Lockheed-Huntsville Research & Engineering Center for NASA-Marshall Space Flight Center.

The work was performed under the direction of E. A. Hasemeyer (M553) and R. M. Poorman (M551) of NASA-MSFC S&E-PE-MW and S&E-ASTN-MM, respectively.

RESEARCH STUDY ON MATERIALS PROCESSING IN SPACE EXPERIMENT M512

FINAL REPORT

By

M. R. Brashears

and

S. J. Robertson

Lockheed Missiles & Space Company, Inc.
Huntsville, Alabama

ABSTRACT

A study program was conducted to clarify the role of gravity in the fluid mechanics of certain molten metal processes of potential significance to manufacturing in space. In particular, analyses were conducted of the M551 Metals Melting Experiment and the M553 Sphere Forming Experiment to be conducted in the M512 Facility onboard Skylab. The M551 experiment consisted of a study of electron beam welding of various metals, and the M553 experiment studied the formation of molten metal spheres by free-floating in a near zero-gravity environment. The analyses of these experiments and a comparison with ground-based and KC135 experimental results are presented.

TABLE OF CONTENTS

LIST OF ILLUSTRATIONS

LIST OF TABLES

NOMENCLATURE

Symbol	Definition
A	Area, Maximum Amplitude
a	Amplitude, Acceleration
B	Magnetic Induction
C	Constant $\propto r\mu$, Heat Capacity
C_p	Specific Heat at Constant Pressure
D	Diameter
d	Differential Operator, Cavity Depth
E	Electron Energy, Electric Field Intensity
e	Base of Natural Logarithms, Charge on Electron
F	Force
f	Frequency
g	Acceleration of Gravity
I	Electron Current
J	Electrical Current Density
K	Constant $\propto \sigma$
k	Thermal Conductivity, Boltzmann Constant
M	Mass
M_w	Molecular Weight
m	Molecular Mass
$\dot{m}$	Mass Flux Due to Evaporation

NOMENCLATURE (Continued)

Symbol	Definition
N_i	Mole Fraction of Component i
$\vec{n}$	Unit Normal Vector
n_i	Moles of Component i
P	Pressure
P_{eb}	Electron Beam Power
P_v	Vapor Pressure
p	Partial Pressure
$\dot{Q}$	Rate of Internal Heat Generation
q	Heat
$\vec{q}$	Heat Flow Vector
$\dot{q}$	Rate of Heat Flow
$\dot{q}_c$	Power Loss Due to Conduction
$\dot{q}_i$	Power Loss Due to Ionization and Excitation of Evaporated Atoms
$\dot{q}_r$	Power Loss Due to Radiation
$\dot{q}_v$	Power Loss Due to Vaporization
$\dot{q}_{loss}$	Total Power Loss
R	Universal Gas Constant, Universal Electron Range
$\vec{R}$	Positional Vector
r	Radius
S	Strouhal Number
S_c	Spreading Coefficient

NOMENCLATURE (Continued)

Symbol	Definition
T	Temperature
T_M	Melting Point
t	Time
V	Volume, Voltage
$\overline{V}$	Average Molecular Velocity
$\vec{V}$	Velocity Vector
v	Velocity
v_e	Velocity of Electron
W	Work of Adhesion
x	Longitudinal Distance from Datum Plane
y	Lateral Distance from Datum Plane
z	Vertical Distance from Datum Plane

GREEK LETTERS

α	Thermal Diffusivity
γ	Fraction of Radiation Escaping from Electron Beam Hole
∇	Grad or del Operator
∂	Partial Differential Operator
ϵ	Emissivity (Radiation)
θ	Contact Angle
λ	Latent Heat of Phase Change
λ_f	Latent Heat of Fusion

NOMENCLATURE (Concluded)

Symbol	Definition
μ	Viscosity
ρ	Density
σ	Surface Tension, Stefan-Boltzmann Constant
σ_{LV}	Surface Energy at Liquid-Vapor Interface
σ_{LS}	Surface Energy at Liquid-Solid Interface
σ_{SV}	Surface Energy at Solid-Vapor Interface
φ	Phase Angle
ω	Angular Velocity

SECTION I. INTRODUCTION

Lockheed-Huntsville began work in May 1972 to assist the National Aeronautics and Space Administration, Marshall Space Flight Center, in meeting the objectives of the M551 Metals Melting Experiment and the M553 Sphere Forming Experiment to be conducted in the M512 Facility aboard the Skylab Laboratory. Specifically, ground-based studies have been conducted with the objectives of clarifying the effects of gravity and optimizing the experiments within the constraints of existing hardware. All process phenomena have been considered with particular attention given to adhesion-cohesion studies with emphasis on the fluid dynamics of the molten metal. Detailed thermal histories have been generated for the three-dimensional specimen geometry including radiation, conduction and vaporization losses with allowances for variable properties. In addition, quantitative techniques have been used to establish the gravitational level (magnitude and direction) for KC-135 aircraft flights and the actual Skylab mission for both experiments.

The overall study is composed of three distinct portions, Phase A – the preparation of a ground base study plan, Phase B – the performance of the study plan, and Phase C – the analysis of experimental flight data. This final report documents the results of the overall effort.

The M551 Metals Melting Experiment consisted of a rotating metal disk mounted perpendicular to an electron beam (eb) heat source with the eb impingement point located 6 cm from the center of rotation. The velocity of the beam relative to the impingement point was 1.61 cm/sec with a corresponding radial acceleration of $5.09(10)^{-4}$g. The eb was focused to approximately 0.15 cm diameter. The three materials listed below were used in the experiment.

- 2219 Aluminum
- 321 Stainless Steel
- Tantalum.

The thickness of the material varies with angular position around the disk.

The M553 experiment consisted of two 15-specimen indexing pinwheels mounted perpendicular to the electron beam. With each discrete rotation of the pinwheel a new cylindrical specimen was positioned in the path of the electron beam. As the specimen melted, the hardware was designed to allow for deployment of the resulting liquid spheres with the ensuing free-float time giving rise to a containerless solidification in the vacuum chamber.

Before presenting specific calculations and experimental results relating to the M551 and M553 experiments, a brief discussion of some fundamental concepts will be presented (Section II). Specific attention will be given the M551 experiment in Section III, while Section IV is devoted to the M553 experiment.

SECTION II. FUNDAMENTAL CONCEPTS

This section reviews some of the fundamental concepts pertinent to the M551 and M553 experiments. Specific calculations relative to either the M551 or M553 experiment are presented in Sections III or IV, respectively.

A. MECHANISMS OF POWER LOSS

The distribution of eb power can be described by the following equation:

$$\dot{q}_{loss} = \dot{q}_v + \dot{q}_c + \dot{q}_r + \dot{q}_i \tag{1}$$

where

$\dot{q}_v$ = power loss due to vaporization

$\dot{q}_c$ = power loss due to heat conduction

$\dot{q}_r$ = power loss due to radiation

$\dot{q}_i$ = power loss due to ionization and excitation of evaporated atoms.

The vaporization loss can be calculated from the Langmuir theory. Here, the mass flux due to vaporization can be calculated from kinetic theory and is equal to

$$\dot{m} = P_v \left(\frac{m_w}{2\pi RT} \right)^{1/2} \tag{2}$$

where

P_v = vapor pressure

M_w = molecular weight

R = universal gas constant

T = temperature.

If more than one component is present, Raoult's law may be used to calculate the equilibrium vapor pressure that is exerted by a component in a solution. This law states that

$$p_a = N_a P_{v_a} = \left(\frac{n_a}{n_a + n_b + n_c + \ldots} \right) P_{v_a} \tag{3}$$

where

p_a = partial pressure components "a" in a solution with, b, c. . .

P_{v_a} = vapor pressure of "a" in pure state

n_a, n_b, n_c = moles for components a, b, c

N_a = mole fraction of "a."

The total vaporization power loss can now be calculated from

$$\dot{q}_v = \sum_{i=1}^{N} \dot{q}_{v_i} = \sum_{i=1}^{N} \int_A \dot{m}_i \left(\frac{\lambda_o + 2RT}{M_w} \right) dA \tag{4}$$

where λ_o is the energy required to vaporize a unit mass at $0^\circ K$ (i.e., the sum of the heat of melting and the heat of vaporization).

A second mechanism of heat loss is due to thermal conduction. This can be obtained (via a thermal analyzer) from

$$\dot{q}_c = \int_A \vec{q} \cdot \vec{n} \, dA \tag{5}$$

where $\vec{q}$ is the heat flow vector and $\vec{n}$ is the surface normal. The term $\vec{q}$ is calculated by

$$\vec{q} = -k \nabla T \tag{6}$$

with T satisfying

$$\nabla^2 T - \frac{1}{\alpha} \frac{\partial T}{\partial t} = \frac{\dot{Q}}{k} \tag{7}$$

where

α = thermal diffusivity

k = thermal conductivity

$\dot{Q}$ = heat generation (source).

The heat loss to radiation can be calculated via the Stefan-Boltzmann law

$$\dot{q}_r = \int_A \epsilon \, \sigma \, T^4 \, \gamma \, dA \tag{8}$$

where

ϵ = emissivity

γ = fraction of radiation differential area dA which escapes from eb hole

σ = Stefan-Boltzmann constant.

The average power lost to ionization and excitation can be calculated from the universal electron range (R) — incident electron energy relationship. This can be written as

$$\frac{dE}{dR} = \text{known constant} \tag{9}$$

The density of the gas in the hole is

$$\rho = \frac{\dot{m}}{A_o \overline{V}} \tag{10}$$

where

A_o = area of cavity

$\overline{V}$ = average molecular velocity.

The energy loss due to ionization and excitation is then

$$\dot{q}_i = I\, d\, \rho \frac{dE}{dR} \tag{11}$$

where

I = current

d = cavity depth.

These mechanisms are shown schematically in Figure 1.

B. ACTIVE FORCES ATTRIBUTABLE TO ELECTRON BEAM

Electron Force

The transfer of electron momentum during impingement on a surface can be equated to the net force on the surface and is given by

$$F_e/A = m_e v_e \frac{J}{e} \tag{12}$$

where

F_e/A = force per unit area

m_e = mass of electron

v_e = velocity of electron

e = charge of electron

J = current density

The velocity can be calculated from

$$v_e = \left(\frac{2eE}{m_e}\right)^{1/2} \tag{13}$$

where

E = acceleration potential.

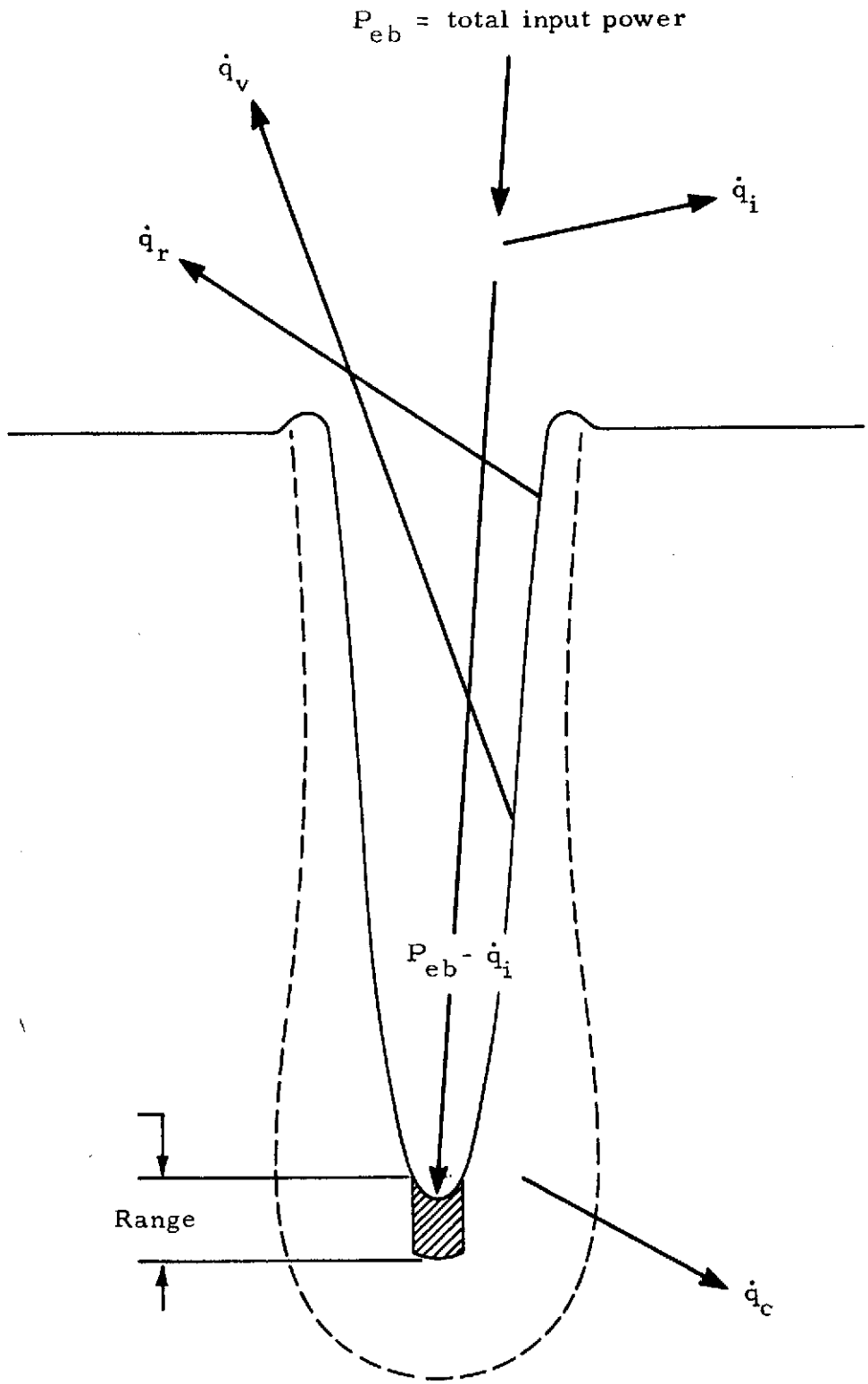

FIGURE 1. THERMAL MECHANISMS

Thus the total force on area A is

$$F_e = I\sqrt{\frac{2m_e E}{e}} \tag{14}$$

with $e/m_e = 5.27(10)^{17}$ stat coulomb/gm.

Vaporization Force

The reaction force of evaporating mass can be calculated from conservation of momentum:

$$F_v/A = \dot{m}\,\overline{V} \tag{15}$$

where

$\overline{V}$ = molecular velocity.

The most probable velocity calculated from a Maxwell-Boltzmann distribution is

$$V_{mp} = \left(\frac{2kT}{m}\right)^{1/2} \tag{16}$$

while the mean speed is given by

$$\overline{V} = \left(\frac{8kT}{\pi m}\right)^{1/2} \tag{17}$$

where

k = Boltzmann's constant

m = molecular mass

The total force can be found by integrating over the surface

$$F_v = \int_A \dot{m}\,(T)\,\overline{V}(T)\,dA\,. \tag{18}$$

If the most probable velocity is used this equation reduces to

$$F_v = \frac{1}{1.775} \int_A P_v(T)\, dA \tag{19}$$

and

$$F_v = \frac{1}{1.57} \int_A P_v(T)\, dA \tag{20}$$

for mean velocity. Thus, given the surface temperature distribution, the total force can be calculated.

Surface Tension Force

The total surface tension force tending to close the cavity can be calculated as the product of surface tension and the circumference of the cavity, i.e.,

$$F = \pi D \sigma \tag{21}$$

where

D = cavity diameter

σ = surface tension.

Hydrostatic Force

One of the three expected differences in zero-g phenomena as compared to one-g is the decrease in hydrostatic pressure exerted by the weight of the molten material on the cavity wall. This is given by

$$F_h/A = \rho g d \tag{22}$$

where

d = depth of cavity.

Thus, the total force is then

$$F_h = \frac{\pi}{4} \rho g d D^2. \tag{23}$$

Electrostatic and Electromagnetic Forces

The electrostatic force due to a net charge on a mass of material (especially low electrical conductors) may be a non-negligible force for both experiments. The magnitude of this force may be estimated for a given charge distribution by calculating the electrostatic body force ($\rho\vec{E}$) and realizing the tendency to negate surface tension effects.

The contribution of magnetostriction and electrostriction effects (i.e., the variation in electrical properties with changes in density due to compression) to the total force may also be estimated if this variation in electrical properties (permittivity and permeability) with density is known. Also, the Lorentz force ($\vec{J} \times \vec{B}$) is a measure of the role of convective charge transport and conduction current of the total force.

In the absence of one predominant body force (gravity) some of the mentioned mechanisms may produce a unique effect and the relative magnitudes should be established to help clarify the effect of the absence of gravity.

C. ADHESION, COHESION AND SURFACE TENSION EFFECTS

The terms cohesion and surface tension are generally used interchangeably while in fact they represent different mechanisms. In discussing the differences between the two, it is necessary to discuss the concept of intrinsic pressure. Intrinsic pressure is generated as a result of the attractive cohesive force producing a compression and, since one is a result of the other, they exist at the same time. It is this intrinsic pressure gradient that defines the range of the effects of surface tension itself as surface tension is the difference between the intrinsic pressure forces and the cohesive forces. This difference is non-zero only near the surface as the cohesive forces are weaker at the surface than they are in the bulk and intrinsic pressure is at a maximum. This situation produces the largest difference at the surface. The general effect of increasing temperature is to superimpose a repulsive force that produces a weakened cohesive force and also reduces the intrinsic pressures. If the cohesive effects are a stronger function of temperature than intrinsic pressure effects, a reduction in the surface tension accompanies an increase in temperature and vice versa. For equal dependence, surface tension would remain constant.

Contact Angle

The equilibrium conditions of a sensible drop in contact with a solid surface have generally been written in terms of surface

tension (i.e., the Young-Dupre' form). One derivation of this form of the equation can be obtained from a force balance at the interfaces (see Figure 2).

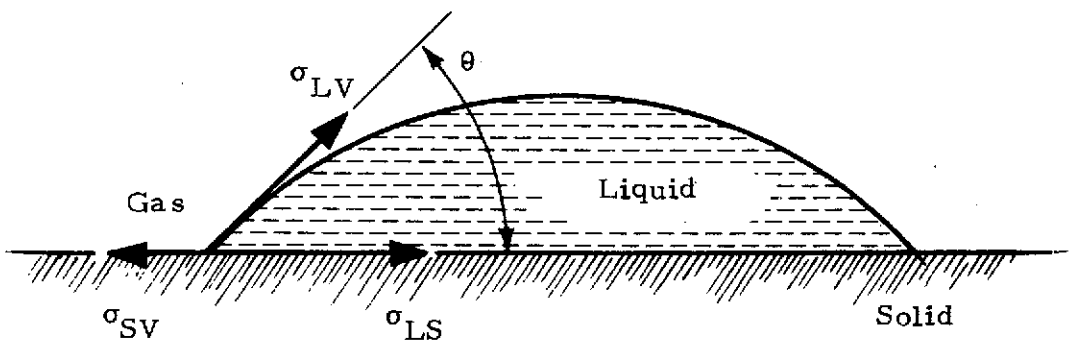

FIGURE 2. CONTACT ANGLE

This yields

$$\sigma_{SV} = \sigma_{LV} \cos\theta + \sigma_{LS} \tag{24}$$

A distinction must be made, however, between surface tension and surface free energy as recognized by Gibbs [1], restated by Shuttleworth [2] and discussed by Pethica and Pethica [3]. Young's equation is frequently used to draw conclusions concerning the surface energy of solids; but as stated it is objectional from a theoretical point of view and refuted by experiment. The main theoretical objection lies in the fact that the vertical component ($\sigma_{LV}\sin\theta$) is not accounted for. Some investigators have argued that it is obvious that this component is balanced by the elasticity of the solid, by gravitation, or by another non-capillary agent. However, if a vertical plate is envisioned (i.e., unaccounted component now horizontal), it is easily seen that this component cannot affect the vertical displacement of the plate. Also it is known from experiment that poorly wetted solid particles float on the surface of a less dense liquid; thus the vertical component cannot be compensated for by $\sigma_{SV} - \sigma_{LS}$ (see Figure 3). These aforementioned sentiments are best described by Bikerman [4], as this discussion denies the validity of Young's equation from a theoretical and experimental point of view. The work of Pethica and Pethica [3] examined the validity of the equation in a gravitational field and it was concluded that the equation is invalid. Others, as pointed out by Johnson [5], deny the validity for zero contact angle. Johnson, however, maintains that Young's equation is indeed valid when surface tensions are used instead of surface free

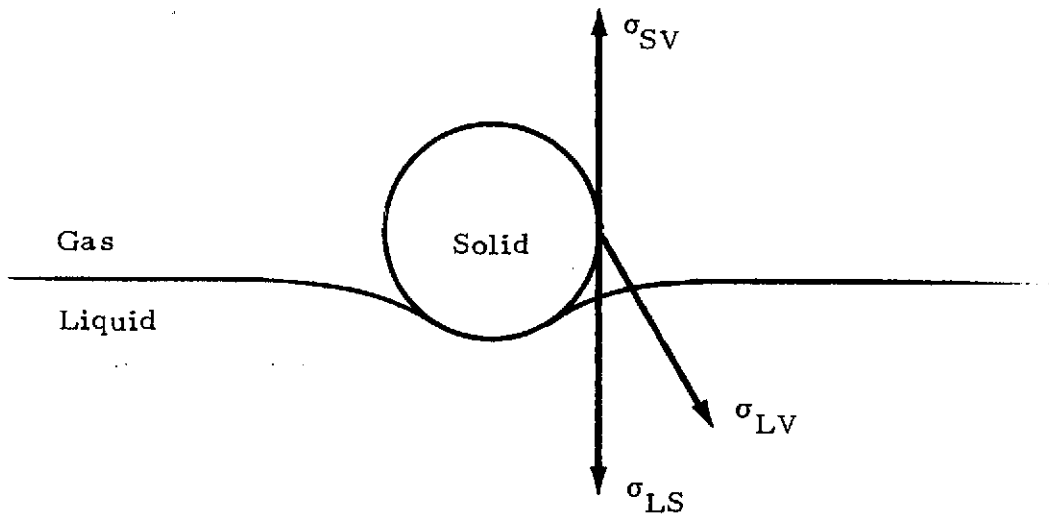

FIGURE 3. "FLOATING" SOLID

energy. He derives relationships based on Gibbsian thermodynamics that include the effects of adsorption and gravity. He also discusses four major reasons that contribute to these discrepancies, i.e.,

- Assumption that surface tension is numerically equal to specific surface free energy
- Conclusion that a necessary and sufficient condition for equilibrium is that the free surface energy of the system be a minimum
- Lack of rigor in defining the differences between surface tensions, surface free energies, specific surface free energies and surface energies, and
- Interpretation of σ as applied to solids.

Johnson then clarifies the above misconceptions and derives an equation that represents total mechanical equilibrium from which Young's surface tension equation results. In support of Johnson's work is the work of Li [6]. Here the Young equation is shown to be a terminal condition of an isoperimetric problem derived from the principal of minimum energy. It is also shown that the contact angle is constant for all gravitational field levels. This concept will be employed to examine the adhesion and cohesion effects in the M551 and M553 experiments.

Spreading and Wetting

The spreading of a liquid on a substrate has classically been defined as the energy released per unit area when the liquid with a free surface spreads over the solid. The spreading coefficient is given by

$$S_c = \sigma_{SV} - \sigma_{LS} - \sigma_{LV} \tag{25}$$

or by

$$S_c = \sigma_{LV} (\cos\theta - 1) \tag{26}$$

if Young's equation is substituted. If $S_c \leq 0$ the liquid will assume the shape of a spherical segment (no external forces) with the area of contact given by

$$A = \frac{\pi^{1/3} \sin^2\theta \, V^{2/3}}{(1 - \cos\theta)^{4/3} \left(\frac{2 + \cos\theta}{3}\right)^{2/3}} \tag{27}$$

where

V = volume of the liquid.

On the other hand, if $S_c > 0$, the liquid will spread over the solid surface at a rate dependent upon the viscosity of the liquid and the surface roughness.

Work of Adhesion

Dupre' introduced the concept of reversible work of adhesion of liquids to solids and this relation can be written as

$$W = \sigma_{SV} + \sigma_{LV} - \sigma_{LS} \tag{28}$$

This equation is simply the thermodynamic expression of the fact that the change in free energy of a system is equal to the work needed to separate the liquid from the solid.

D. LIQUID DYNAMICS

Formation Time

The question of the time needed for minimum energy formation has received considerable attention and is reviewed here to document how the calculations have been made.

Consider a mass of liquid whose motion can be described by the full Navier-Stokes equations as given below:

$$\rho \frac{D\vec{V}}{Dt} = \vec{F} - \nabla P + \mu \nabla^2 \vec{V} \tag{29}$$

Performing an order of magnitude analysis with

$$\begin{aligned} V &= O(r/t) \\ D/Dt &= O(1/t) \\ F &= O(\sigma/r)/r \\ \nabla &= O(1/r) \\ \nabla^2 &= O(1/r^2) \end{aligned} \tag{30}$$

and keeping track of the resisting and forming forces yields

$$\rho O(r/t^2) = \frac{O(\sigma/r)}{r} - O(P/r) - \mu\ O(1/rt) \tag{31}$$

or

$$O(\rho r/t^2) = O(\sigma/r^2) - O(\mu/rt) \tag{32}$$

as

$$O(P/r) = O(2\sigma/r^2). \tag{33}$$

Rearranging yields

$$O(\sigma t^2) - O(\mu rt) - O(\rho r^3) = 0\ . \tag{34}$$

Thus

$$t_f = O(t) = \frac{\mu r \pm \sqrt{\mu^2 r^2 + 4\sigma\rho r^3}}{2\sigma} \tag{35}$$

where t_f is the time to formation. For low viscosity liquids such as liquid metals, Eq. (35) can be simplified to

$$\lim_{\mu \to 0} t_f = \lim_{\mu \to 0} \frac{\mu r \pm \sqrt{\mu^2 r^2 + 4\sigma \rho r^3}}{2\sigma} \tag{36}$$

or

$$t_f' = \sqrt{\frac{4\sigma \rho r^3}{4\sigma^2}} = \sqrt{\frac{\rho}{\sigma}}\ r^{3/2} \tag{37}$$

where t_f' = time to formation of inviscid fluid.

Damping Time

After formation, the sphere will continue to oscillate around its minimum energy position due to inertial effects. These oscillations are reduced as a function of time as a result of internal friction due to a non-zero viscosity.

Consider a system of mass M freely oscillating about its equilibrium position. Further, it is reasonable to assume a constraining force coefficient proportional to the surface tension and a damping coefficient proportional to viscosity and radius. This can be expressed as

$$M \frac{d^2 a}{dt^2} + C \frac{da}{dt} + Ka = 0 \tag{38}$$

where

M = mass = $(4/3)\ \pi\ r^3 \rho$

a = amplitude of response

t = elapsed time

$C \propto r\mu$

$K \propto \sigma$.

The solution to Eq. (38) is

$$a = Ae^{-tC/2M} \cos(\omega t + \varphi) \tag{39}$$

where

A = maximum amplitude

ω = angular velocity

φ = phase angle.

The time required to achieve a certain percent decay can be readily found from Eq. (39) as follows:

$$t = -2 \frac{M}{C} \ell n \, (a/A) \propto - \frac{r^2}{\nu} \ell n \, (a/A) \tag{40}$$

with the corresponding circular frequency being

$$f = \frac{\omega}{2\pi} = \frac{1}{2\pi} \sqrt{\frac{K}{M}} \propto \sqrt{\frac{\sigma}{\rho r^3}} \tag{41}$$

E. MELTING AND SOLIDIFICATION TIMES

Time to Melt Specimen

From the operating characteristics of a heat source, the time needed for melting can be calculated by equating the heat input from the source to the change in internal energy plus the radiative loss. This yields the following for minimal conduction loss (i.e., M553);

$$\dot{q} = MC \frac{dT}{dt} + A \sigma \epsilon \, (T^4 - T_o^4) \tag{42}$$

or rearranging

$$\int_{T_o}^{T_M} \frac{dT}{\frac{q}{4\pi r^2 \sigma \epsilon} + T_o^4 - T^4} = \int_{t=0}^{t} \frac{3\sigma \epsilon}{\rho r C} \, dt \, . \tag{43}$$

Performing this integration yields

$$t = \frac{\rho r C}{6\sigma \epsilon T'^3} \left\{ \ell n \left[\left| \frac{(T' + T_M)(T' - T_i)}{(T' - T_M)(T' + T_i)} \right|^{1/2} \right] + \tan (T_M/T') - \tan (T_o/T') \right\} \quad (44)$$

where

$$T'^4 = \frac{\dot{q}}{4\pi r^2 \sigma \epsilon} + T_o^4 \, . \quad (45)$$

Upon reaching the melting temperature, the time needed to melt can be estimated by equating the available heat (source input less radiative loss) to the heat absorbed during formation of a complete melt. This gives

$$\dot{q}\, t_M - 4\pi\, r^2 \epsilon \sigma\, T_M^4 = \frac{4}{3}\, \pi\, r^3 \rho\, \lambda_f \, . \quad (46)$$

where

t_M = time to melt

T_M = temperature of melting.

Rearranging yields

$$t_M = \frac{(4/3)\, \pi\, \lambda_f\, r^3\, \rho}{\dot{q} - 4\pi\, r^2\, \epsilon\, \sigma\, T_M^4} \quad (47)$$

Thus, the total time for heating and melting is

$$t_{total} = t + t_M \, . \quad (48)$$

In the derivations for both of these times, it was assumed that isothermal conditions prevailed; i.e., the sphere is at uniform temperature. This would be realistic for materials of relatively high thermal conductivity. However, a "warm up" time is associated

with low k materials as a result of finite heat conduction and this time can be estimated by an order of magnitude analysis of Fourier's heat conduction equation,

$$\nabla^2 T = - \frac{1}{\alpha} \frac{\partial T}{\partial t} \tag{49}$$

with

$$\nabla^2 = O(1/r)^2 \tag{50}$$

α = thermal diffusivity = $k/\rho C$

t_c = conduction time

Thus

$$O(T/r^2) = \frac{1}{\alpha} O(T/t_c) \tag{51}$$

or rearranging

$$O(1/r^2) = O(1/\alpha t_c) . \tag{52}$$

This relation shows that the thermal diffusivity is a measure of the time required to heat a material to a given temperature level and is seen to be proportional to the square of the conducting path and reciprocal transfer time. A final result can be obtained from Eq. (52) by solving for this time,

$$t_c = r^2/\alpha = \rho\, r^2\, c_p/k \tag{53}$$

In a transient heating process the thermal capacity of the material governs the amount of energy absorbed and the thermal conductivity dictates the rate. Thus, for large k the time to reach the melting temperature is governed by Eq. (44) while for small k, Eq. (53) applies. A maximum time (upper bound) can be estimated by the addition of all three times (Eqs. (44), (47) and (53)); however, in practice a tradeoff should be made between Eq. (44) and Eq. (53), depending on the value of the conductivity and the magnitude of convection present.

The maximum temperature capable of a given heat source can be readily obtained from a balance of heat input from source and the loss due to radiation. This can be expressed as

$$\dot{q} = 4\pi\, r^2\, \epsilon\, \sigma\, T^4 \tag{54}$$

or

$$T_{max} = \left(\frac{\dot{q}}{4\pi \, r^2 \, \epsilon \, \sigma} \right)^{1/4} \tag{55}$$

Solidification Time

The time needed for a liquid sphere to solidify can be estimated by equating the heat of fusion to the time integral of the radiated dissipation rate; i.e.,

$$\lambda_f M = \int_0^t A \epsilon \sigma (T^4 - T'^4) \, dt \tag{56}$$

where

λ_f = heat of fusion
A = surface area
ϵ = emissivity
σ = Stefan-Boltzmann constant
T = solidification temperature
T' = surrounding temperature.

Since $T'^4 \ll T^4$, Eq. (56) can be reduced to

$$t = \frac{\lambda_f \, r \, \rho}{3 \epsilon \, \sigma \, T^4} \tag{57}$$

SECTION III. M551 METALS MELTING EXPERIMENT

A. GENERAL

During the course of the investigation all process phenomena have been considered with particular attention given to adhesion-cohesion studies with emphasis on the fluid dynamics of the molten metal. This was accomplished by establishing all expected variations in terrestrial versus space processing occurring as a result of

- The dominance of capillary motion (instead of gravity-induced flow)
- Minimal segregation (sedimentation), and
- A decrease in hydrostatic pressure gradient.

These mechanisms are all hydrodynamical in nature; thus gravity has no direct affect on grain structure or any other properties of the solidified material. The gravity effects occur as a result of differing fluid motion.

The following items are considered the most significant contribution to the M551 experiment analysis:

- Establishment of the role of vaporization in the cavity shape
- Performance of three-dimensional temperature calculations for weld and dwell modes of melting for multi-component variable property material, and
- Establishment of magnitude and direction of gravity during actual Skylab mission to allow meaningful conclusions to be drawn from micrographs about zero-gravity effects.

Analysis of the aforementioned results has produced the following projections of effects of zero-gravity.

- Since all fluid mechanic phenomena require a finite time to occur (due to inertia considerations) an effect due to gravity during the weld portion of the experiment may not occur (except for a more spherical bead when beading occurs) as large cooling rates are available via conduction.

- A more homogeneous dwell structure will occur due to lack of sedimentation.

- The liquid cavity shape will be determined by vaporization effects and should be nearly symmetric (different temperature gradients do exist in positive and negative radial directions).

- If degassing is the cause of the splattering as noted in color films of the process, porosity may result in the zero-gravity dwell as the driving force for the pockets to surface is less.

B. THERMAL HISTORY RESULTS

Thermal histories corresponding to the experimental test conducted at NASA-MSFC with the M512 Facility have been calculated. The stainless steel disk was discretely divided into 289 nodal points shown schematically in Figure 4. The operating procedure consisted of the weld beginning at node 4 and continuing around the weld circle through all four quadrants. The weld portion ends at a time of approximately 19 seconds with the dwell beginning on node 316 at 19.5 seconds and continuing until 34.5 seconds (15-second duration). The input power was 1 kW with a 75% conversion efficiency assumed for the calculations. Table 1 defines the eb location as a function of time for both the weld and dwell modes of operation.

Figure 5 shows the nodes on the weld circle for the entire quadrant of the thin section (0.02-inch thickness). This result indicates that full penetration will occur with an average of 500°C superheat. Notice also as the dwell is begun at 20 seconds, no effect is seen at this location. Figure 6 shows the radial distribution of temperature corresponding to the center of the quadrant. Note that the nodes surrounding the weld circle do not melt as the maximum temperature is 800°C. Also a nearly symmetric radial temperature gradient about the weld circle is seen to exist. Figure 7 gives the weld circle distribution of temperature through the entire quadrant of 0.05-inch thickness. Again, full penetration is predicted with 300°C of superheat. Figure 8 reveals the same results as those for the thin section, namely, no melting except on the weld circle and again near symmetry existing.

The situation in the third quadrant consisting of a 0.125-inch thickness section is shown in Figure 9. For this beam power (1 kW) these results indicate that melting is confined to near the surface. In fact the average temperature over one third of the thickness is below the melt temperature indicating that less than one-third penetration occurs. Figure 10 shows the profiles just below the surface

Table 1

ELECTRON BEAM POSITION VERSUS TIME (DISK ROTATION)

Node	Time (sec)	Node	Time (sec)	Node	Time (sec)	Node	Time (sec)
4	0	104	5.5805	204	11.161	304	17.237
10	0.62005	110	6.2005	204	11.657	310	18.454
16	1.2401	116	6.8206	210	12.773	316	19.570
22	1.8602	122	7.4406	216	13.889	316	34.570
28	2.4802	128	8.0607	222	15.005		
34	3.1003	134	8.6807	228	16.121		
40	3.7203	140	9.3008				
46	4.3404	146	9.9208				
52	4.9604	152	10.541				

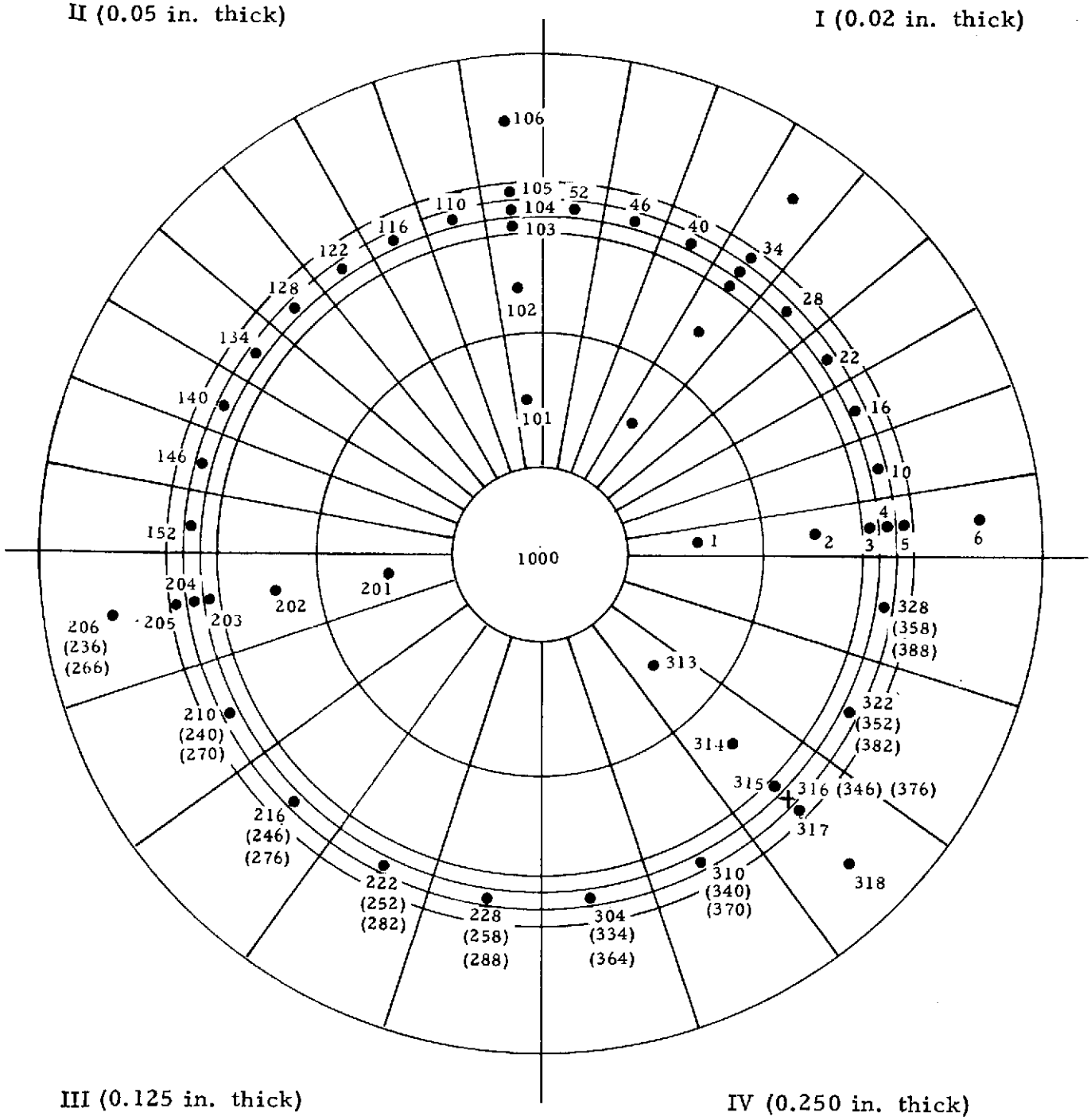

FIGURE 4. NODAL POINT ARRANGEMENT FOR THERMAL CALCULATIONS

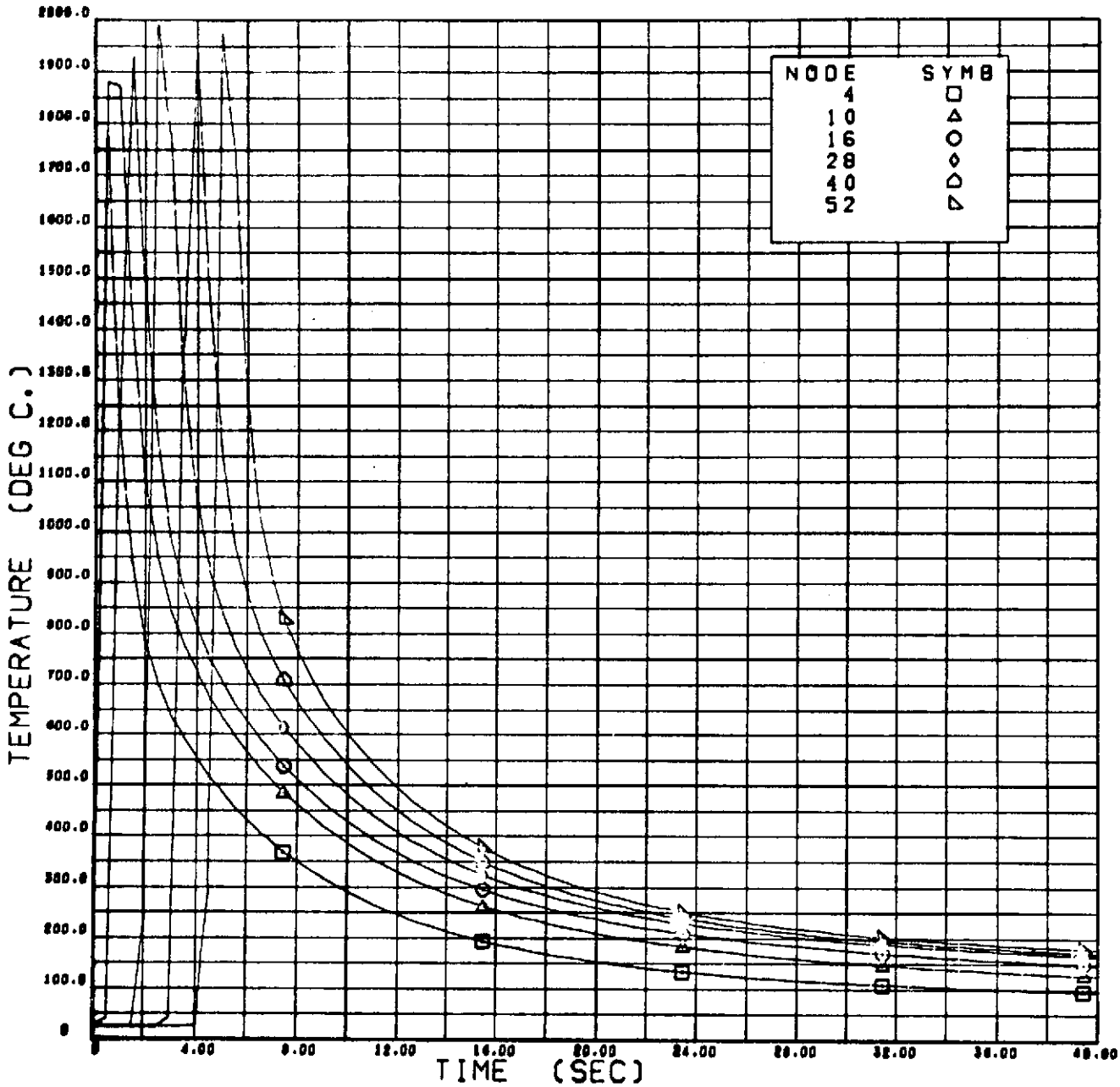

FIGURE 5. THERMAL HISTORY FOR 0.02-INCH STAINLESS STEEL DISK (NODES 4, 10, 16, 28, 40 AND 52)

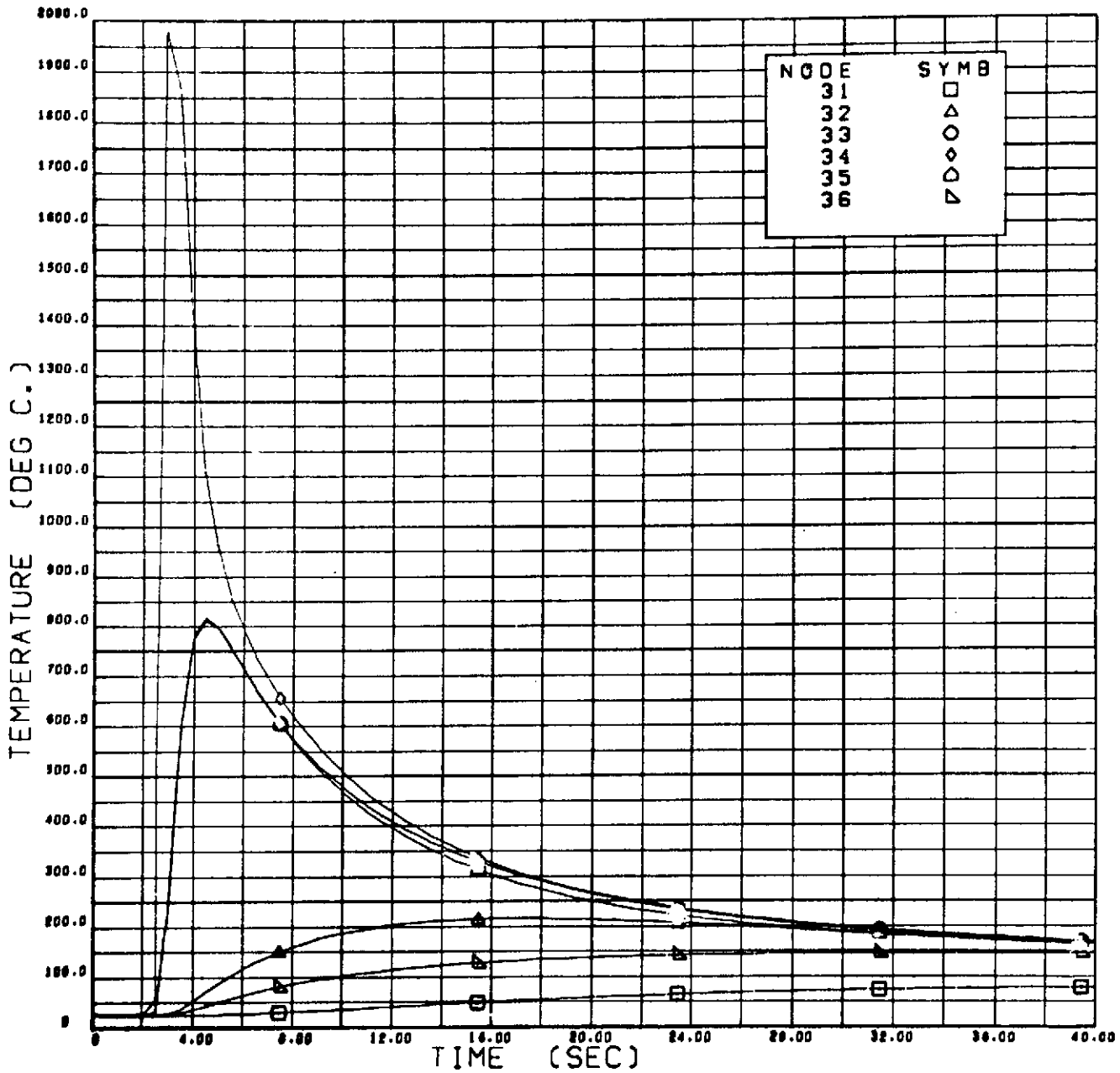

FIGURE 6. THERMAL HISTORY FOR 0.02-INCH STAINLESS STEEL DISK (NODES 31 THROUGH 36)

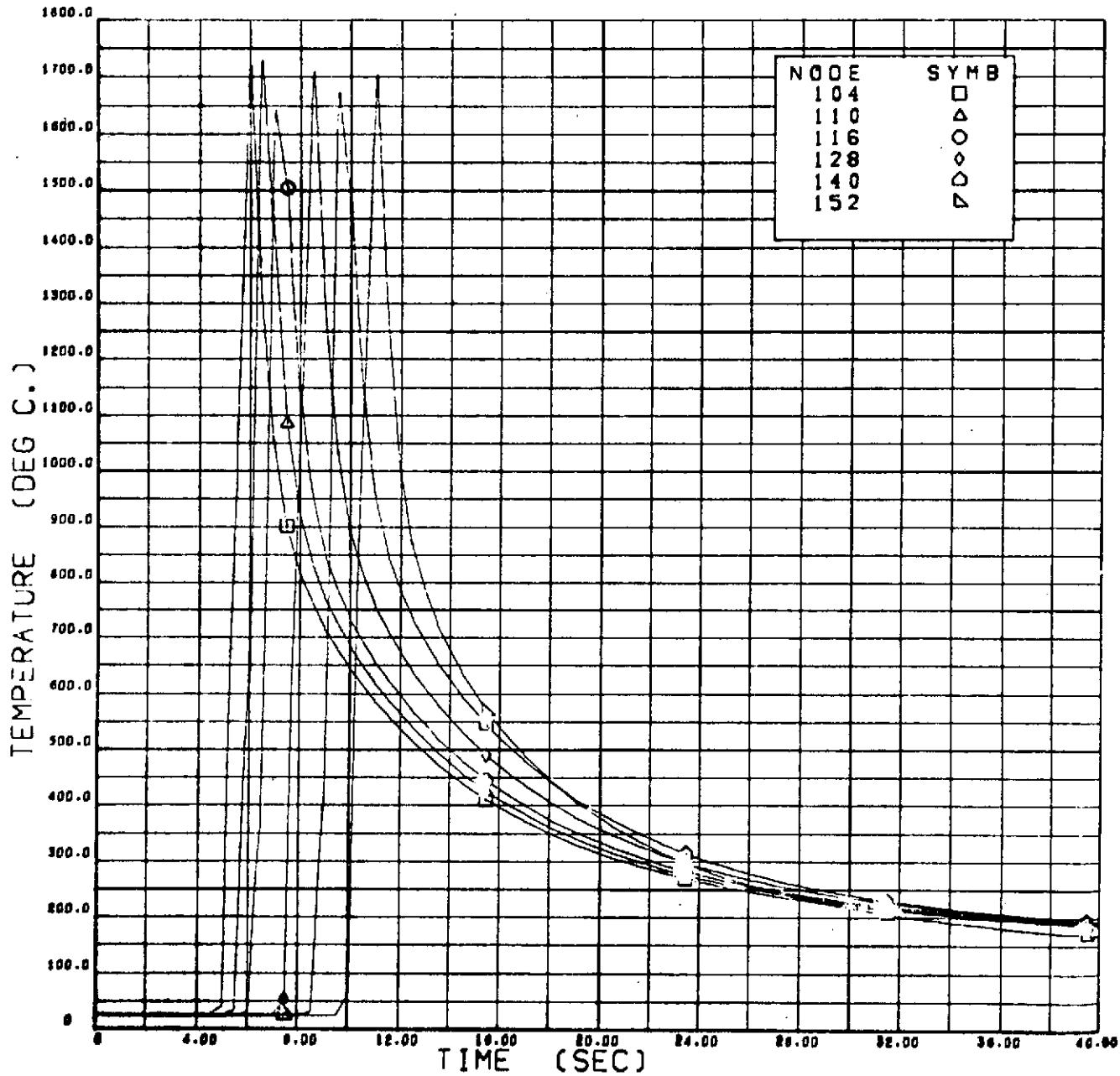

FIGURE 7. THERMAL HISTORY FOR 0.05-INCH STAINLESS STEEL DISK (NODES 104, 110, 116, 128, 140 AND 152)

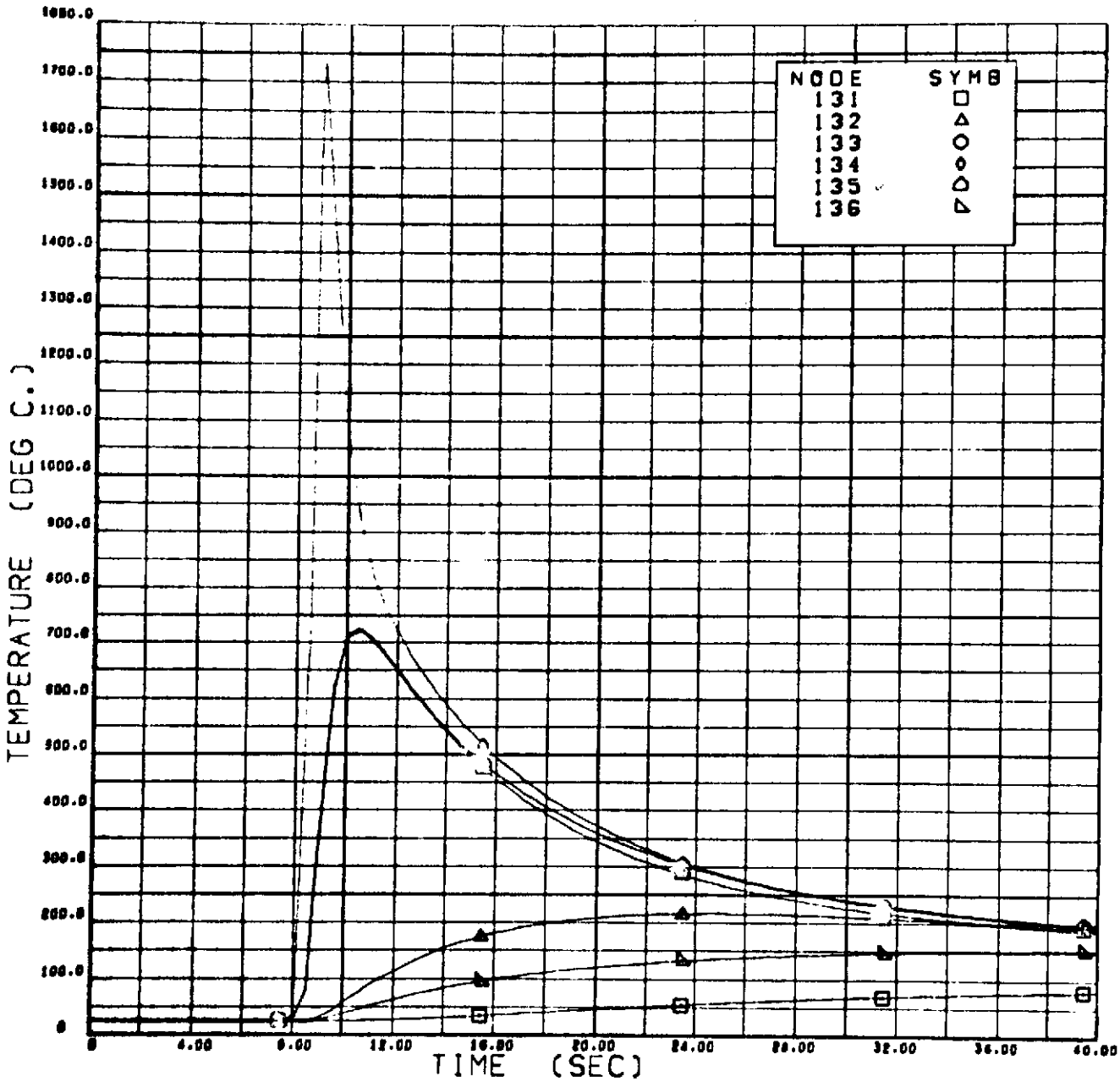

FIGURE 8. THERMAL HISTORY FOR 0.05-INCH STAINLESS STEEL DISK (NODES 131 THROUGH 136)

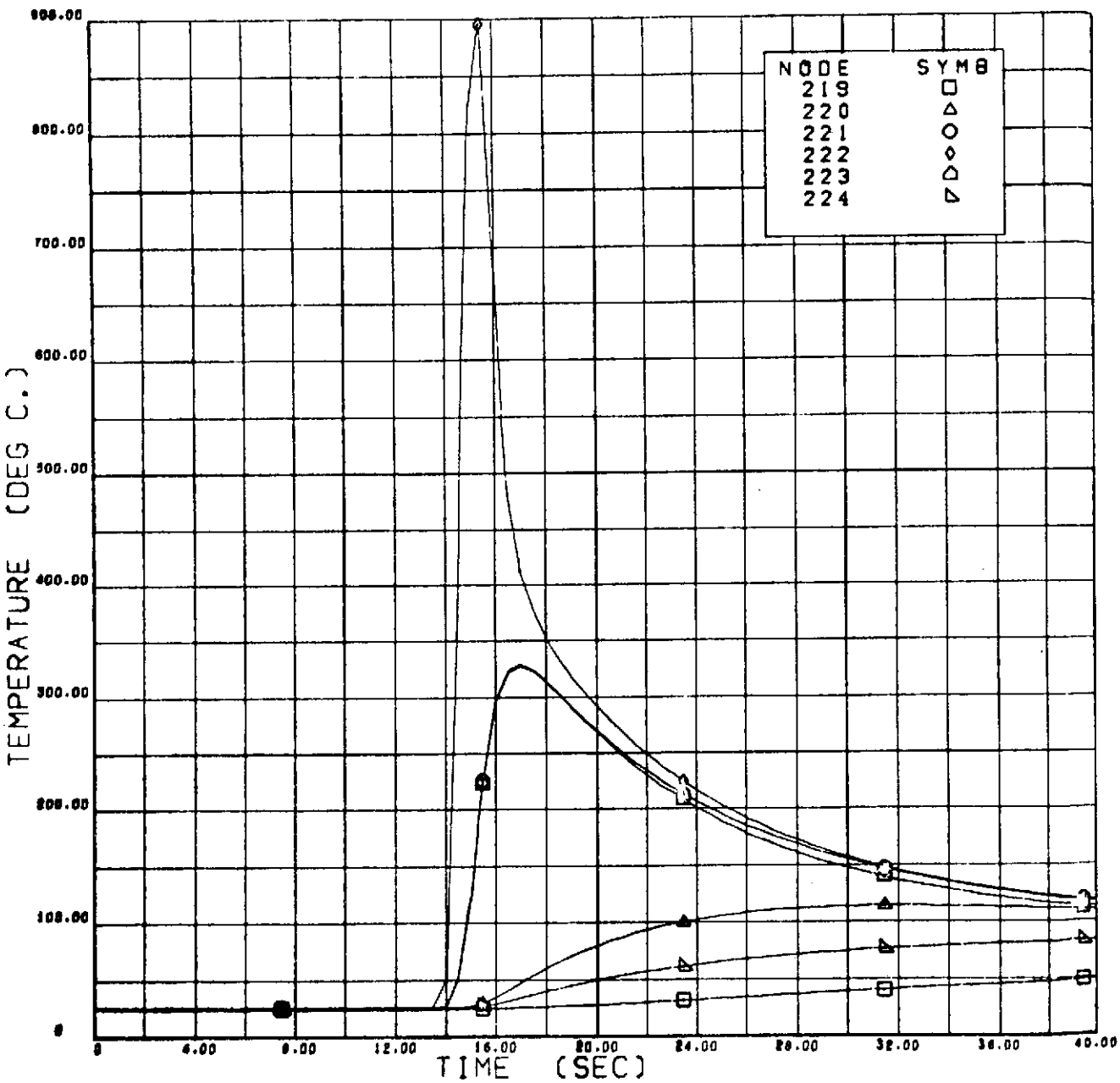

FIGURE 9. THERMAL HISTORY FOR 0.125-INCH STAINLESS STEEL DISK (NODES 219 THROUGH 224)

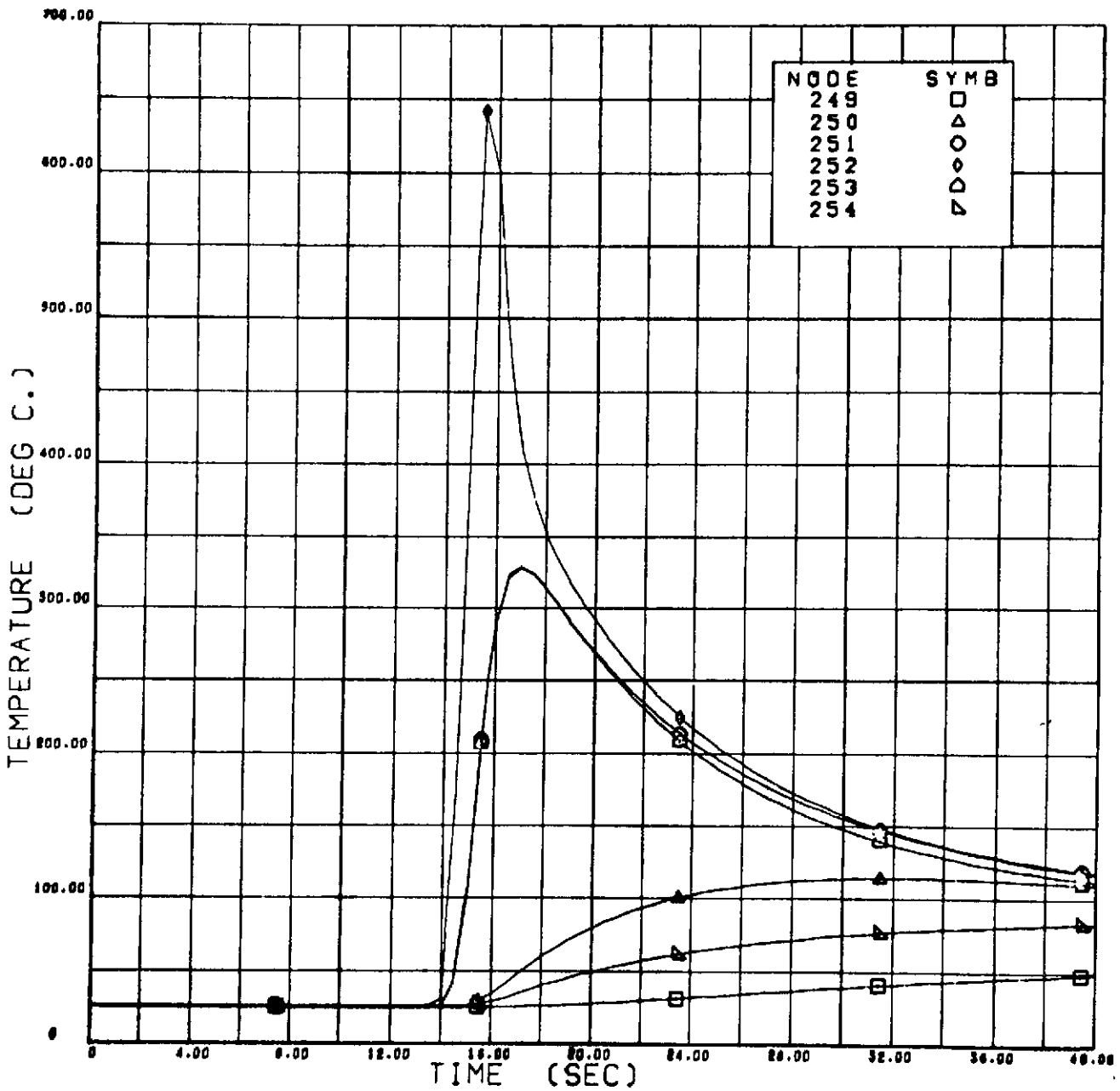

FIGURE 10. THERMAL HISTORY FOR 0.125-INCH STAINLESS STEEL DISK (NODES 249 THROUGH 254)

node as shown in the previous figure. Exactly the same trend is observed with lower maximum temperatures. The radial profile for the bottom layer is shown in Figure 11, indicating precisely the same trend as before. The thickest quadrant results are shown in Figure 12 for the upper surface where again melting is seen to occur only near the surface. Here, an asymmetric situation develops about the weld circle with a substantial difference in temperature in the positive and negative radial directions. As the center of this quadrant is reached the dwell portion of the cycle is initiated as depicted in Figures 13 and 14. It is seen that nearly full penetration is predicted (no allowance for eb cavity) and a substantial melt region is outlined. Within a few seconds of eb cutoff, nearly isothermal conditions result near the dwell region as indicated by the temperatures at 40 seconds.

A comparison between these calculated results and those obtained by experiment are shown in Table 2 where the maximum temperatures are given in each case. The calculated results in the weld case are consistently lower than the corresponding experimental values. As previously stated, a 1 kW beam power (50 mA and 20 kV) was assumed with an efficiency of 75% giving rise to an input power of 0.75 kW. If the actual input power was slightly higher, this could explain the trend. Also some of the maximum temperatures for the dwell occur after 40 seconds. This accounts for the dwell temperatures in the table being listed as greater than some level (i.e., > 50). This means that the maximum temperature will occur later in time than the cutoff of the plot. In general, however, agreement is fairly good. Temperature histories were also calculated for aluminum and tantalum disks, and the results are given in Appendix B.

C. BEADING CONSIDERATIONS

Upon examination of the M551 disks, it has been noted that a beading occurs behind the electron beam as the beam moves through the molten material. At present, no detailed analysis has been conducted to explain this phenomenon; however, some consideration has been given to understanding the mechanism. In order to present a hypothesis explaining the proposed mechanism some background information is presented.

The movement of the electron beam cavity through the molten metal resembles the motion of an infinite cylinder (especially if full penetration occurs) through a fluid. It has long been known that such a body leaves in its wake a regular pattern of vortices which move alternately clockwise and counterclockwise and is known as a Karman vortex street. A schematic is presented in Figure 15.

Table 2

COMPARISON OF CALCULATED AND EXPERIMENTAL MAXIMUM TEMPERATURES

Node No.	Thermocouple No.	Weld		Dwell	
		Calculated Max. Temp. (°C)	Experimental Max. Temp. (°C)	Calculated Max. Temp. (°C)	Experimental Max. Temp. (°C)
317	1	322	387	1430	638
315	2	236	349	1105	1160
223	4	330	515	112	—
221	5	332	404	118	171
219	6	37	97	>50	171
135	7	725	871	187	—
133	8	725	815	196	121
131	9	41	102	>80	118
35	10	818	1093	165	—
33	11	819	599	169	163
31	12	58	91	>80	106

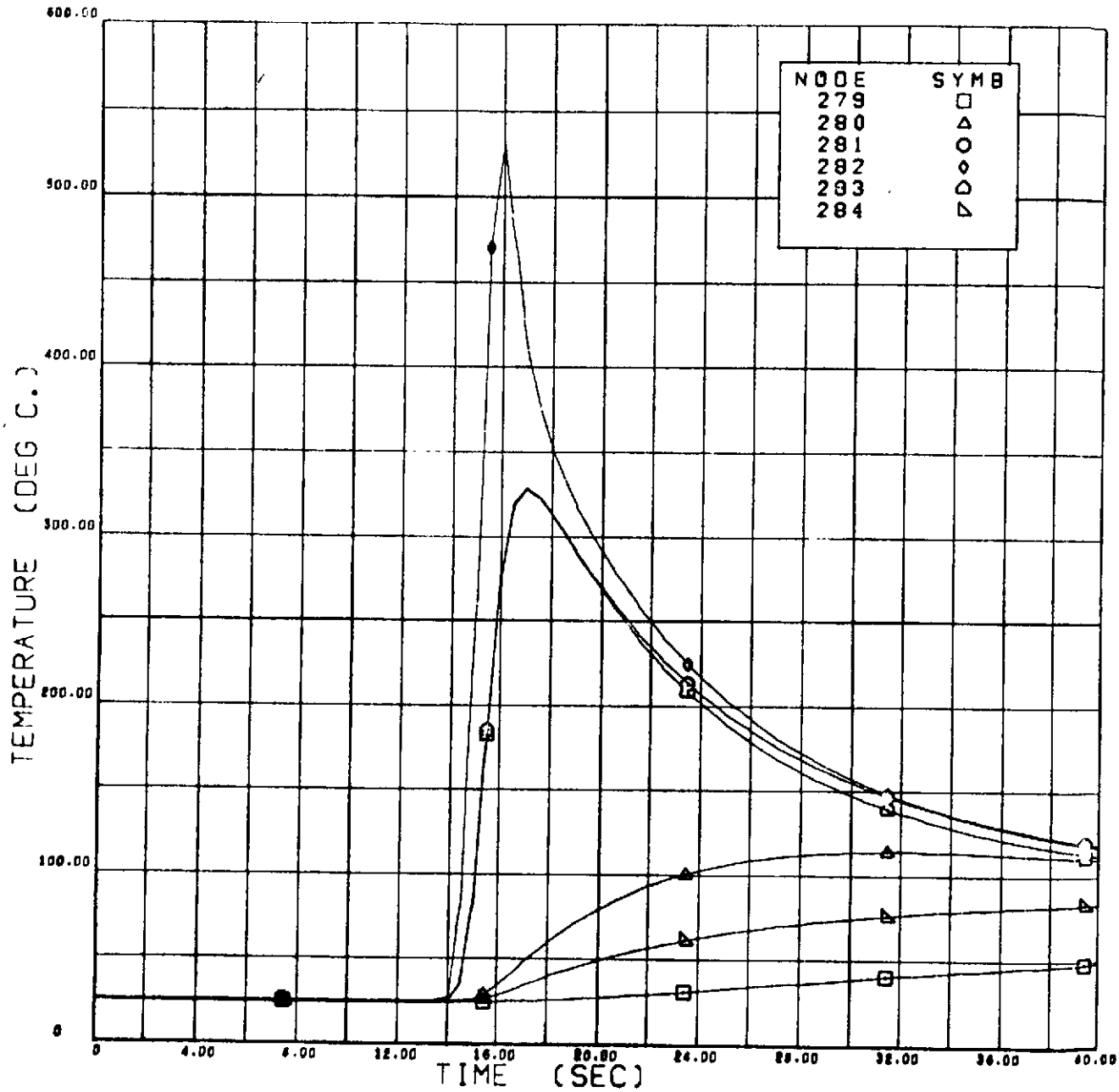

FIGURE 11. THERMAL HISTORY FOR 0.125-INCH STAINLESS STEEL DISK (NODES 279 THROUGH 284)

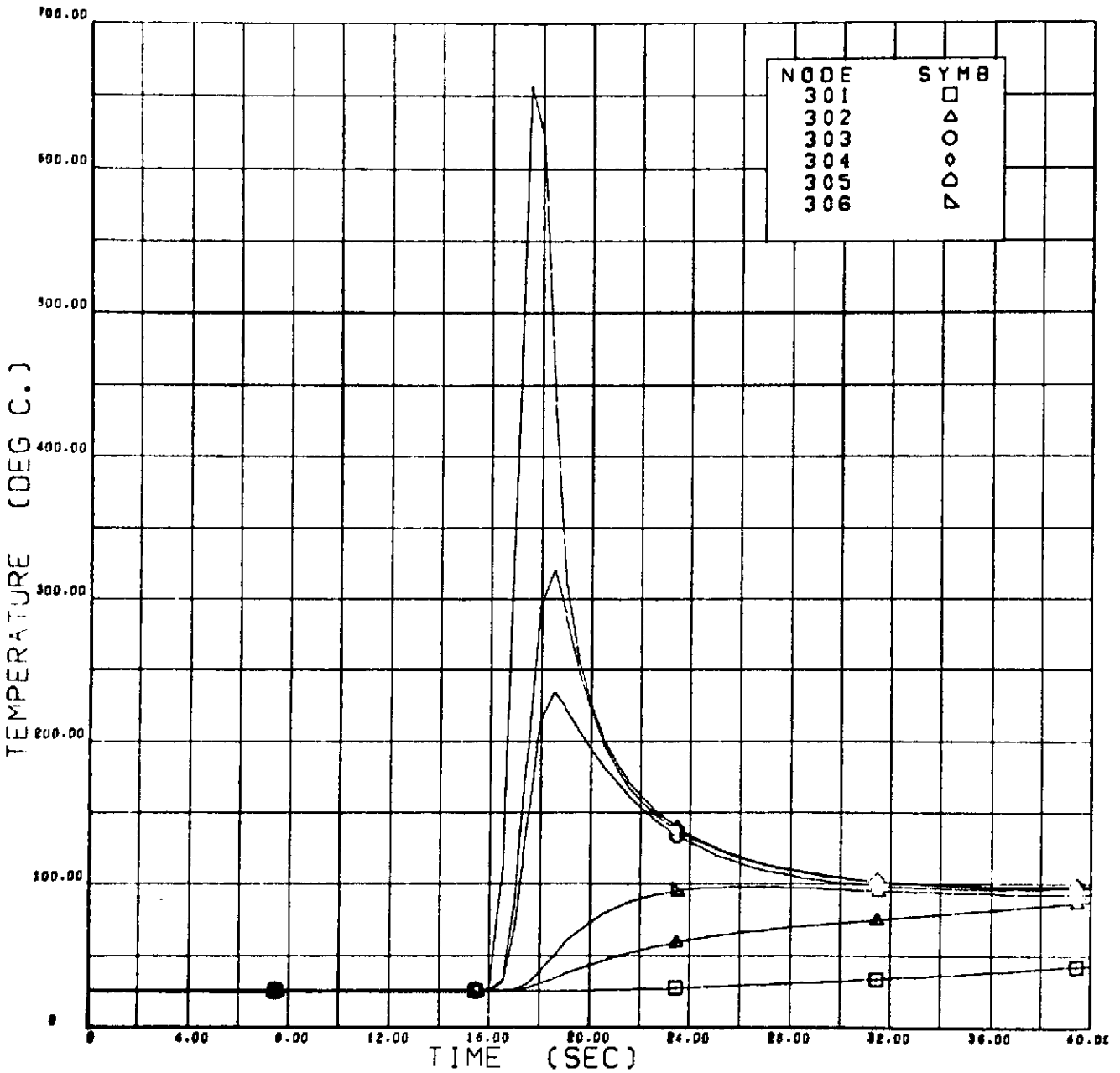

FIGURE 12. THERMAL HISTORY FOR 0.25-INCH STAINLESS STEEL DISK (NODES 301 THROUGH 306)

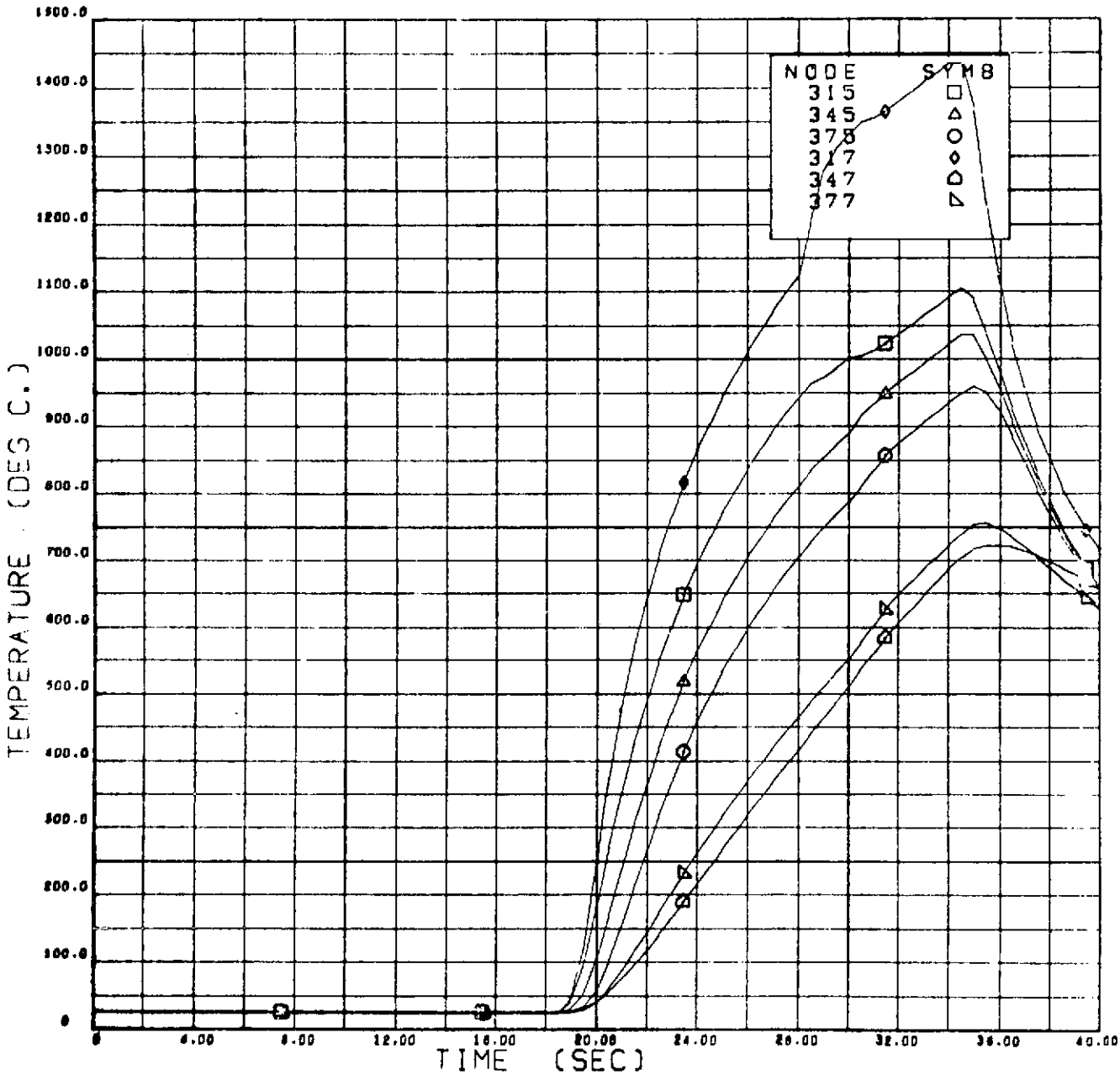

FIGURE 13. THERMAL HISTORY FOR 0.25-INCH STAINLESS STEEL DISK (NODES 315, 345, 375, 317, 347 AND 377)

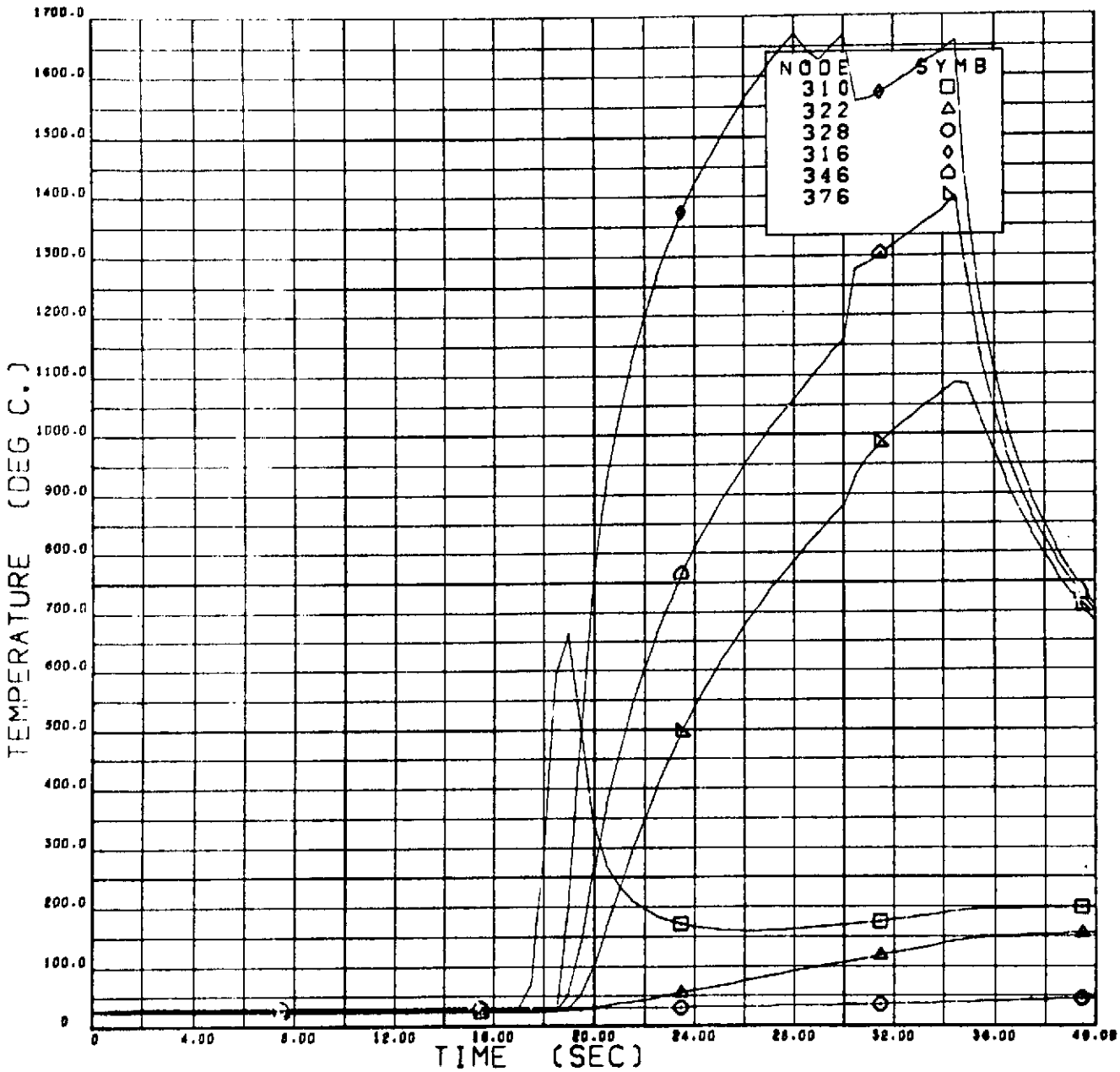

FIGURE 14. THERMAL HISTORY FOR 0.25-INCH STAINLESS STEEL DISK (NODES 310, 322, 328, 316, 346 AND 376)

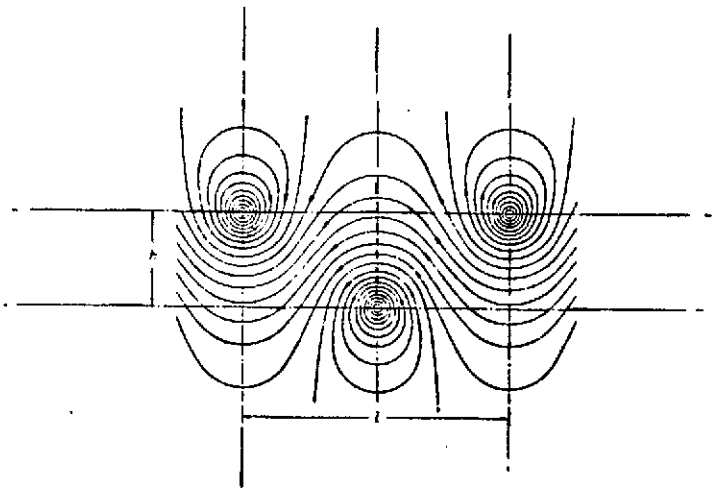

FIGURE 15. KARMAN VORTEX STREET (DIAGRAMMATIC); STREAMLINES DRAWN IN A SYSTEM OF COORDINATES MOVING WITH THE VORTEX STREET

There exists a distinct frequency at which the vortices on one side of the wake are shed that depends only on the Reynolds number of the fluid motion and is given by the Strouhal number, i.e.,

$$S = \frac{fD}{v}$$

where f is the frequency, D is the diameter of the cavity and v is the velocity of the beam in the liquid metal.

From experiment, the relationship of the Strouhal number to the Reynolds number has been determined and is shown in Figure 16. This shows that a critical Reynolds number exists below which no shedding has been observed.

Using these concepts the theoretical number of beads per unit length has been determined for the M551 materials. It should be mentioned that no attempt has been made to account for the solid material (edges) in the cut or the extent of melt in the radial direction of the disks (which is a function of the thermal conductivity). These results are shown in Table 3. The surface tension is included as the magnitude indicates the tendency of the vortices to bead before solidification occurs.

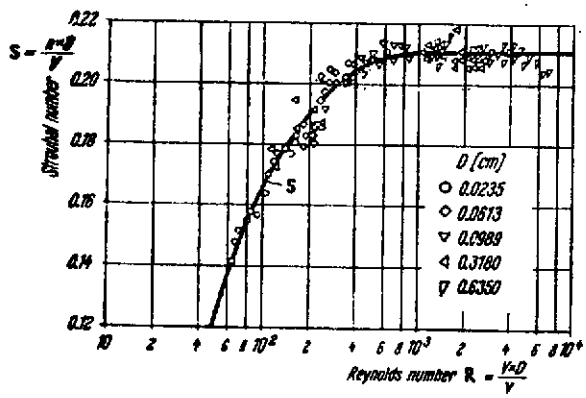

FIGURE 16. STROUHAL NUMBER VS REYNOLDS NUMBER

TABLE 3

BEAD POPULATION

M551 Materials	Reynolds No.	Strouhal No.	Shedding Freq. (beads/ sec)	Beads per cm (on each side)	Total Beads (both sides)	Surface Tension (dynes/ cm)
321 Stainless Steel	55	0.125	0.8	0.5	1.0	1750
2219 Aluminum	86	0.155	1.0	0.6	1.2	737
Tantalum	207	0.19	1.2	0.75	1.5	2150

Some qualitative observation can be made concerning these results. First both aluminum and stainless possess Reynolds numbers near the critical values; thus it would not be surprising if some of the effects not accounted for could have a significant effect on the population of the beads if not controlling whether or not beading will

occur. Tantalum, however, possesses the largest Reynolds number and value of surface tension; thus it is expected that these properties produce the greatest probability of beading and will give rise to the greatest population of beads.

D. FLIGHT RESULTS

Shown in Figures 17 through 22 are photographs taken of stainless steel, aluminum and tantalum metal disks after being subjected to electron beam impingement in the M551 metals melting experiment. In these photographs, Skylab flight test specimens are compared to ground-based test specimens. The most striking phenomenon appearing in these photographs is the "beading" effect which occurs simultaneously with total penetration in the stainless steel and tantalum specimens. It was speculated in Section III-C that this beading effect may be related to vortex shedding. Theoretical bead spacing along the electron beam track was predicted based on calculated vortex shedding frequencies. Average bead spacing distances were estimated for both flight test and ground based test specimens by inspection of the photographs in Figures 17 through 22. These experimental values are compared to the predicted values (Table 3) in Table 4.

TABLE 4

BEAD SPACING

M551 Materials	Bead Spacing, cm		
	Theoretical	Flight Test	Ground Based Test
321 Stainless Steel	1.0	1.1	1.1
2219 Aluminum	0.8	—	—
Tantalum	0.7	3.6	2.2

The experimental bead spacing on the stainless steel specimens is seen to be in remarkably good agreement with the predicted value for both flight and ground based tests. No beading is exhibited on the aluminum specimen, however, and the spacing on the tantalum specimen is considerably larger than the predicted value. Consideration was given to the possibility that the departure from vortex shedding theory might be due to "wall" effects resulting from the limitation on the lateral extent of melting. The presence of confining parallel

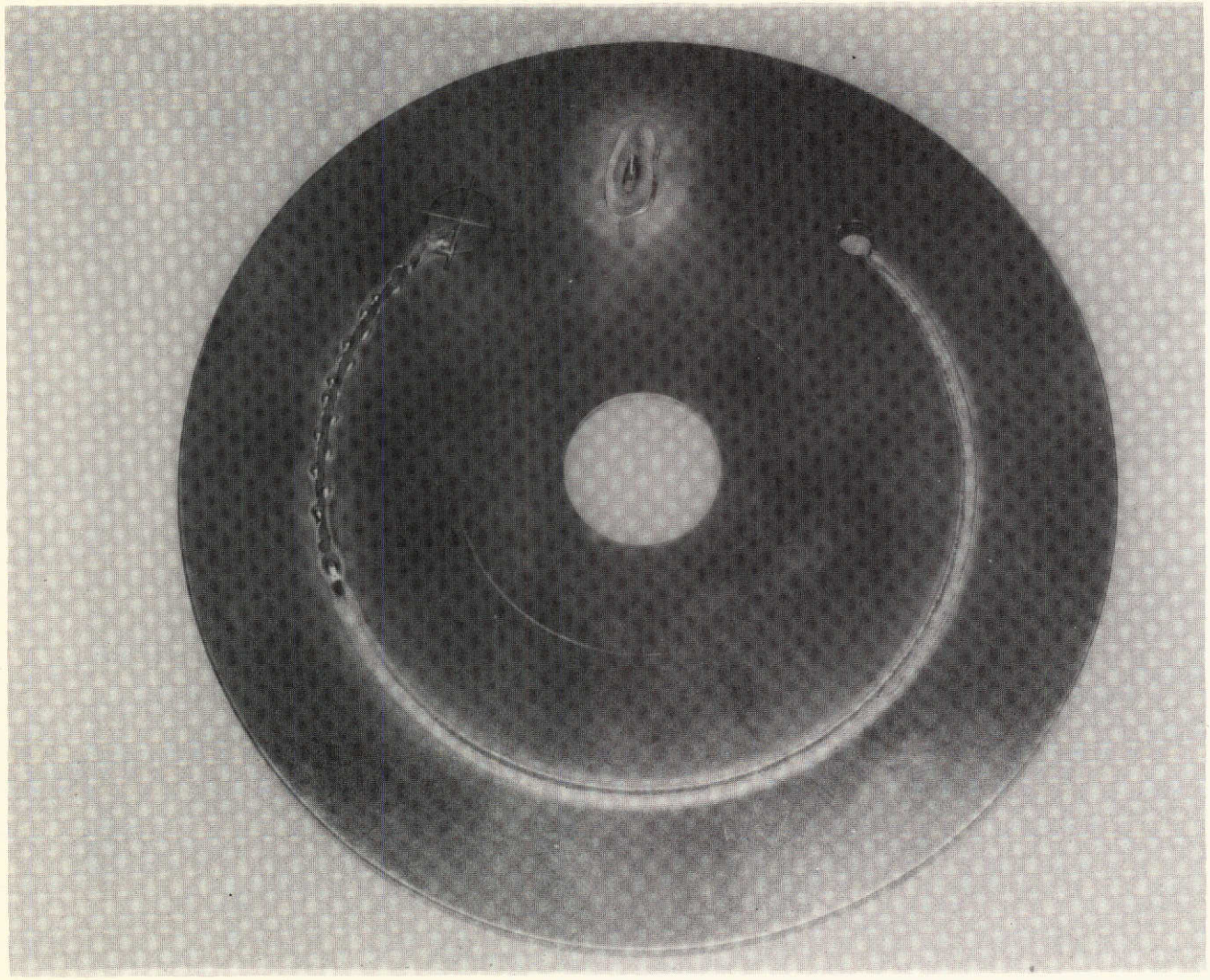

FIGURE 17. STAINLESS STEEL DISK AFTER M551 FLIGHT TESTS

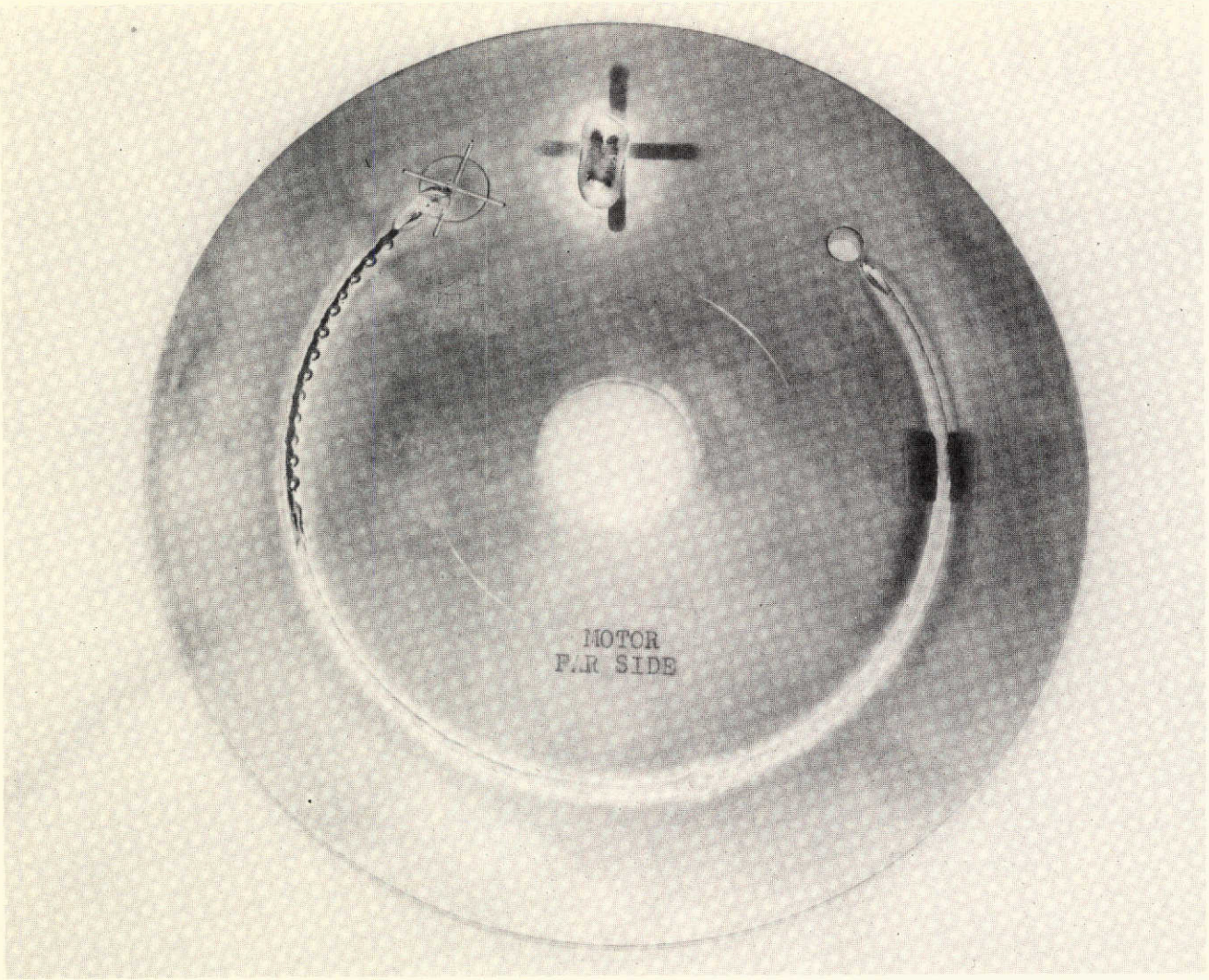

FIGURE 18. STAINLESS STEEL DISK AFTER M551 GROUND-BASED TESTS

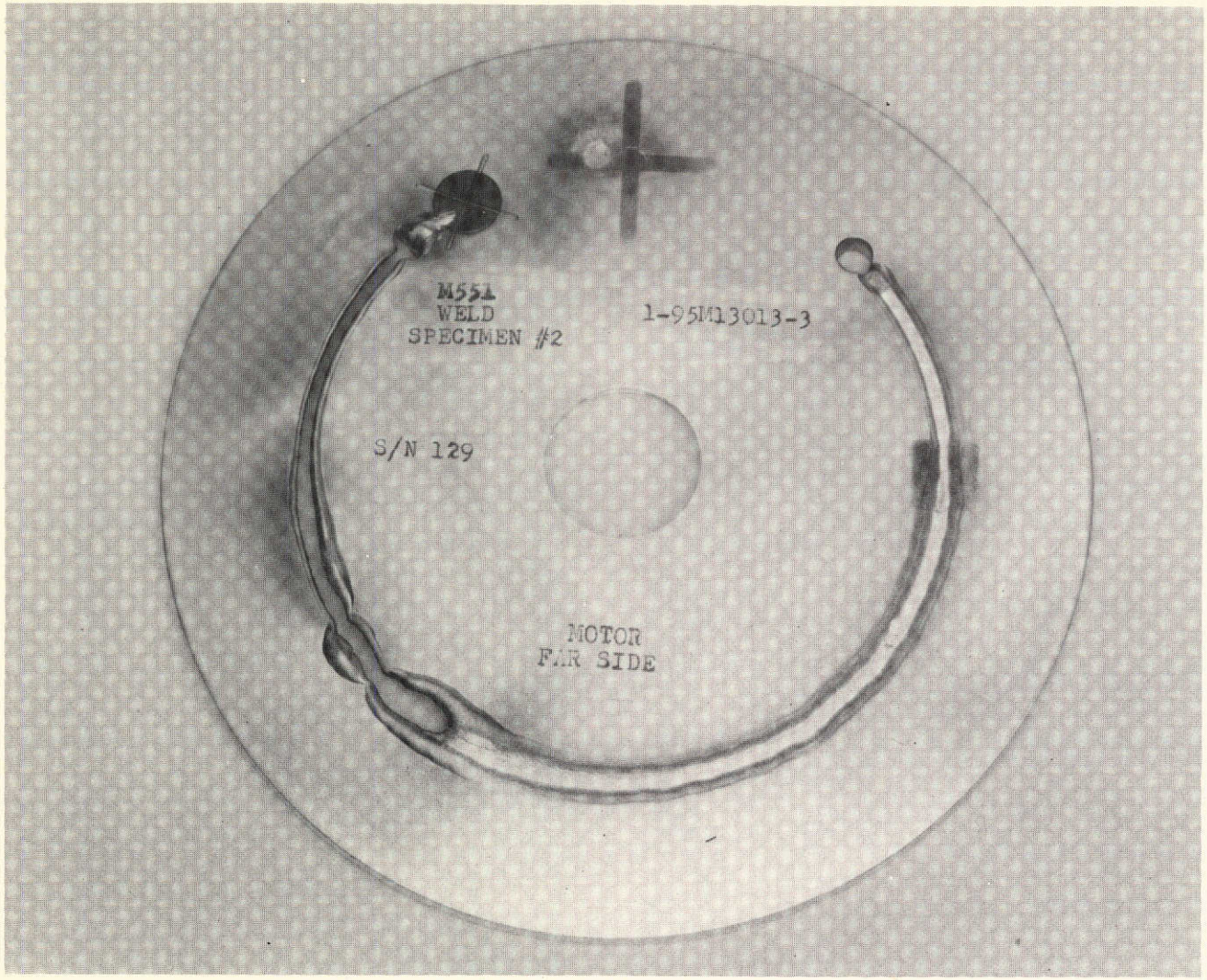

FIGURE 19. ALUMINUM DISK AFTER M551 FLIGHT TESTS

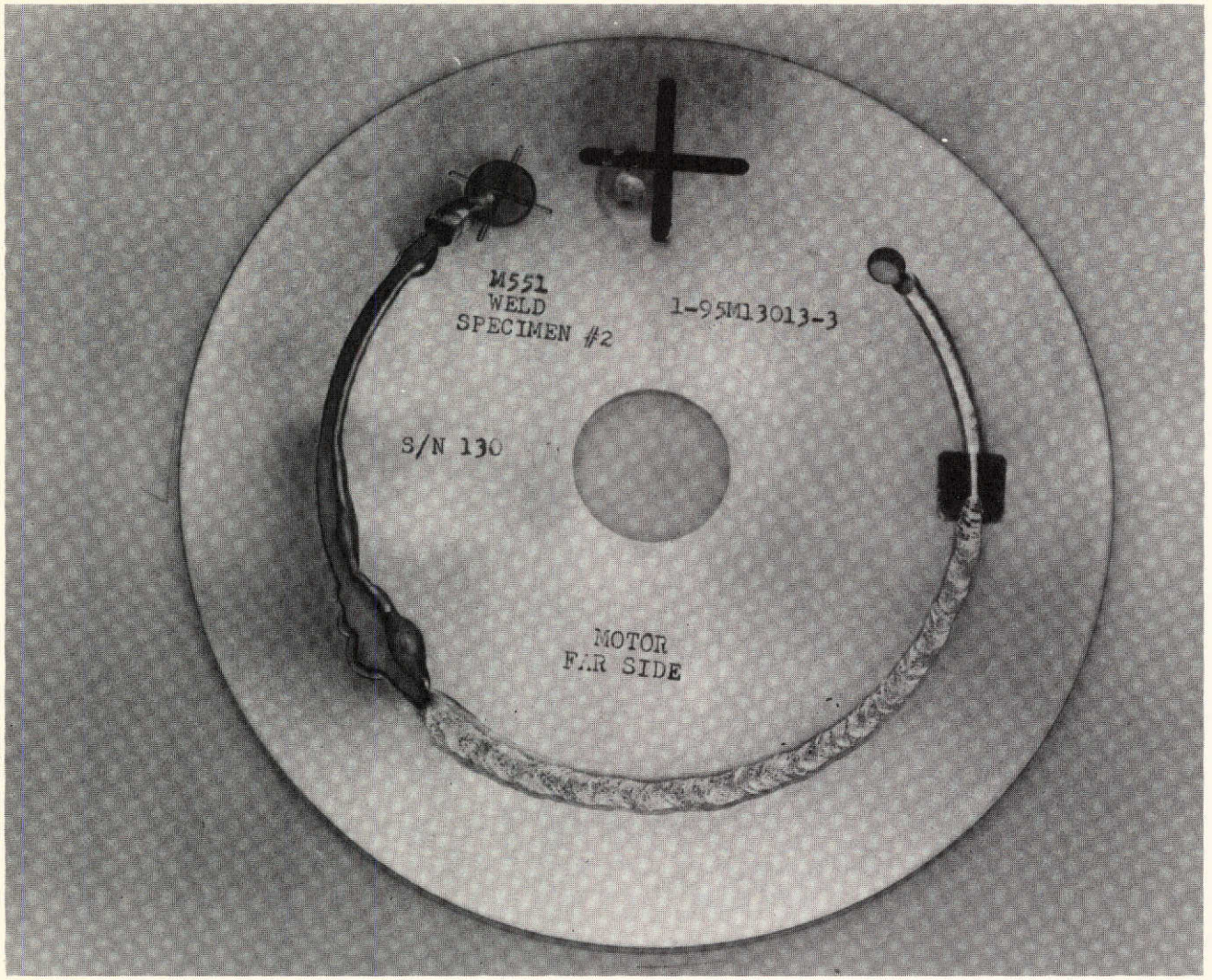

FIGURE 20. ALUMINUM DISK AFTER M551 GROUND-BASED TESTS

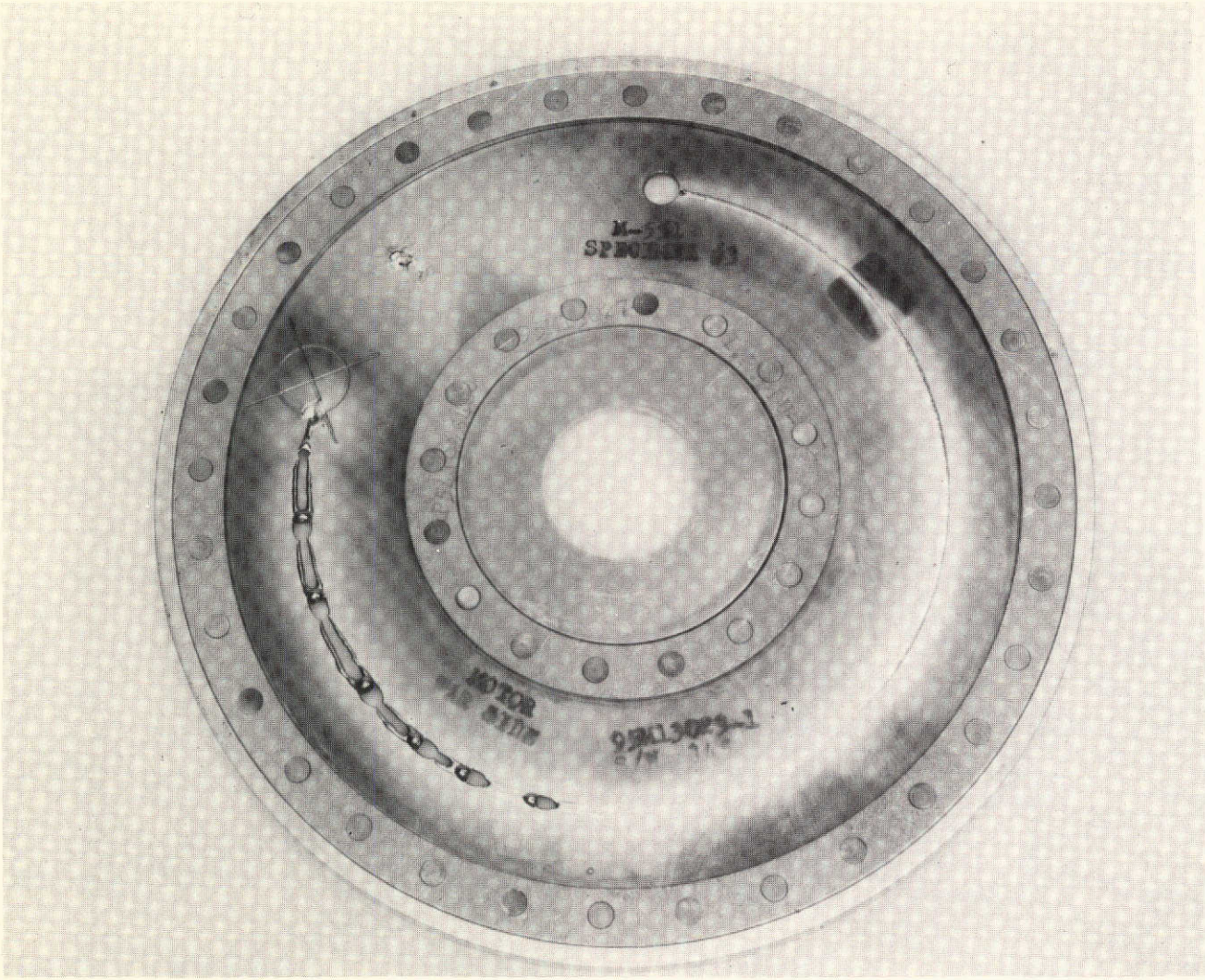

FIGURE 21. TANTALUM DISK AFTER M551 FLIGHT TESTS

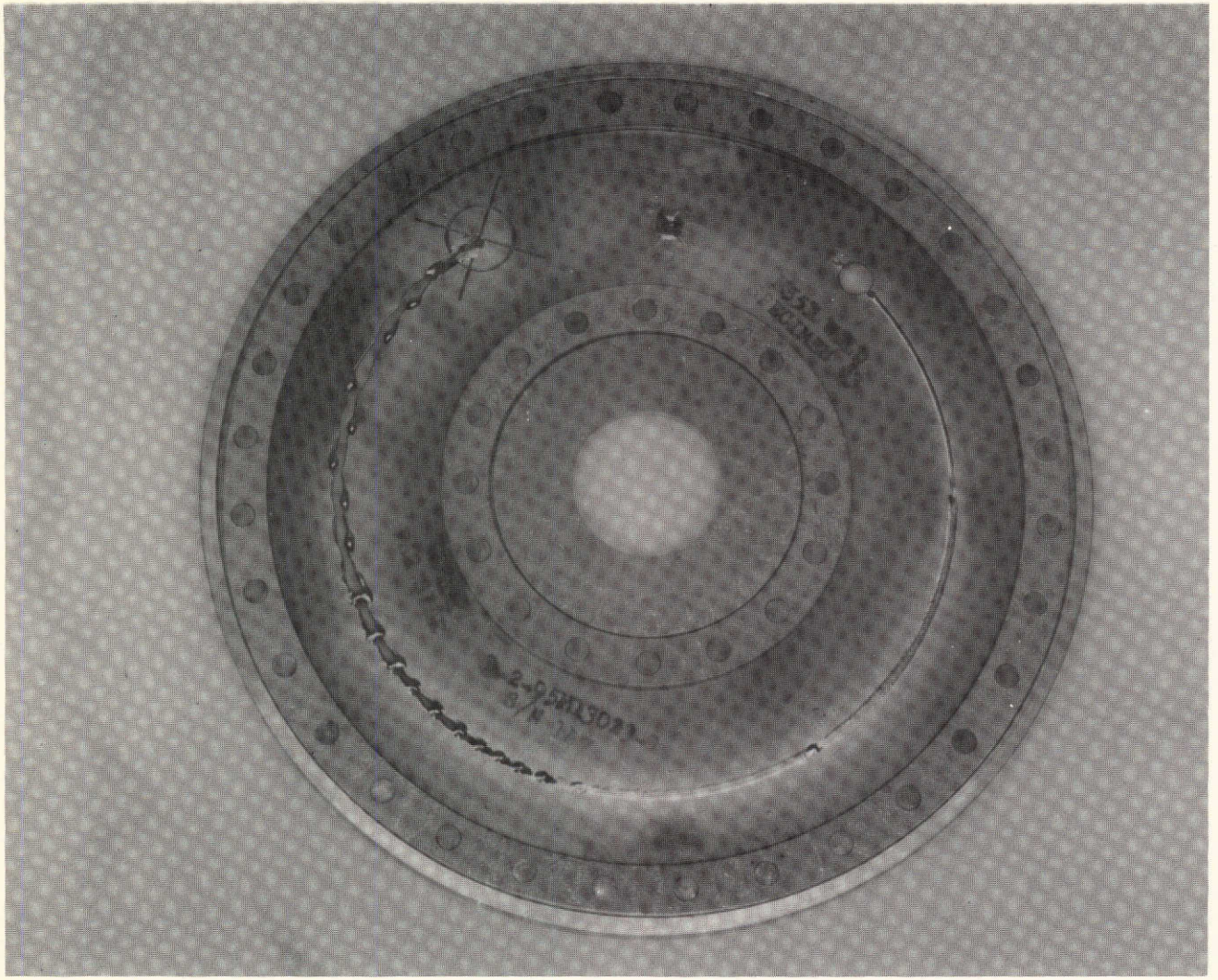

FIGURE 22. TANTALUM DISK AFTER M551 GROUND-BASED TESTS

walls will tend to increase the drag force on the cylinder due to the increased fluid velocity in the space between cylinder and wall. This may be considered equivalent to an increased "effective" Reynolds number for drag on the cylinder. Hypothesizing that the Strouhal number relates to this effective Reynolds number according to the relationship in Figure 16, the vortex shedding frequency should be increased by the presence of the confining walls. The results in Table 4, however, indicate the opposite trend. Wall effects, therefore, do not account for the observed departure from vortex shedding theory. Also, nearly identical bead spacing is noted for both flight and ground-based tests with the stainless steel specimens, while spacing on the tantalum specimens is larger for flight than for ground-based test. No definite trend can be established, therefore, in the effect of reduced gravity on bead spacing.

An indication of total penetration depth can also be obtained by inspection of the photographs. The plate thickness is smallest at the starting point of the electron beam track and increases with angular displacement along the track. Total penetration is seen to occur on all plates beginning at the beam starting point and ceasing at angular positions where the plate thickness becomes greater than the penetration depth. The penetration depth, therefore, should be approximately equal to the plate thickness where total penetration ceases. The angular positions where total penetration ceases and the corresponding plate thicknesses are given in Table 5 along with theoretical penetration depths determined according to a method presented in [7]. The

TABLE 5

OBSERVED AND THEORETICAL PENETRATION DEPTHS

M551 Materials	Flight Test		Ground Based Test		Theoretical Depth
	Plate Position (deg)	Plate Thickness (cm)	Plate Position (deg)	Plate Thickness (cm)	
321 Stainless Steel	75	0.104	70	0.915	0.195
2219 Aluminum	115	0.211	108	0.193	0.323
Tantalum	98	0.635	125	0.762	0.120

theoretical method is based on an energy balance in which the beam power is equated to energy absorbed in melting and lost to thermal conduction and re-radiation. The theoretical depths are seen to be within about a factor of two of the experimental results in all cases. No definite trends are noted in the differences between flight test and ground-based test results.

SECTION IV. M553 SPHERE FORMING EXPERIMENT

A. GENERAL

During the course of the investigation all process phenomena have been considered with particular attention given to adhesion-cohesion studies with emphasis on the fluid dynamics of the molten metal. This was accomplished by establishing all expected variations in terrestrial versus space processing occurring as a result of:

- The dominance of capillary motion (instead of gravity-induced flow)
- Minimal segregation (sedimentation), and
- Decrease in hydrostatic pressure gradient.

These mechanisms are all hydrodynamic in nature, thus gravity has no direct effect on grain structure or any other property of the solidified material; the gravity effects occur as a result of differing fluid motion.

The following items are considered the most significant contributions to the M553 experiment analysis:

- Identification of physical forces affecting the trajectory of the molten sphere
- Development of unifying calculational technique to predict trajectory of molten spheres during free-float condition
- Development of three-dimensional thermal model to predict temperature history of sphere during melting
- Establishment of the role of vaporization on temperature history and motion of sphere
- Establishment of the magnitude and qualitative motion of surface dynamics, and
- Performance of detailed analysis of KC-135 flight test data and ground-based experimental tests.

Analysis of the aforementioned results has produced the following projections of effects of zero-gravity:

- Less heterogeneous nucleation will occur due to foreign particles as segregation effects will be minimal.

- If the material has any gas content that comes out of solution during solidification, an increase in porosity may result as there will be minimal tendency for the gas pockets to surface (except for convection effects).

- For the materials with high vaporization rates (Ni-12% Sn, and Ni-30% Cu), a substantial increase in surface cooling occurs — thus greater nucleation and surface tension gradients.

- Even though the cooling rate is dependent on the amount of convection, the cooling rate will be determined by radiation considerations only as the sphere reaches isothermal superheat conditions in approximately a second. This in turn dictates the solidification rate.

- Since solid formations in polycrystalline materials is highly dependent on the distribution of foreign particles and the liquid motion, the associated differences should be discernible (homogeneous nucleation).

As discussed previously, the only expected differences in zero-g versus one-g processing are the dominance of capillary motion instead of gravity-induced flow, the absence of segregation and a decrease in hydrostatic pressure. There are, however, many indirect effects (advantages) due to a lack of gravity. In general, the factors affecting the final sample properties, composition and structure can be divided into three major categories, i.e.,

- Nucleation
- Growth, and
- Reaction kinetics.

The absence of gravity might allow better control of the independent variables affecting each category; this occurs directly through the three aforementioned fluid dynamic effects and indirectly through other mechanisms that are a function of fluid motion (gas content, composition, foreign particles, imperfections, cooling rate, nucleation rate, etc.).

B. M512 VACUUM CHAMBER GEOMETRY

The geometry of the M512 chamber is shown in Figure 23 along with the coordinate system chosen. The pinwheel containing the specimen to be melted is mounted in the chamber in the y-z plane with the center of the specimen to be melted positioned at coordinates (-0.292, -0.750, -0.433) as shown in Figure 24. Figure 24 also defines the camera locations used in the KC-135 aircraft and ground-based (camera 1) tests with the associated line-of-sight geometry to account for mirror effects. The corresponding film frame projections are depicted in Figure 25 in the local ξ, η, ζ coordinate system.

C. M553 THERMAL CONSIDERATIONS

The theoretical foundation for computing the three-dimensional temperature history for a multi-component system has been presented in Section II. This subsection presents the results of calculations for the M553 materials of interest. First consider the time required for the material to become superheated and cool to the melt temperature for the operating procedures used in the actual Skylab mission. This time can be determined from the temperature history calculated by the Lockheed Thermal Analyzer which includes allowances for:

- A three-dimensional network
- Conduction heat loss
- Radiation heat loss
- Vaporization heat loss
- Variable properties (with temperature and phase), and
- Variable heat source.

The spheres are discretely modeled by 69 nodal points with each of the corresponding nodal temperature histories computed. Allowances are included for sting melting and automatic electron beam cutoff. The nodal arrangement is shown for the inner layer in Figure 26, with the outer layer and electron beam impingement location given in Figure 27.

The thermal history for pure nickel is shown in Figures 28 through 31. It is seen that in less than one second after eb cutoff the sphere is nearly isothermal in each layer. The time corresponding to the onset of solidification is shown in Figure 28 and is approximately 10.5 seconds. This time must be added to the time needed for solidification to determine the necessary free-float time for containerless solidification. The corresponding temperature histories

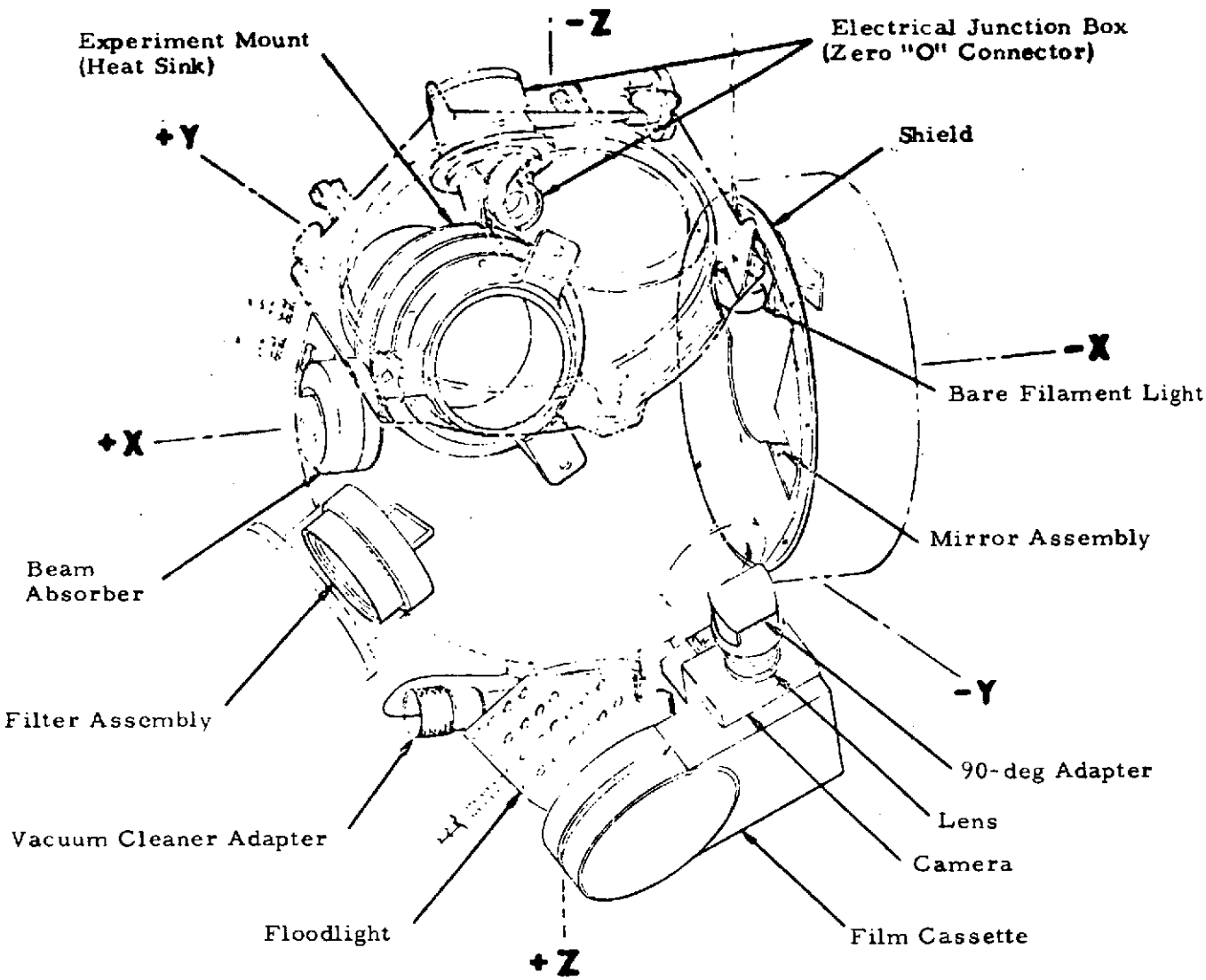

FIGURE 23. WORK CHAMBER ASSEMBLY

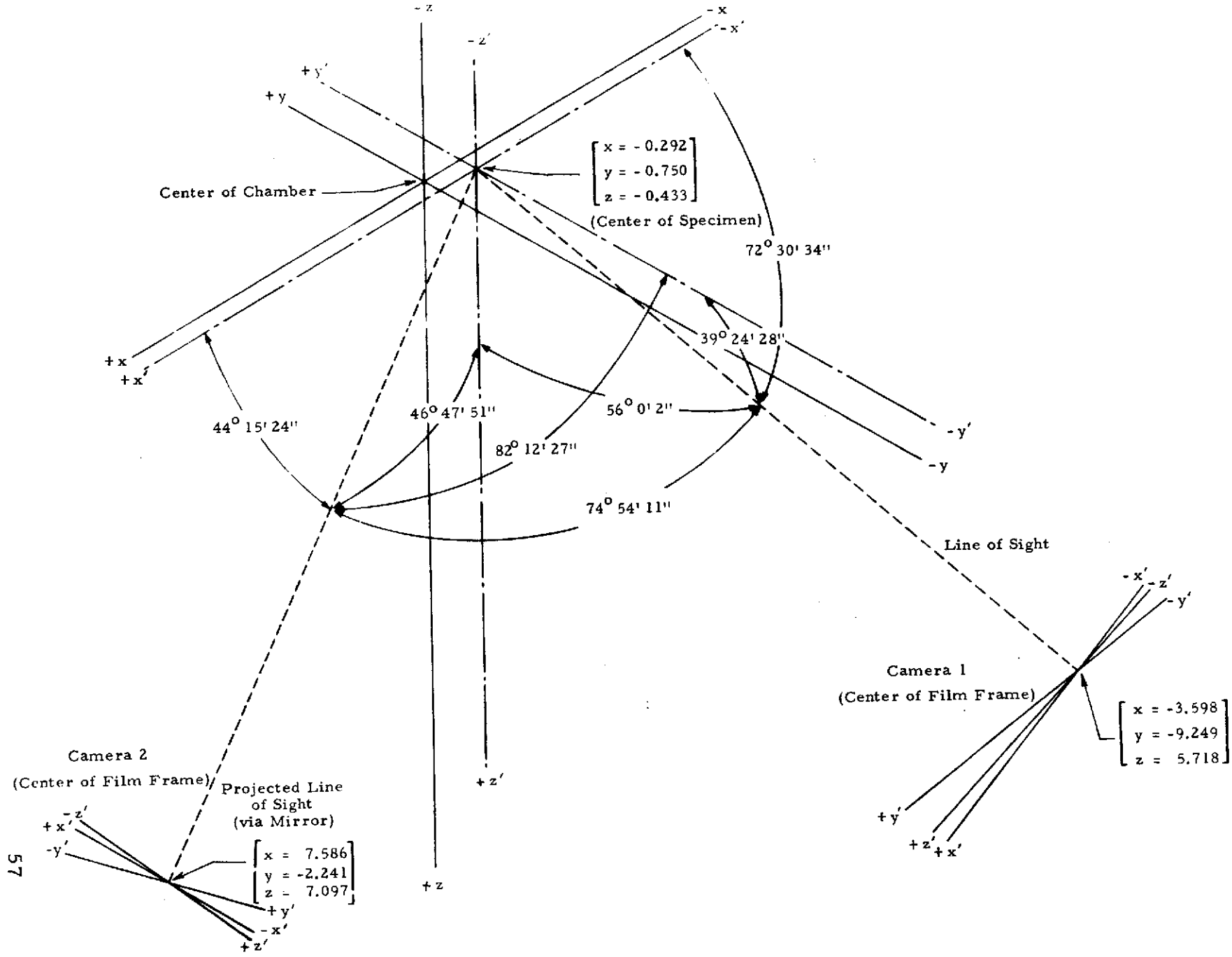

FIGURE 24. RELATIVE GEOMETRY OF M512 CHAMBER AND CAMERA ORIENTATION

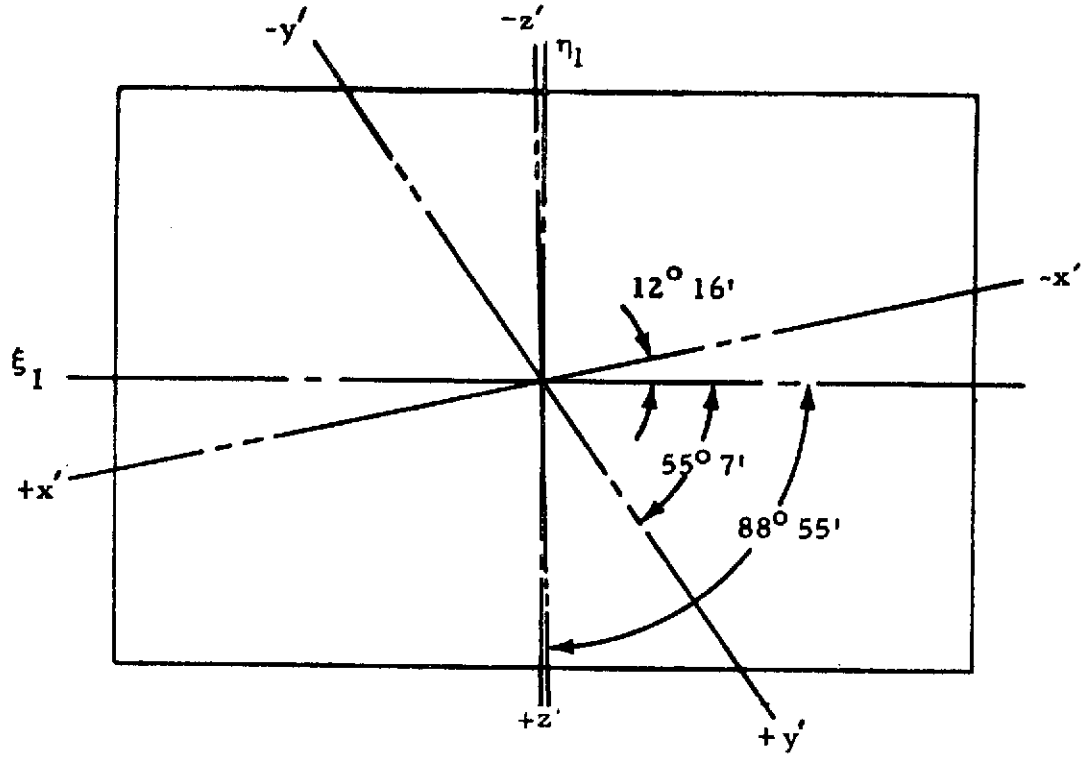

Camera 1 Film Frame

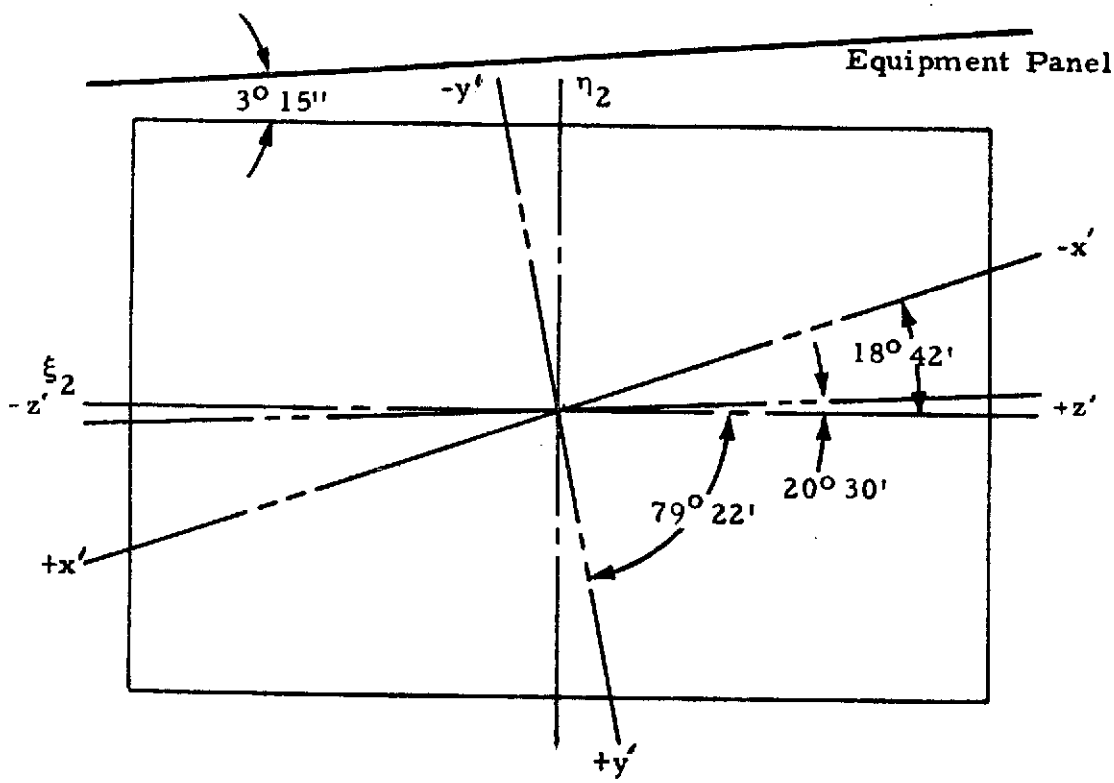

Camera 2 Film Frame

FIGURE 25. PROJECTION OF x'y'z' AXES ONTO FILM FRAME COORDINATE SYSTEM (POSITIVE NORMAL, ζ, IS INTO PLANE)

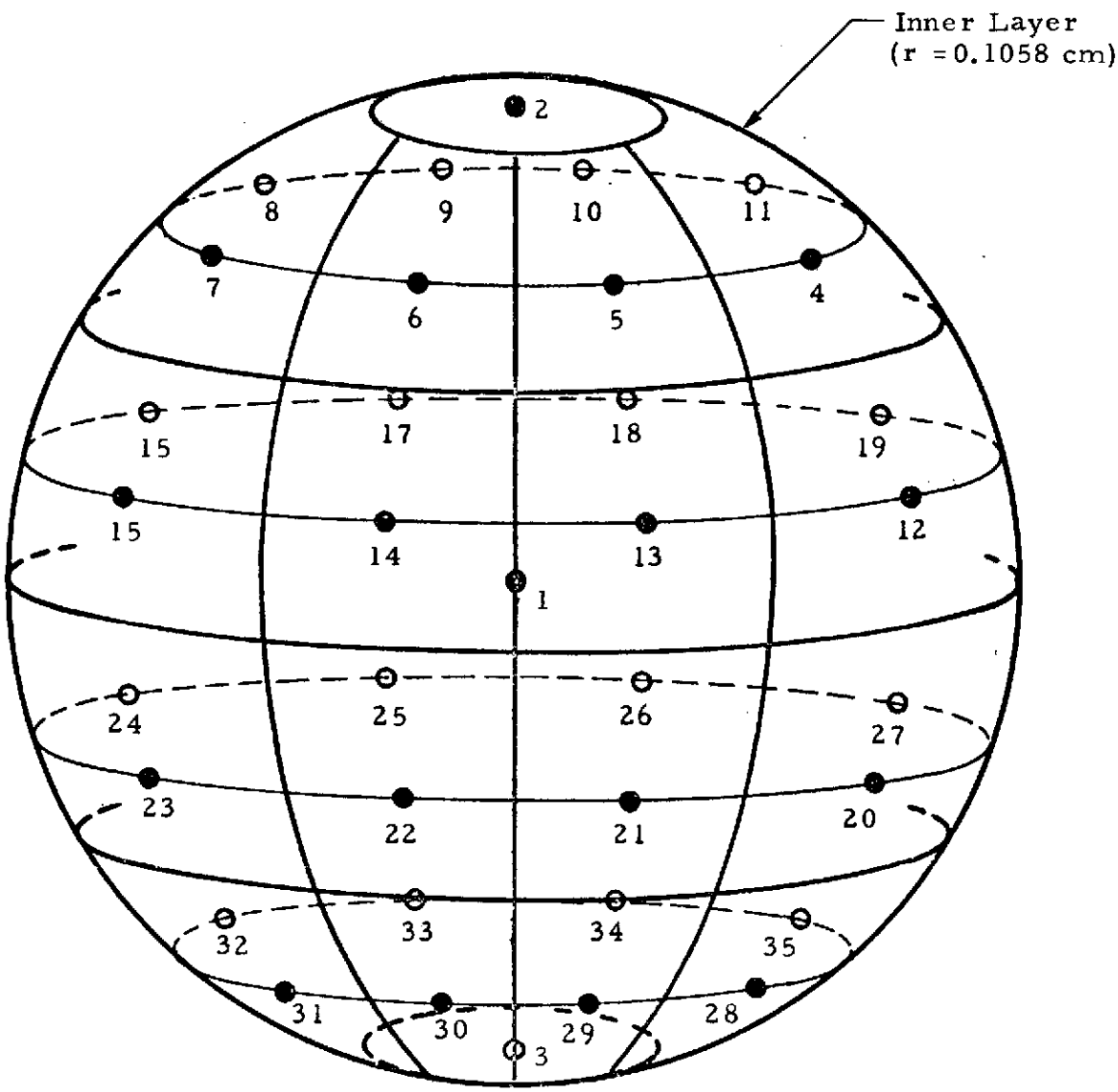

FIGURE 26. THERMAL MODEL FOR INNER LAYER

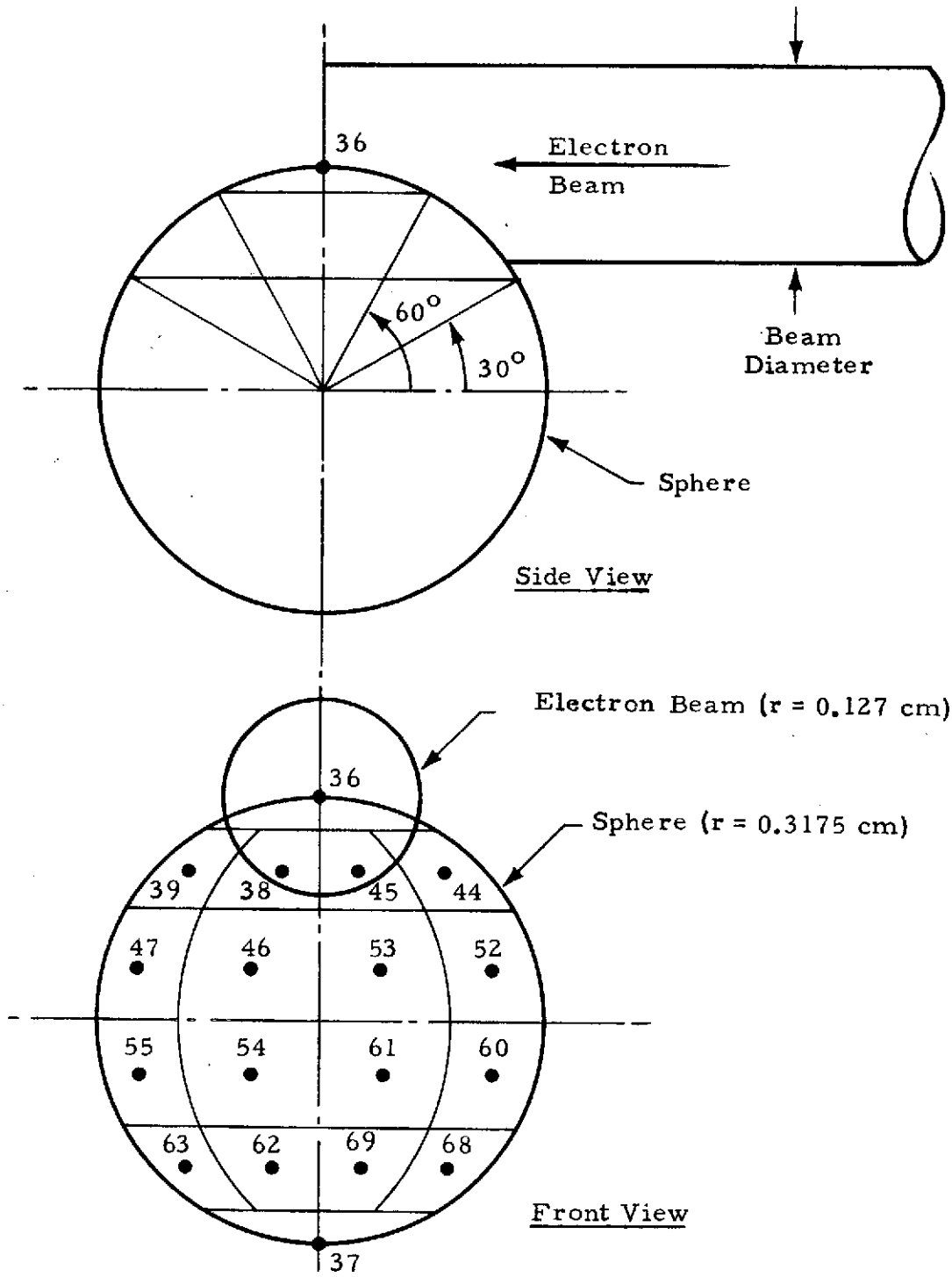

FIGURE 27. THE RELATIVE POSITION OF ELECTRON BEAM TO SPHERE AND THERMAL MODEL FOR OUTER LAYER

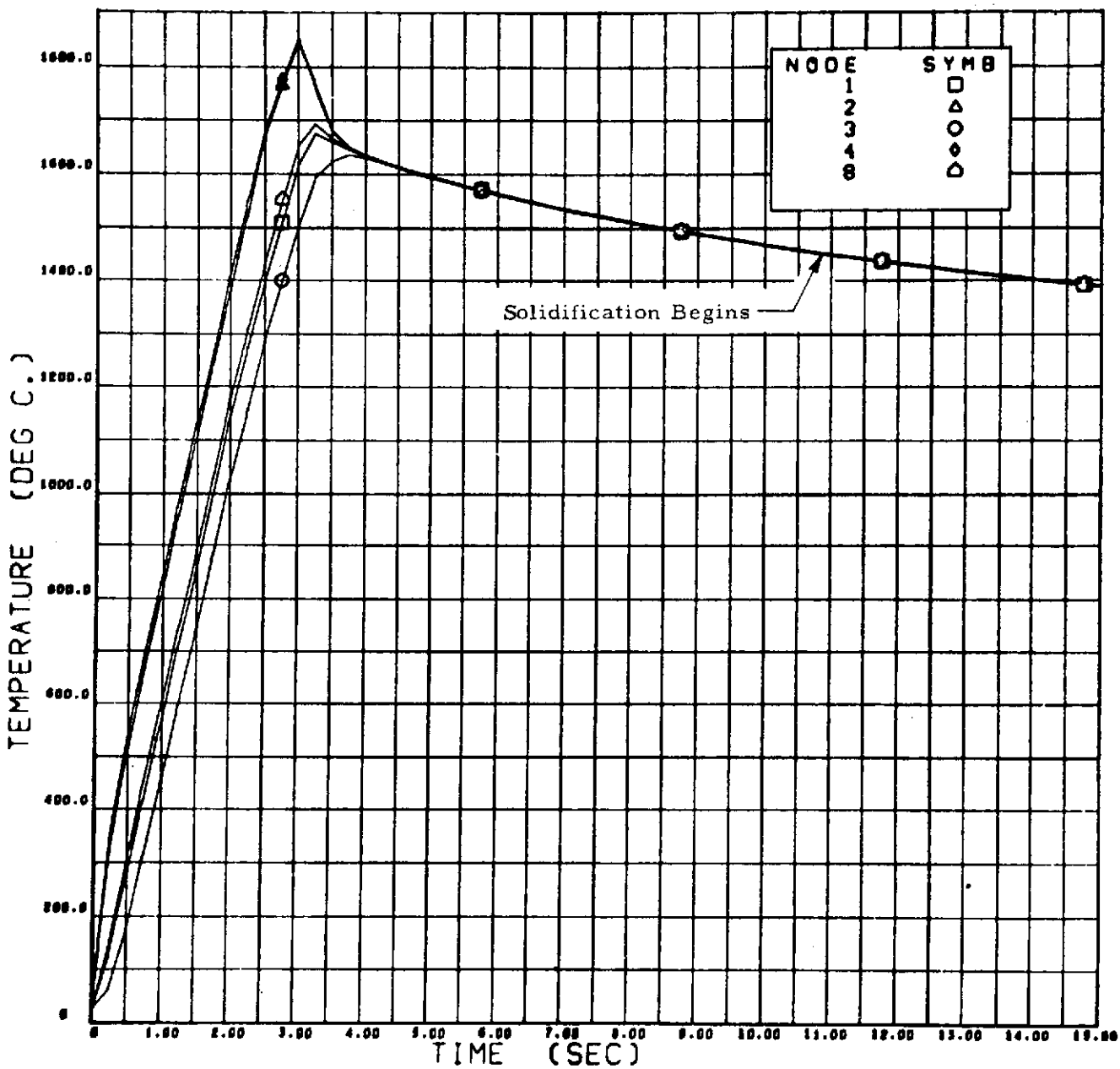

FIGURE 28. NICKEL TEMPERATURE HISTORY (NODES 1, 2, 3, 4 AND 8)

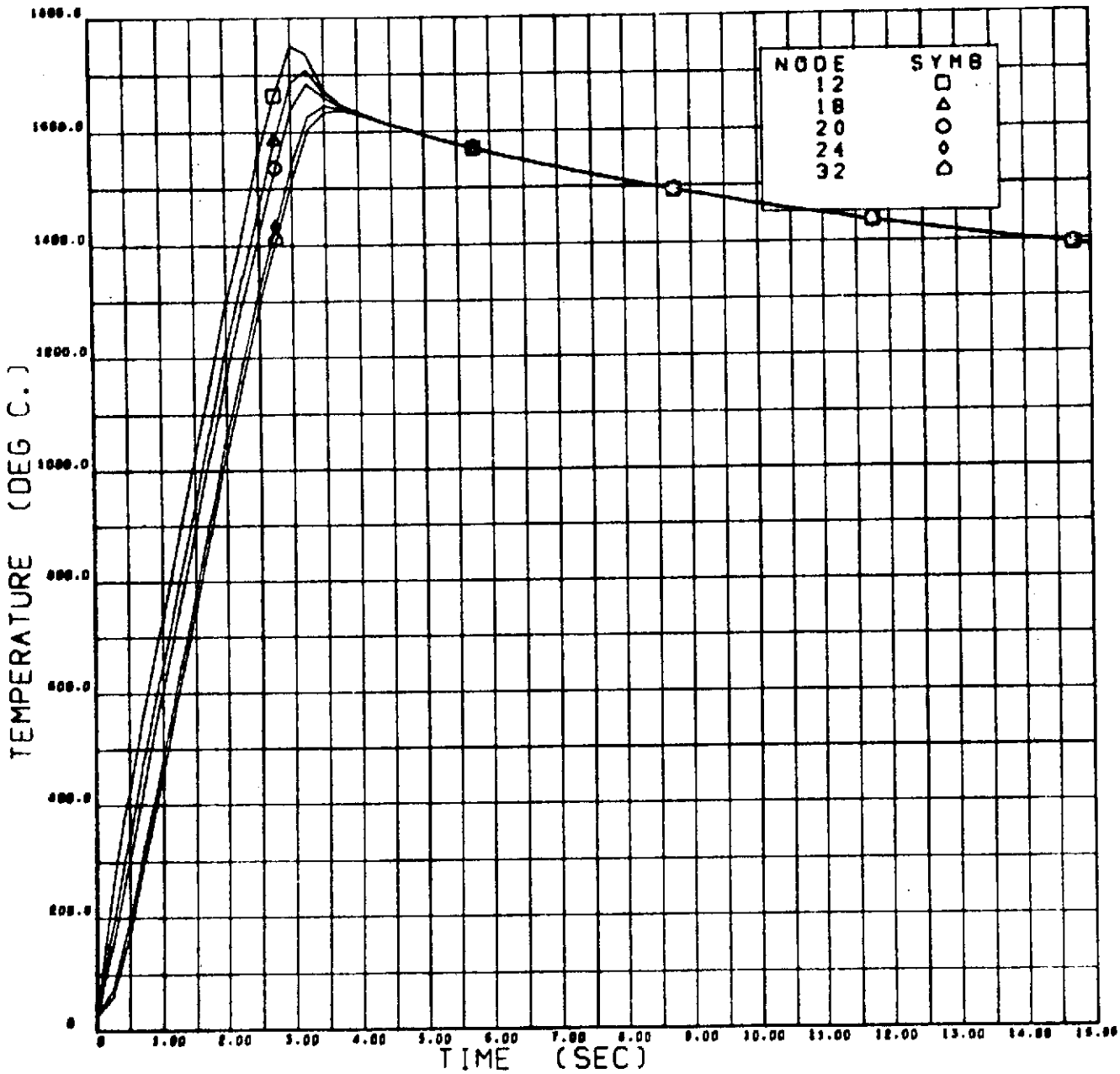

FIGURE 29. NICKEL TEMPERATURE HISTORY (NODES 12, 18, 20, 24 AND 32)

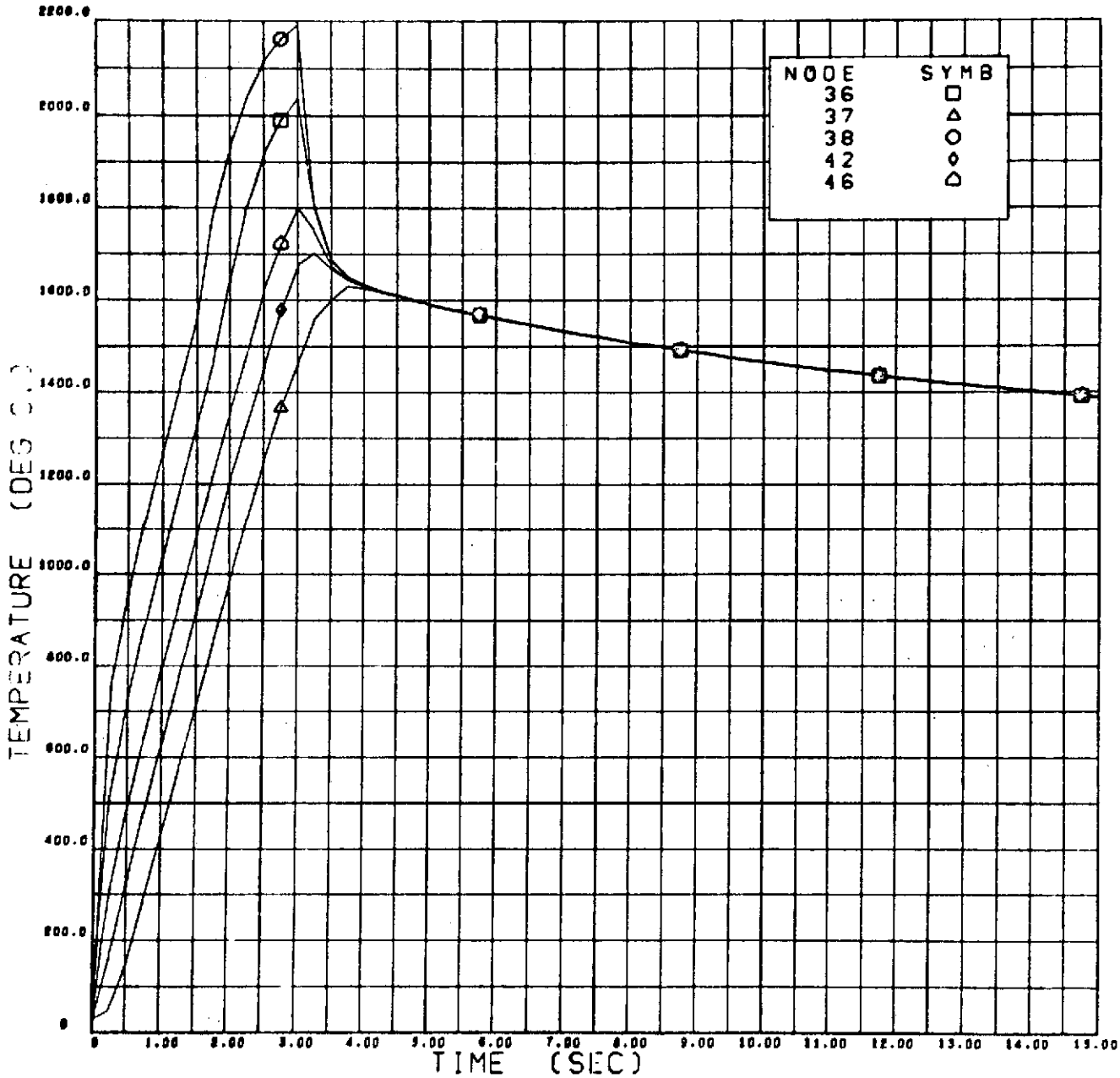

FIGURE 30. NICKEL TEMPERATURE HISTORY (NODES 36, 37, 38, 42 AND 46)

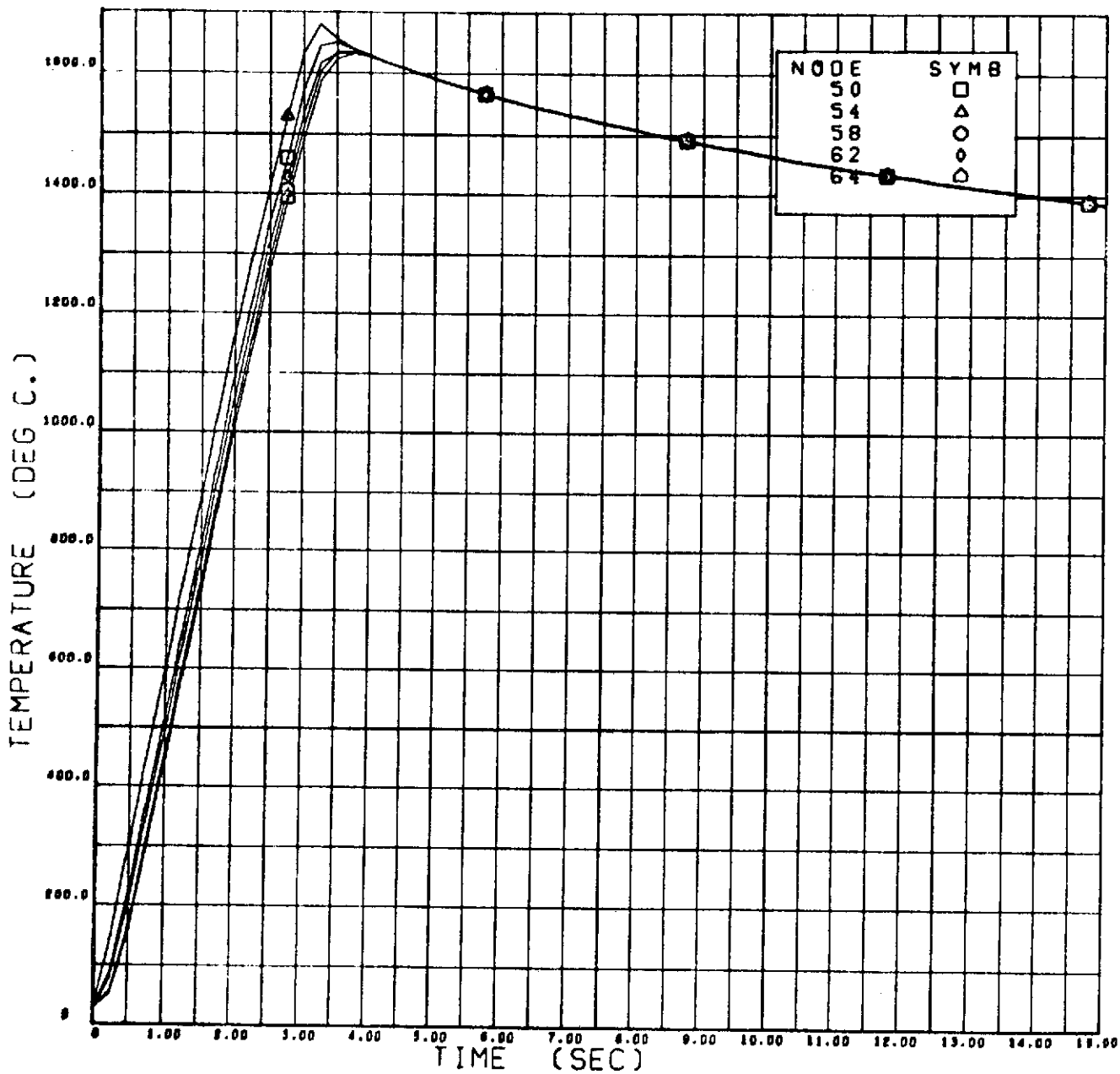

FIGURE 31. NICKEL TEMPERATURE HISTORY (NODES 50, 54, 58, 62 AND 64)

for Ni-12% Sn, Ni-1% Ag and Ni-30% Cu are shown in Figures 32 through 35, 36 through 39 and 40 through 43, respectively. The essential features of these results are as follows:

- Vaporization forces can be computed
- Time above melt temperature can be determined, and
- Superheat can be determined.

These items either affect the free-float time directly or the time duration needed for solidification. The solidification time including both vaporization and radiation losses for all four materials has been computed based on the methodology of Section II. These results are summarized in Table 6 for the M553 materials. These calculations indicate that from 32 to 48 seconds are necessary for complete solidification to occur.

Unfortunately, provision was not made during the Skylab flight tests for temperature measurements. Ground test measurements were made, however, and reported in Reference [8]. The measured temperatures represent a spatial average over the observed sphere surface (near the impingement point) and a time average for a period on the order of one or two seconds after electron beam cutoff. For the pure nickel specimens, the maximum measured temperature was about 1500°C for the sting-type specimens and about 1450°C for the release specimens. Figures 28 and 29 show predicted "average" temperatures of about 1600°C for the one or two second time period after beam cutoff. An emittance correction for the sample could have raised the measured temperature by about 100°C thus giving good agreement between the predicted and measured results [8]. The maximum measured temperature for the nickel-12% tin specimens was about 1400°C, which after emittance corrections could be increased to about 1500°C. This is about 100°C less than the 1600°C predicted average indicated in Figures 32 through 36. The maximum measured temperature for the nickel-1% silver specimens was also about 1400°C with possible emittance correction to 1500°C, and this also compares to a predicted value of about 1600°C indicated in Figures 36 through 39. For the nickel-30% copper specimens, a maximum measured value of about 1350°C compares to a predicted value (from Figures 40 through 43) of about 1425°C, thus giving good agreement if emittance corrections increased the measured values by 50 to 100°C.

Table 6

THERMAL SUMMARY

Material	eb Time (sec)	T_{melt} (°C)	Maximum Superheat (°C)	Average Superheat (°C)	Solidification Initialization (sec)	Solidification Time (sec)	Total Time (sec)
Ni	2.98	1455	228	91	10.7	25	36
Ni-12% Sn	2.65	1370	330	132	12.0	36	48
Ni-1% Ag	3.01	1454	210	84	9.3	23	32
Ni-30% Cu	2.30	1357	98	39	7.3	30	38

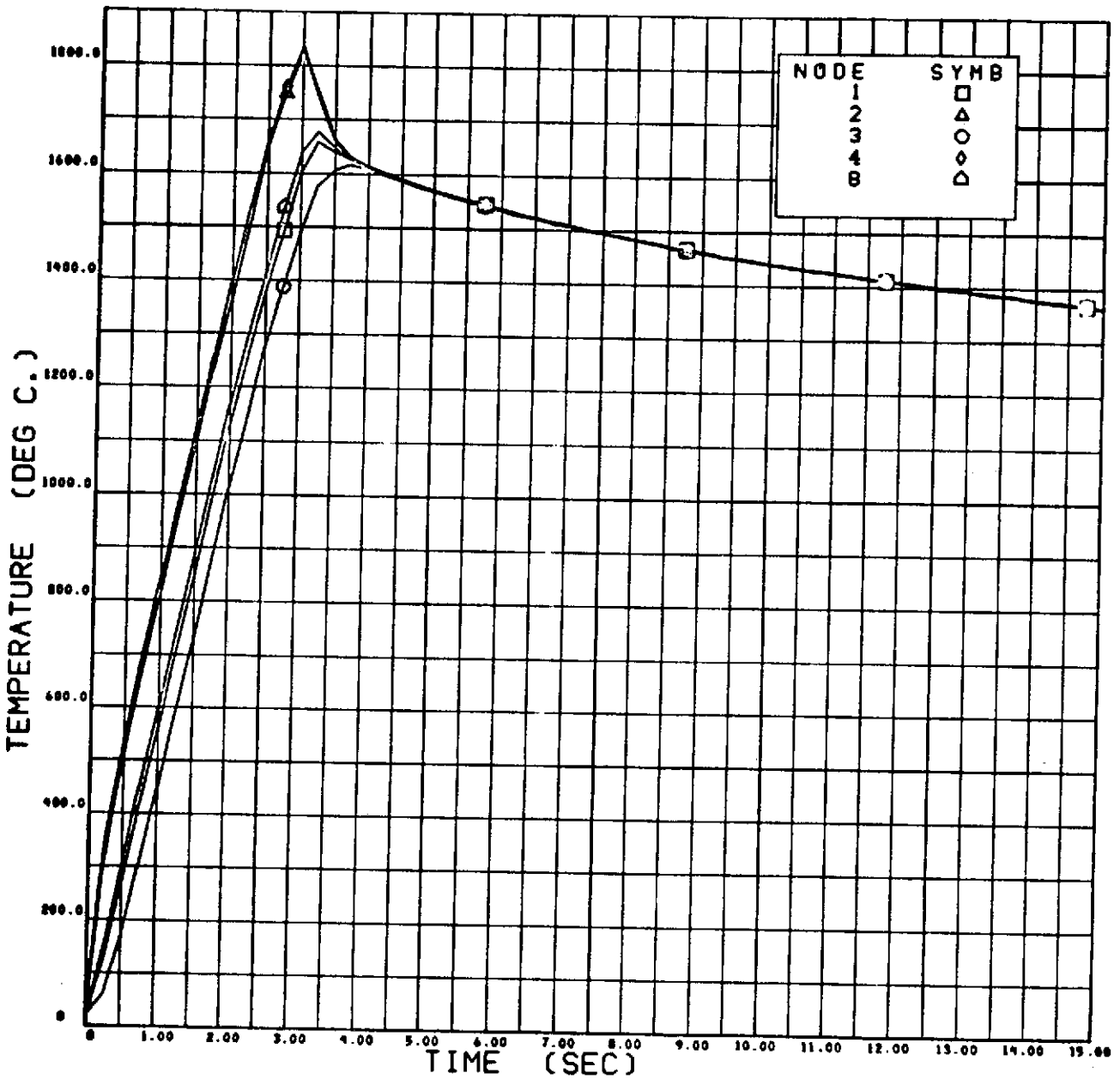

FIGURE 32. NICKEL-12% TIN TEMPERATURE HISTORY (NODES 1, 2, 3, 4 AND 8)

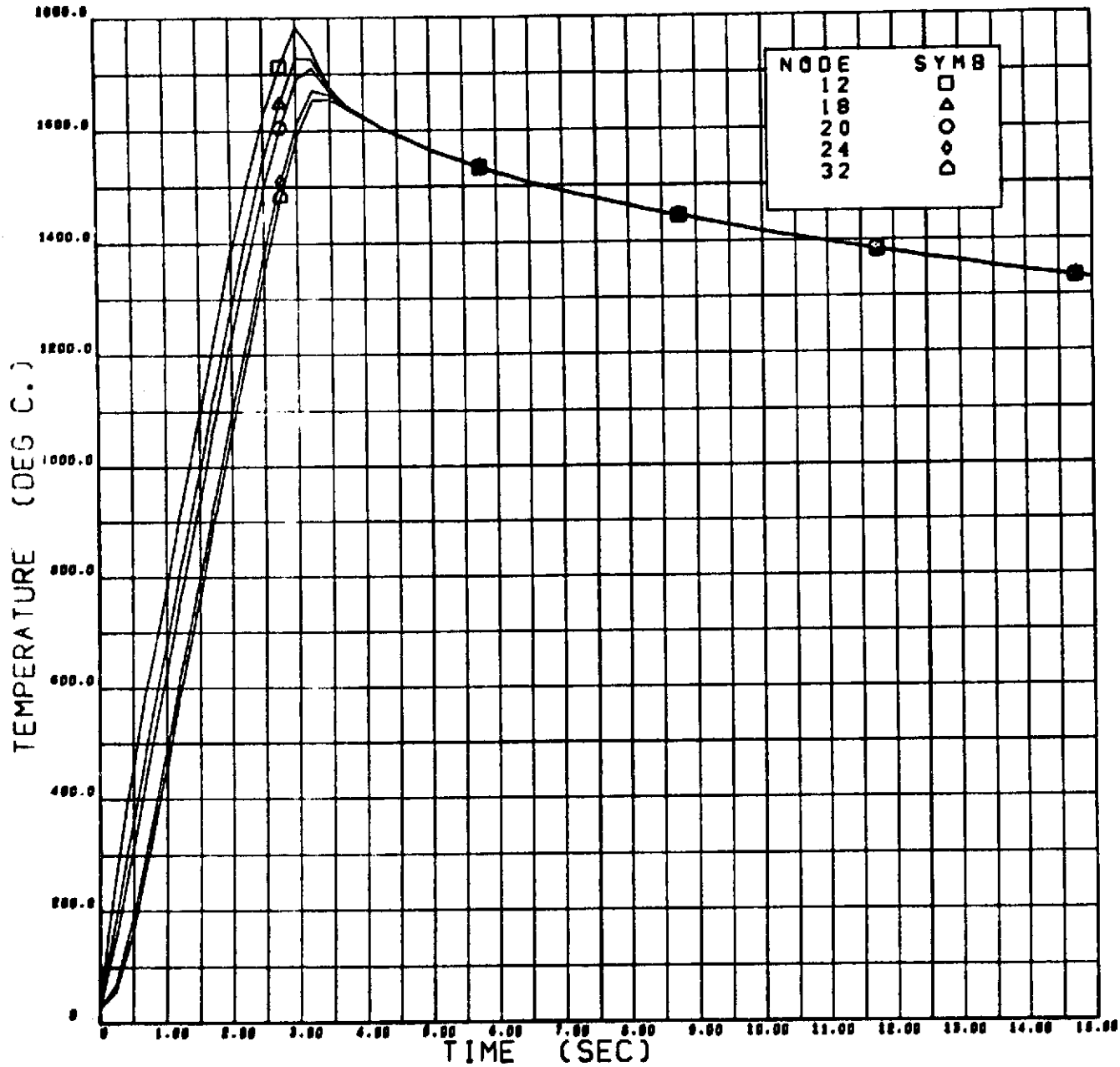

FIGURE 33. NICKEL-12% TIN TEMPERATURE HISTORY (NODES 12, 18, 20, 24 AND 32)

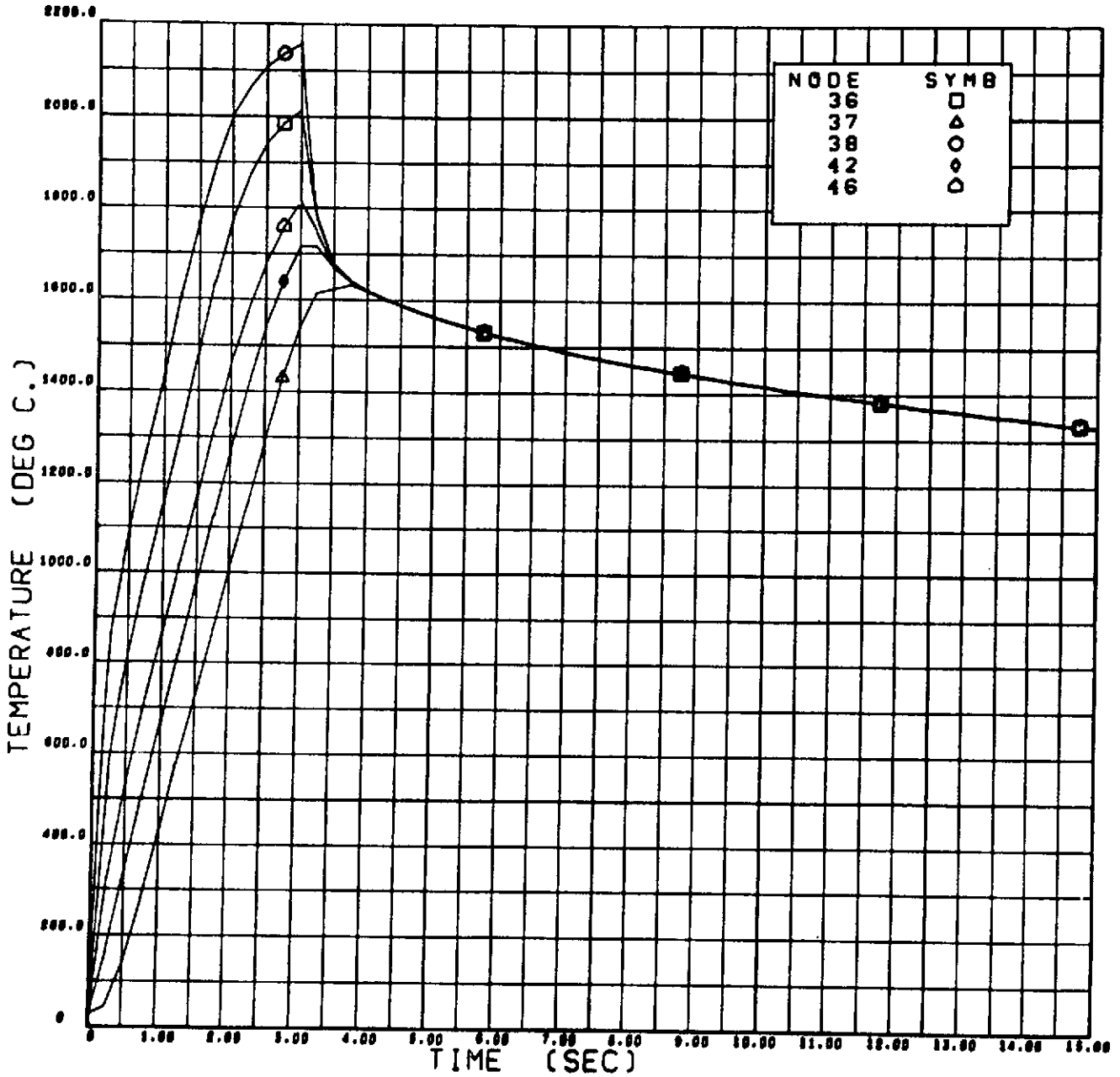

FIGURE 34. NICKEL-12% TIN TEMPERATURE HISTORY (NODES 36, 37, 38, 42 AND 46)

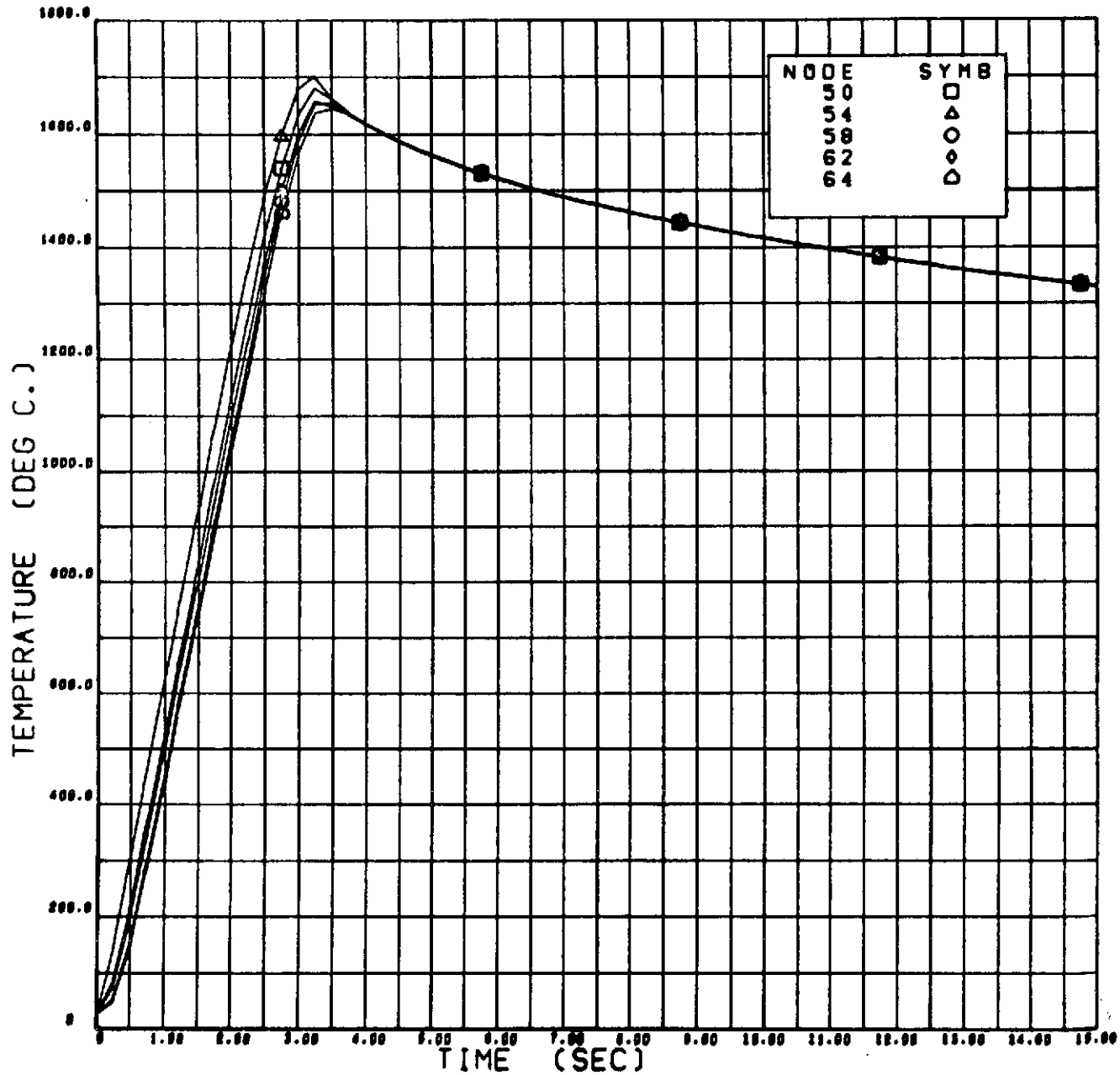

FIGURE 35. NICKEL-12% TIN TEMPERATURE HISTORY (NODES 50, 54, 58, 62 AND 64)

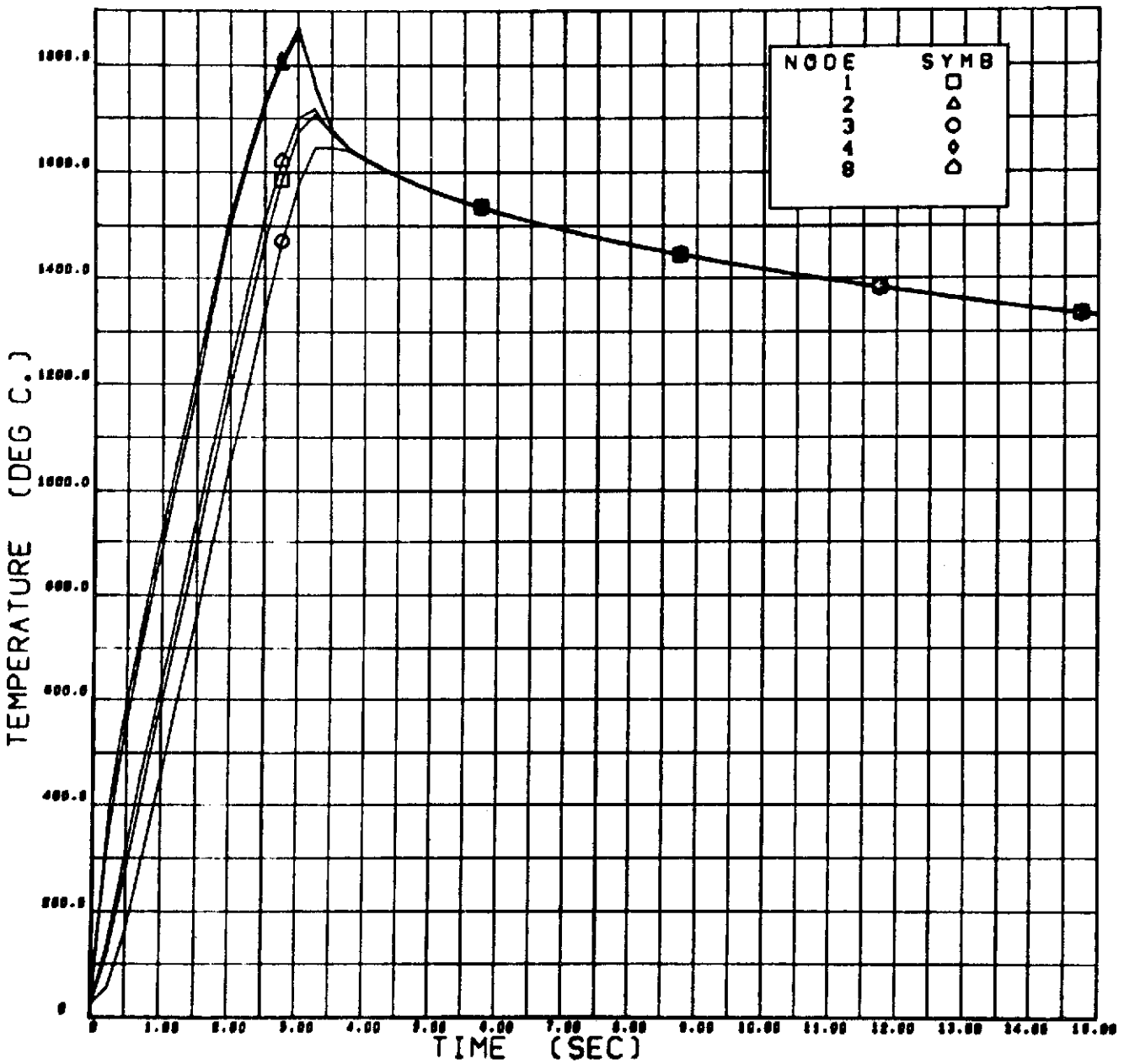

FIGURE 36. NICKEL-1% SILVER TEMPERATURE HISTORIES (NODES 1, 2, 3, 4 AND 8)

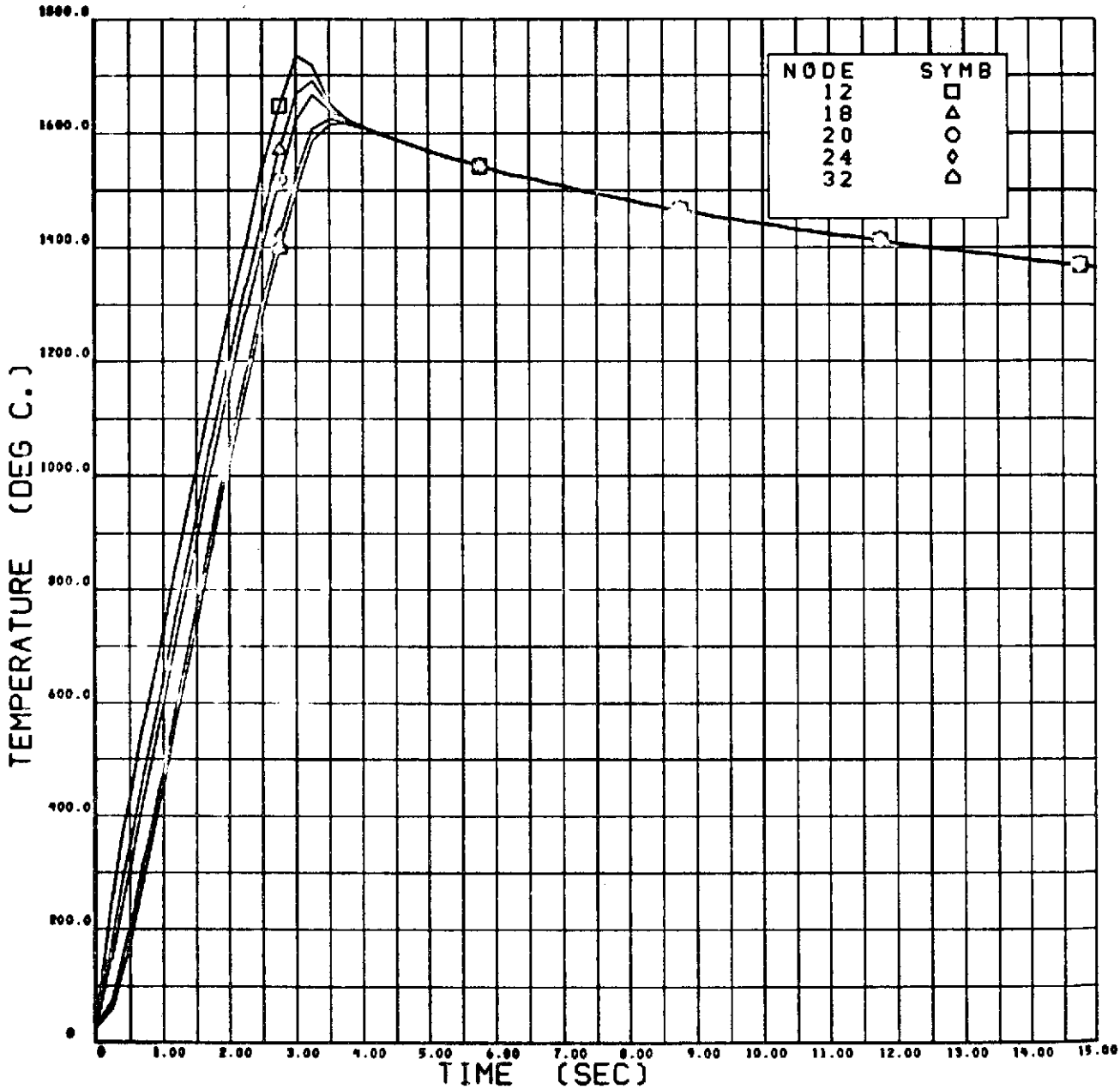

FIGURE 37. NICKEL-1% SILVER TEMPERATURE HISTORIES (NODES 36, 37, 38, 42 AND 46)

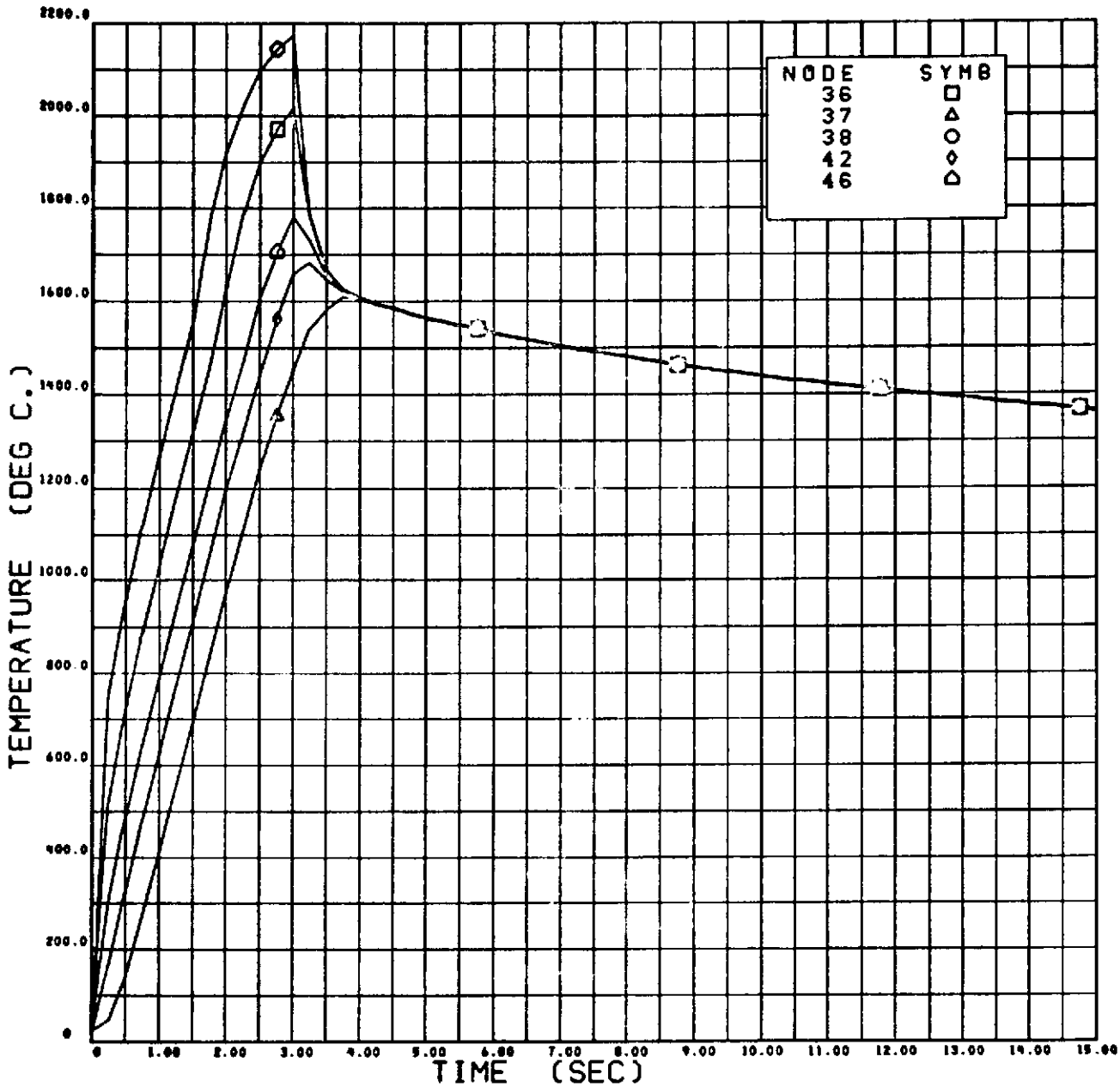

FIGURE 38. NICKEL-1% SILVER TEMPERATURE HISTORIES (NODES 36, 37, 38, 42 AND 46)

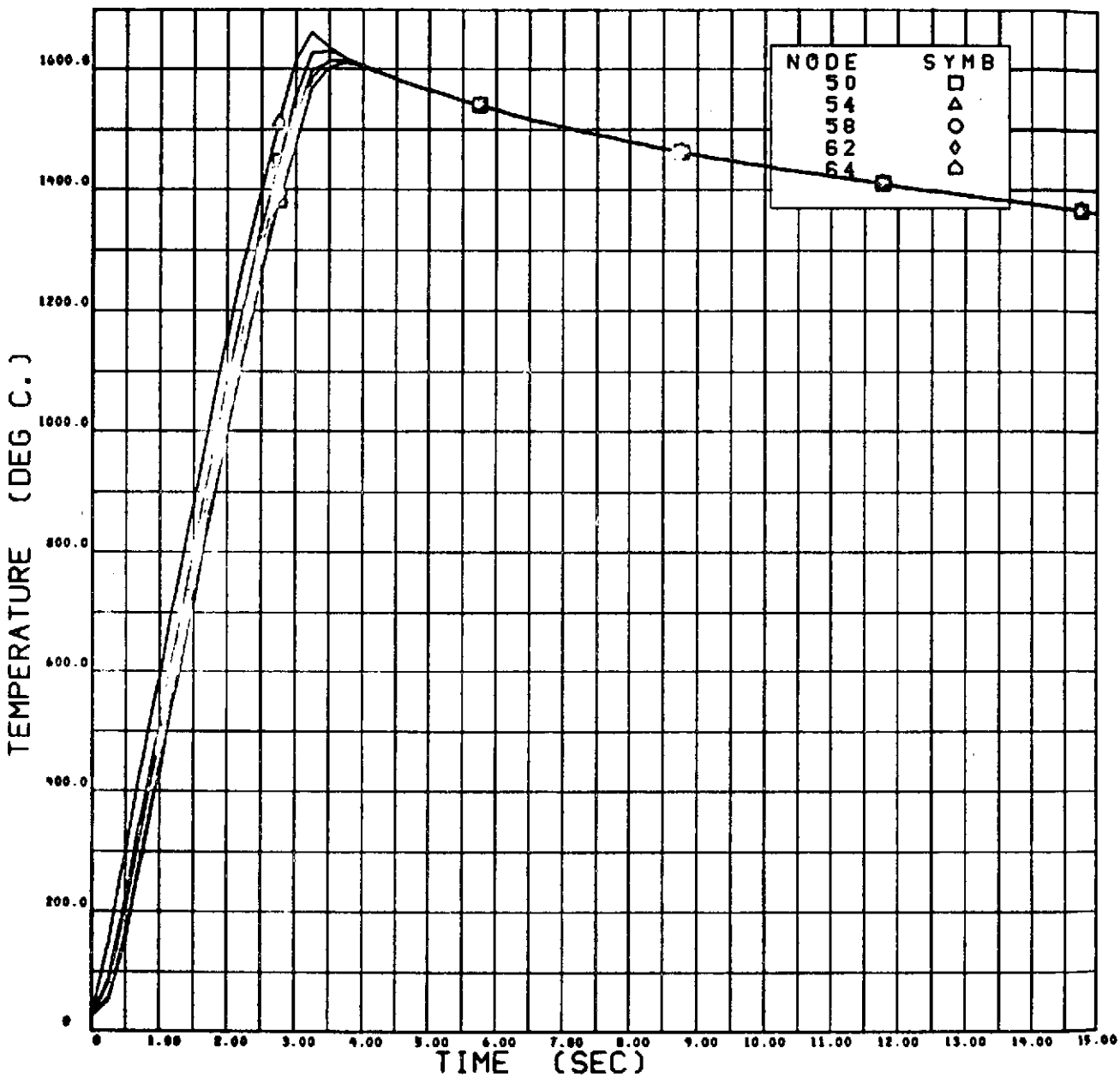

FIGURE 39. NICKEL-1% SILVER TEMPERATURE HISTORIES (NODES 50, 54, 58, 62 AND 64)

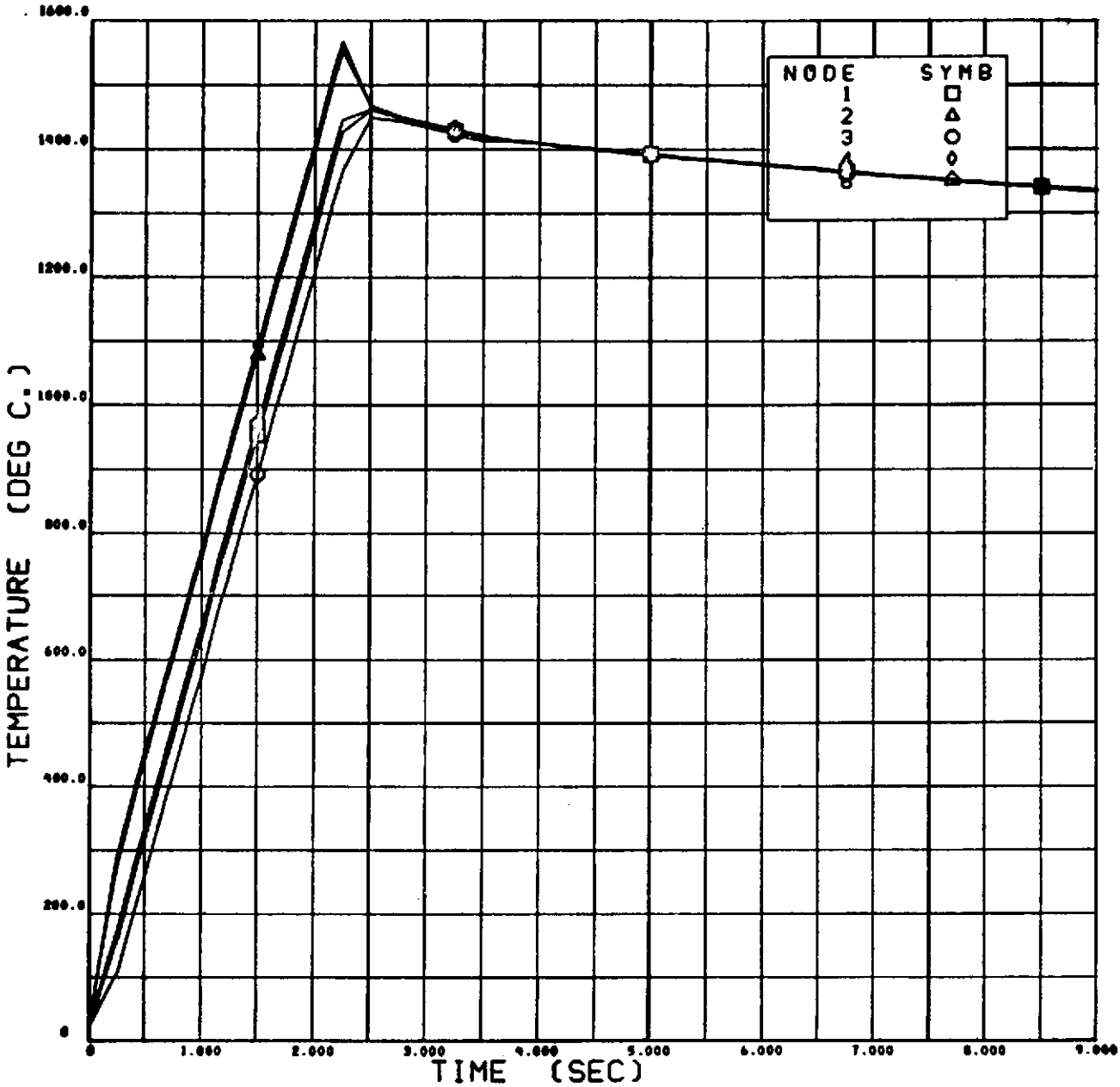

FIGURE 40. NICKEL-30% COPPER TEMPERATURE HISTORIES (NODES 1, 2, 3, 4 AND 8)

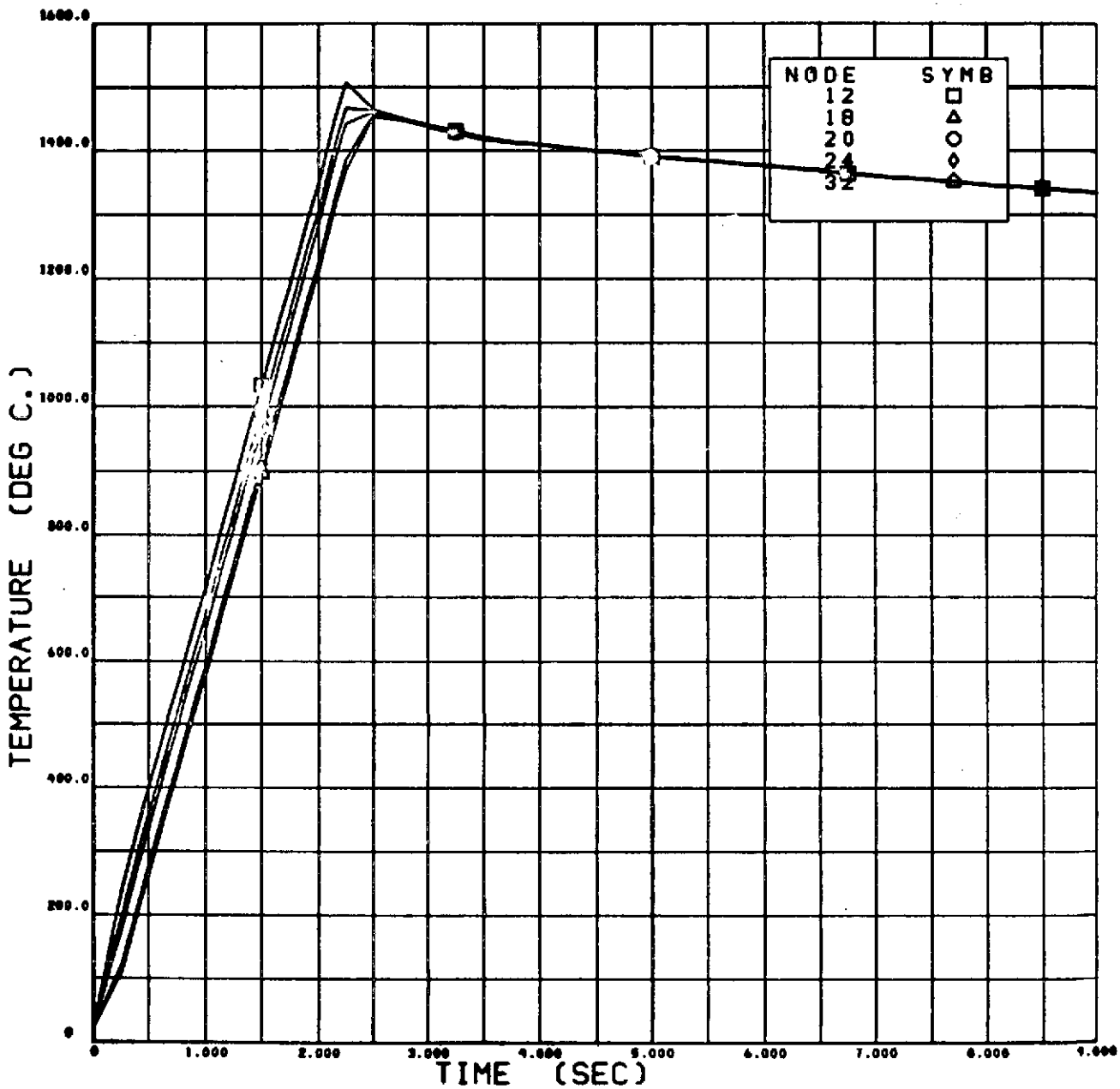

FIGURE 41. NICKEL-30% COPPER TEMPERATURE HISTORIES (NODES 12, 18, 20, 24 AND 32)

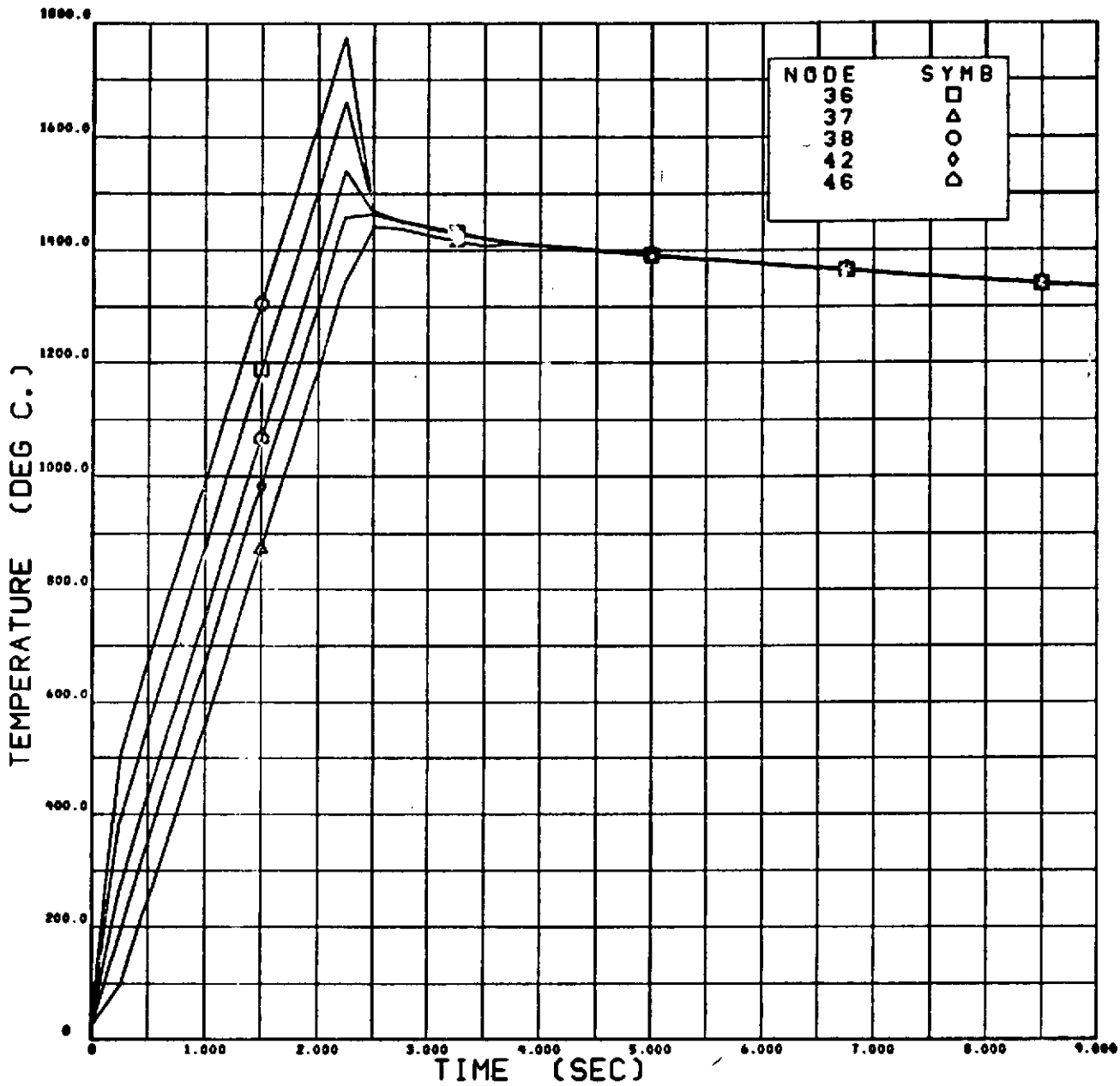

FIGURE 42. NICKEL-30% COPPER TEMPERATURE HISTORIES (NODES 36, 37, 38, 42 AND 46)

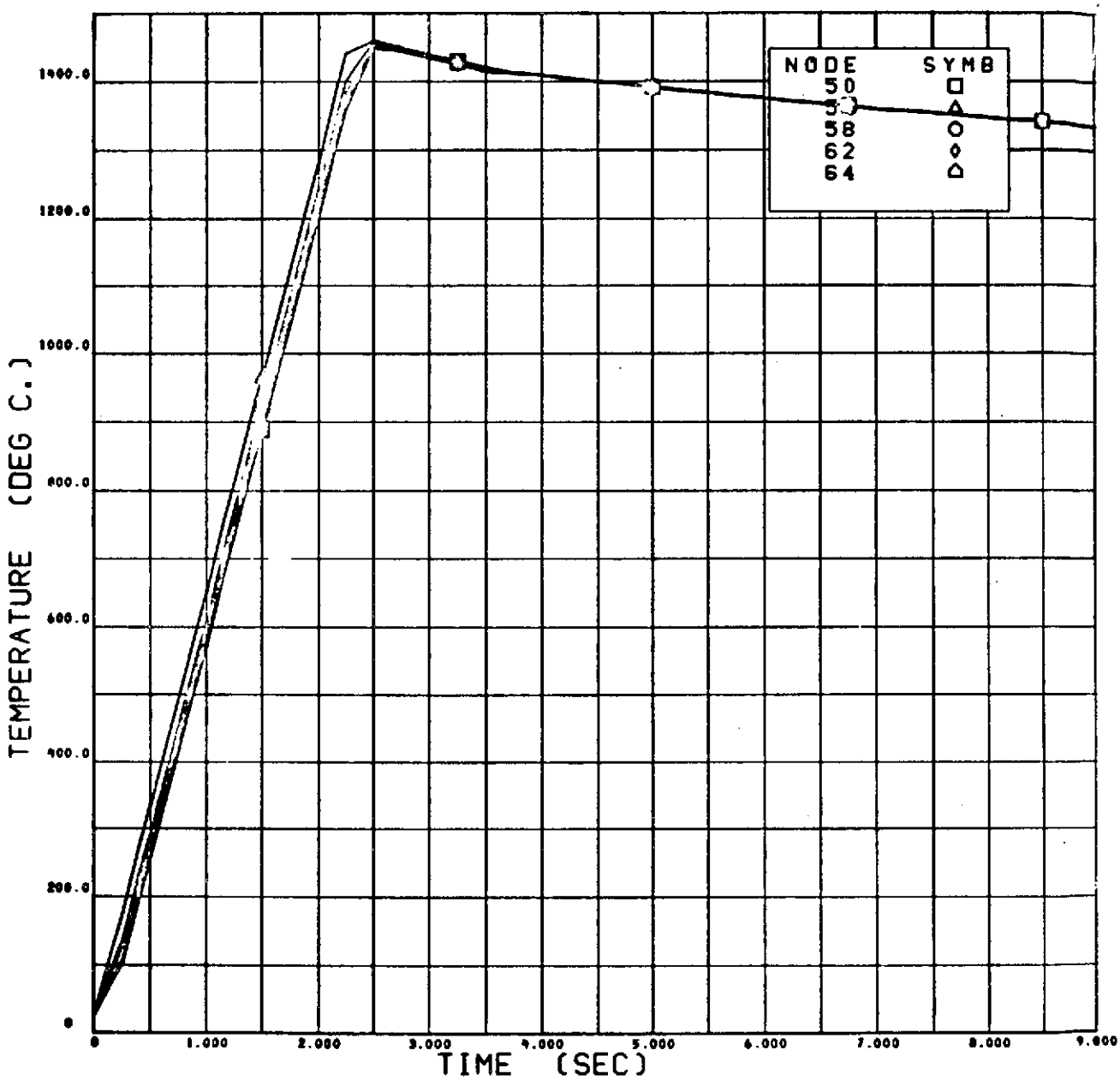

FIGURE 43. NICKEL-30% COPPER TEMPERATURE HISTORIES (NODES 50, 54, 58, 62 AND 64)

D. M553 TRAJECTORY ANALYSIS

One of the most important aspects of the M553 experiment is the motion of the sphere after deployment since this determines what free-float time will exist. In order to predict the motion, a trajectory program has been developed that includes allowances for:

- Electron beam force
- Deployment velocity (spring)
- Vaporization force based on 3-D temperature history
- Skylab orbit considerations
- M512 position considerations, and
- Allowances for additional forces as independent subroutines (KC-135 g-level data).

In general a solution to the equation of motion

$$\frac{d^2\vec{R}}{dt^2} = \vec{f}(t) \tag{58}$$

is obtained numerically via Simpson's rule subject to the following boundary conditions:

$$\vec{R} = 0 \text{ and } \frac{d\vec{R}}{dt} = \vec{V}_o \text{ at } t = 0 \tag{59}$$

Integration of the equation of motion twice yields

$$\vec{R} = t\,\vec{V}_o + \int_o^t \int_o^\eta \vec{f}\,(\xi)\,d\xi\,d\eta \tag{60}$$

which produces the desired trajectory in chamber coordinates centered on the specimen. This computed trajectory is then transformed to camera coordinates to show the path as seen in the film, i.e.,

$$\vec{R}'(t) = [A]\,\vec{S}(t) \tag{61}$$

where $\vec{R}'(t)$ is the projected trajectory and $[A]$ is the transformation matrix obtained from the hardware. For camera 1

$$[A] = \begin{bmatrix} .932 & -.363 & 0 \\ -.203 & -.521 & -.829 \\ .301 & .773 & -.560 \end{bmatrix} \quad (62)$$

and for camera 2

$$[A] = \begin{bmatrix} .661 & -.183 & -.728 \\ -.224 & -.974 & .041 \\ -.716 & .136 & .685 \end{bmatrix} \quad (63)$$

To demonstrate the concept, consider the accelerometer data in Table 7. These data were obtained by orthogonal accelerometers placed on board the July 1972 KC-135 research aircraft flight. The resulting directions of the residual g-level are shown in Figure 44 transformed into both camera planes.

The tabular gravity levels appear in Table 8 in film plane coordinates. The resulting float time as a function of the magnitude of the gravity level is shown in Figure 45 for a spherical outer boundary 20 cm from specimen release. It is seen that float times of 1 to 3 seconds can be expected in the KC-135 flights for g-levels of $6(10)^{-2}$ to $0.6(10)^{-2}$.

The eb force was discussed in Section II and Table 9 gives the magnitude of this force for two eb currents. To establish the motion as a result of the eb force, the conversion efficiency and eb cutoff time must be known. This time corresponds to the time delay associated with automatic shutdown of the eb due to sting melting. Original estimates were from 10 to 20 milliseconds; however, high speed movies (1000 frame/sec) taken during the M553 ground-based test at MSFC on 20 October 1972 show conclusively that longer times exist. During their test the spring loads were varied on the shutdown mechanism to experimentally establish the time interval the eb is on after melting occurs. It was found that for a 150-g spring load a cutoff time of 410 milliseconds was measured while 220 milliseconds were observed for a 200-g load. This cutoff time translates into a free-float time of approximately 12 seconds for a 150-g load and 23 seconds for the 200-g load. Thus the expected free-float time is drastically reduced from the 250 seconds corresponding to the original 20 milliseconds estimate.

An analysis was performed to determine if the cohesive energy-generated kinetic energy is sufficient to cause deployment in the absence of external forces. This was done to allow initial conditions

Table 7

ACCELEROMETER DATA FROM JULY KC-135 FLIGHT

Index	Specimen	$a_x(10)^2$ (g)	$a_y(10)^2$ (g)	$a_z(10)^2$ (g)	$\|g\|(10)^2$ (g)
1	10	1.0	-1.0	3.0	3.4
2	9	0.5	0.3	0.3	0.65
3	8	-0.4	0.3	4.0	4.05
4	14	0.0	0.2	2.0	2.02
5	11	-1.0	-0.7	2.0	2.34
6	7	0.5	-0.4	1.0	1.19
7	6	0.6	-0.1	1.5	1.65
8	5	1.4	-1.0	4.5	4.82
9	2	1.5	-2.2	-2.2	3.14
10	15	-0.4	-0.4	-1.0	1.15
11	13	0.2	-0.4	5.8	5.82

Table 8

TRANSFORMED KC-135 ACCELEROMETER DATA

Camera 1				
Index	Specimen	ξ_1	η_1	ζ_1
1	10	1.290	-2.170	-2.150
2	9	0.357	-0.506	0.214
3	8	-0.482	-3.390	-2.125
4	14	-0.073	-1.762	-0.964
5	11	-0.678	-1.090	-1.960
6	7	0.611	-0.722	-0.718
7	6	0.596	-1.313	-0.736
8	5	1.670	-3.490	-2.868
9	2	2.195	2.666	-0.019
10	15	-0.228	1.119	0.130
11	13	0.331	-4.641	-3.492

Camera 2				
Index	Specimen	ξ_2	η_2	ζ_2
1	10	-1.339	0.874	-2.906
2	9	0.057	-0.392	-0.523
3	8	-3.230	-0.038	-2.411
4	14	-1.492	-0.112	-1.342
5	11	-1.989	0.988	-0.748
6	7	-0.324	0.319	-1.097
7	6	-0.677	0.025	-1.470
8	5	-2.167	0.846	1.716
9	2	2.99	1.716	0.134
10	15	0.536	0.438	0.917
11	13	-4.016	0.584	-4.168

Table 9

TOTAL FORCE DUE TO ELECTRON BEAM

$$F_e = I \sqrt{\frac{2 m_e V}{e}}$$

I (amp)	e (coulomb)	m_e (kg)	V (V)	F_e (N)	F_e (dyne)
0.05	$1.6(10)^{-19}$	$0.9(10)^{-30}$	$2(10)^4$	$2.38(10)^{-5}$	2.38
0.10	$1.6(10)^{-19}$	$0.9(10)^{-30}$	$2(10)^4$	$4.76(10)^{-5}$	4.76

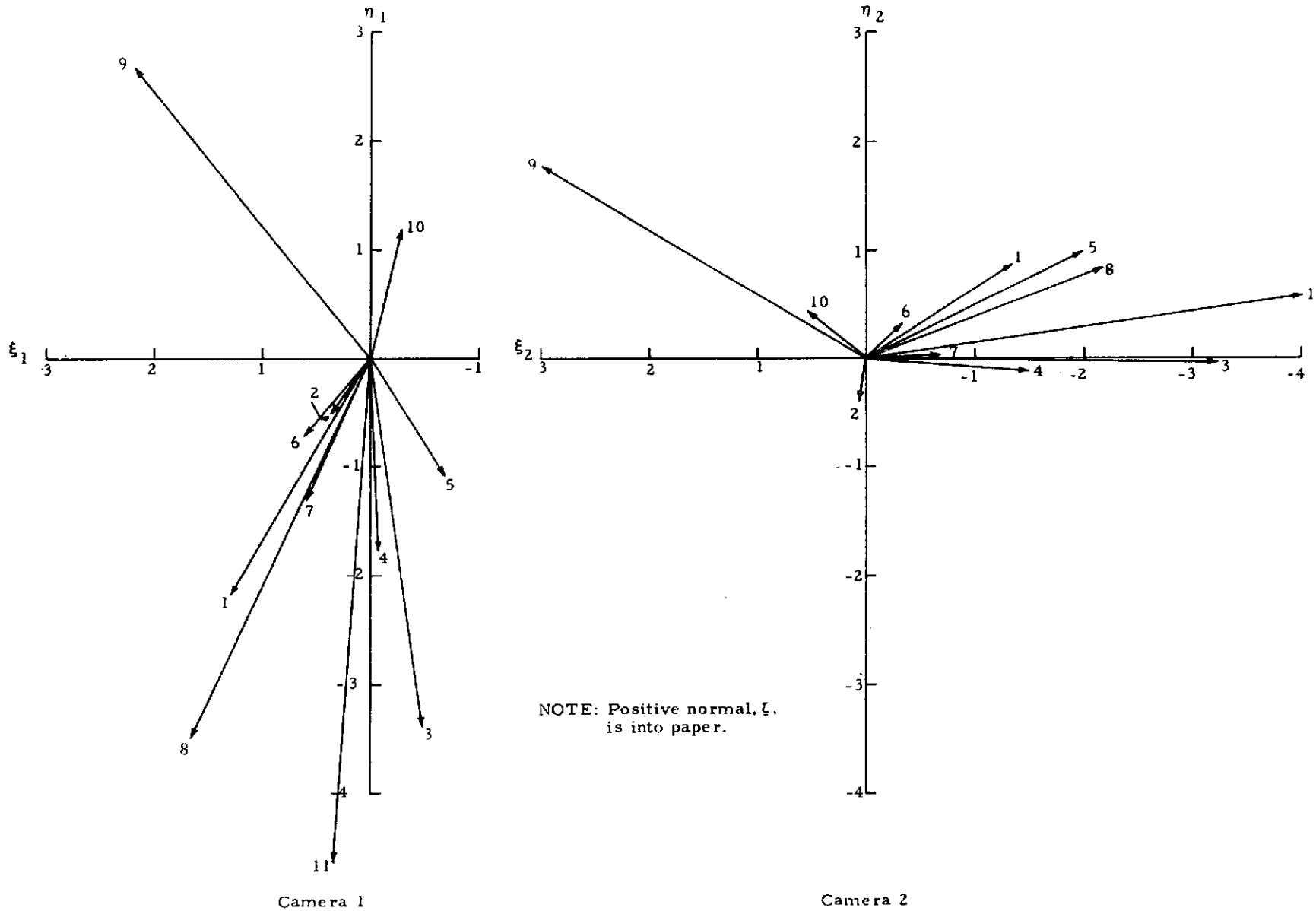

FIGURE 44. TRANSFORMED ACCELEROMETER DATA IN FILM PLANE

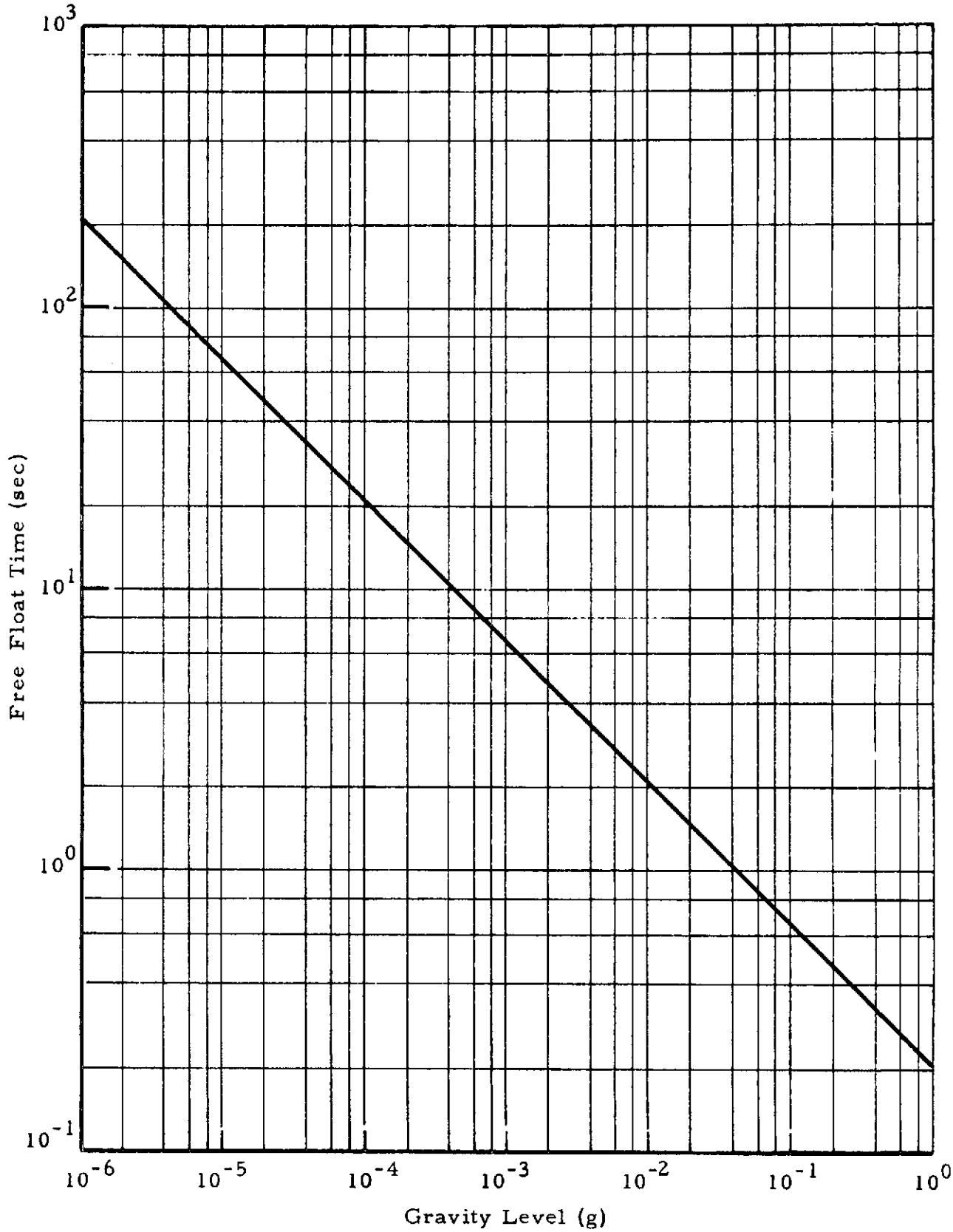

FIGURE 45. APPROXIMATE FLOAT TIME AS A FUNCTION OF GRAVITY LEVEL

to be calculated. To reduce the complexity of the problem, the following assumptions were made:

- Zero gravity field
- No sting melting
- Sting pulled down before breaking
- Perfectly spherical free surface, and
- Contact angle of 120 degrees.

An energy balance was made between the initial and final states and from this the kinetic energy is found as

$$KE = \sigma_{LV}\left(A_{LV}^{(i)} - A_{LV}^{(f)}\right) + \sigma_{LS}\left(A_{LS}^{(i)} - A_{LS}^{(f)}\right)$$

This kinetic energy was calculated as a function of penetration (H) of liquid into orifice. The value of H simulates the effect of the spring in pulling the liquid down via adhesion between liquid and solid sting. The results of this calculation are

Penetration, H (cm)	Kinetic Energy (ergs)
0.0	0.0
0.1	62.7
0.5	293.0
1.0	597.0

The value of the kinetic energy must then be greater than the work of adhesion (or energy of adhesion) for deployment to occur. The work of adhesion was found to be 265 ergs; thus for depressions of more the 0.5 cm deployment will occur due to cohesive effects alone. These criteria are included in the trajectory computer program to allow initial conditions for the numerical integration to be determined.

Tables 10 and 11 show the surface temperature distribution at 3.0 and 3.5 seconds, respectively, for Ni and Ni-12% Sn. These

Table 10

TEMPERATURE DISTRIBUTION AT 3.0 SECONDS

Node No.	Nickel		Nickel – 12% Tin	
	Temp. (°C)	Vapor Pressure (mm Hg/cm^2)	Temp. (°C)	Vapor Pressure (mm Hg/cm^2)
36	2036	.3959	2013	.7001
37	1463	.0006	1537	.0069
38	2193	.464	2157	.6965
39	1900	.0395	1903	.0962
40	1728	.0067	1757	.0253
41	1677	.0037	1716	.0168
42	1677	.0037	1716	.0168
43	1728	.0067	1757	.0254
44	1900	.0400	1903	.0963
45	2193	.4644	2157	.6965
46	1801	.0202	1815	.0602
47	1695	.0063	1731	.0266
48	1609	.0022	1663	.0132
49	1573	.0014	1634	.0096
50	1573	.0014	1634	.0096
51	1609	.0022	1663	.0132
52	1695	.0063	1731	.0266
53	1801	.0201	1815	.0602
54	1633	.0030	1680	.0159
55	1584	.0016	1642	.0105
56	1537	.0009	1605	.0069
57	1513	.0006	1586	.0056
58	1513	.0006	1586	.0056
59	1537	.0009	1605	.0069
60	1584	.0016	1642	.0105
61	1633	.0020	1680	.0158
62	1535	.0006	1602	.0049
63	1515	.0005	1585	.0041
64	1492	.0003	1567	.0033
65	1480	.0003	1557	.0030
66	1480	.0003	1557	.0030
67	1492	.0003	1567	.0033
68	1515	.0005	1585	.0041
69	1535	.0006	1602	.0049

Table 11

TEMPERATURE DISTRIBUTION AT 3.5 SECONDS

Node No.	Nickel		Nickel-12% Tin	
	Temp. (°C)	Vapor Pressure (mm Hg/cm^2)	Temp. (°C)	Vapor Pressure (mm Hg/cm^2)
36	1689	.01249	1678	.0332
37	1601	.00429	1624	.0185
38	1685	.0041	1676	.0111
39	1679	.0038	1674	.0109
40	1672	.0035	1671	.0105
41	1667	.0033	1670	.0103
42	1667	.0033	1670	.0103
43	1672	.0035	1671	.0105
44	1679	.0038	1674	.0109
45	1685	.0041	1676	.0111
46	1675	.0050	1672	.0144
47	1668	.0046	1669	.0140
48	1658	.0041	1665	.0135
49	1652	.0038	1662	.0131
50	1652	.0038	1662	.0131
51	1658	.0041	1665	.0135
52	1668	.0046	1669	.0140
53	1675	.0050	1672	.0144
54	1657	.0040	1663	.0131
55	1651	.0037	1660	.0128
56	1642	.0033	1657	.0123
57	1636	.0031	1654	.0200
58	1636	.0031	1654	.0200
59	1642	.0033	1657	.0123
60	1651	.0037	1660	.0128
61	1657	.0040	1663	.0131
62	1634	.0022	1649	.0083
63	1630	.0021	1648	.0082
64	1624	.0020	1645	.0080
65	1621	.0019	1644	.0078
66	1621	.0019	1644	.0078
67	1624	.0020	1645	.0080
68	1630	.0021	1648	.0082
69	1634	.0022	1649	.0083

data were used in conjunction with the Langmuir theory discussed in Section II to calculate the net vaporization force as a function of time. A sample calculation is presented in Table 12 for both Ni and Ni-12% Sn for the first second after eb cutoff. It is seen that between 3.5 and 4.25 seconds the vaporization force is of the same order of magnitude as the eb momentum force. During the first half second the calculations yield a large vaporization force (comparable to surface tension forces) and represent an intolerable situation as far as the free-float time is concerned. However, due to the large temperature gradients existing, the resulting surface tension driven convection will tend to reduce these values.

The Skylab orbit effects are included in the analysis by the method of Parker and Gatewood [9]. The computer program presented in Reference 9 was used as a subroutine in the present analysis to couple the effects of M512 position and orbit to the physical phenomena occurring in the vacuum chamber.

E. CONCLUSIONS BASED ON TRAJECTORY COMPUTATIONS

It has been shown that free-float times from 32 to 48 seconds (depending on the material) are required for complete containerless solidification to occur. The magnitude of each of the physical forces was discussed and general comments made concerning the effect of each on free-float time in the previous section. This subsection summarizes some of these conclusions.

- Electron beam force for a 460-g spring load has a duration of approximately 100 milliseconds and gives rise to a float time of 40 seconds.

- Kinetic energy of sphere due to spring effects (deployment technique) gives rise to float times of greater than 50 seconds.

- Vaporization force produces float times that are probably the critical link in process. Best estimates of the corresponding float time between 1/4 second after eb cutoff and occurrence of an isothermal outer layer range from 5 to 20 seconds. For some cases the time could even be considerably less than 5 seconds.

- Skylab orbit effects give rise to 29 to 46 seconds of float time.

Table 12

SUMMARY OF VAPORIZATION FORCE CALCULATION

Nickel						
Vaporization Force (dynes)	Time (sec)					
	3.00	3.25	3.50	3.75	4.00	4.25
f_x	882	55	8	1.5	0.3	.07
f_y	1480	126	25	5.8	1.3	.3
f_z	292	25	5	1.0	0.25	.06
Nickel-12% Tin						
f_x	1400	102	9	1	0.16	.02
f_y	2470	240	41	6	1.0	.16
f_z	485	47	8	1	0.2	.03

- Superposition of all of these forces produces an additive (as opposed to canceling) effect in most cases. Trajectory calculations show that even with conservative vaporization forces float times of less than 15 seconds will occur.

Lockheed documented in December 1972 [10] an early projection of anticipated float times less than the required containerless solidification times and again in April via the Science & Engineering Information Technical Note [11], presented as Appendix A for reference. In the latter report a conservative estimate of less than 20 seconds was forecast.

Another potential problem area, discussed in the 27 March 1973 presentation at MSFC, is that even with the relatively large forces on the sphere during the critical time of deployment, the possibility of "sticking" exists. Films of the KC-135 flight test showed that an adherence to the ceramic occurs on occasion that finally results in deployment due to acceleration transients in the ballistics trajectory of the aircraft. A typical sequence is shown in Figure 46. The events are referenced to the time corresponding to what appeared to be the fully molten condition, t=0. For the ensuing 0.300-second, that adherence to the ceramic occurred with periodic motion due to the acceleration transients is evident in the film sequence. At 0.310-second, deployment occurred with the trajectory shown in Figure 46. The important point remains, however, that without the acceleration transients (relatively large compared to the Skylab gravitational environment) specimen retention could have occurred. This adhesion is probably due to contamination of the ceramic from previous melts. The conclusion is that the possibility of unintentional retained specimen may occur in the actual Skylab mission.

F. LIQUID DYNAMICS

This subsection presents a summary of calculations made for Ni and Ni-12% Sn based on the thoughts outlined in Section II. First, the formation times are shown in Table 13 where it is seen that the transformation to minimum energy occurs very rapidly. However, due to inertial considerations, the spherical free surface is "overshot" and oscillations are set up which continue until dissipated by viscous damping. Table 15 gives the oscillation frequencies while Table 14 shows the time required for viscous effects to dampen an initial perturbation to 0.01% and 1% of its initial value.

Table 13

FORMATION TIMES FOR M553 MATERIALS

M553 Materials	ρ (g/cm^3)	σ (dyne/cm)	R (cm)	T (sec)
Ni	7.85	2050	.3175	.011
Ni-12% Sn	7.80	1500	.3175	.013

Table 14

FREQUENCY FOR M553 MATERIALS

Material	Frequency (Hz)
Ni	41
Ni-12% SN	35

Table 15

DECAY TIME FOR M553 MATERIALS

Material	μ (g/cm-sec)	ρ (g/cm^3)	R (cm)	Time (constant)	Time (.01%)	Time (1%)
Ni	.05	7.85	.3175	3.14	28.8	14.5
Ni-12% Sn	.043	7.80	.3175	3.62	33.0	16.7

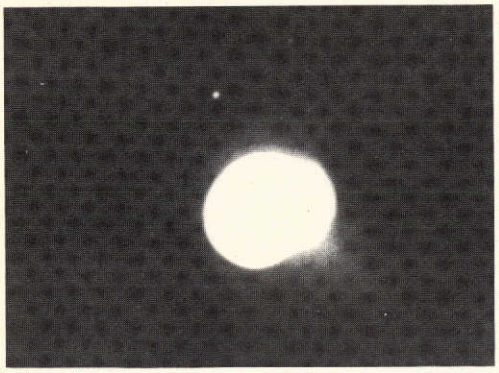

t = 0 (sec)

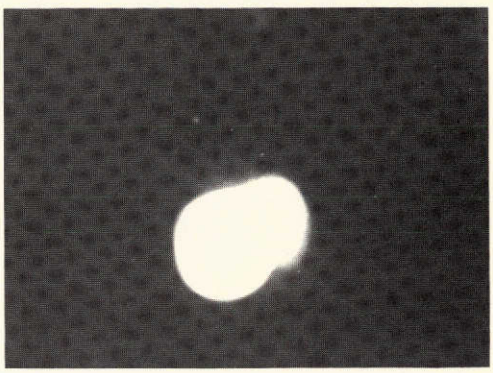

t = .250 (sec)

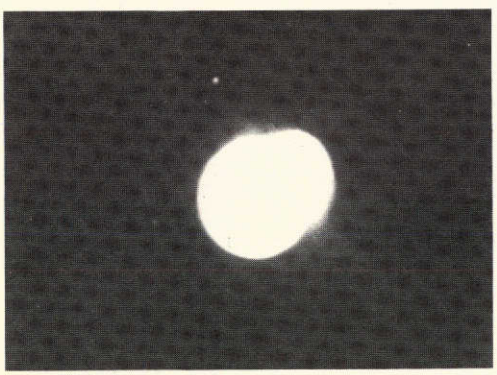

t = .275 (sec)

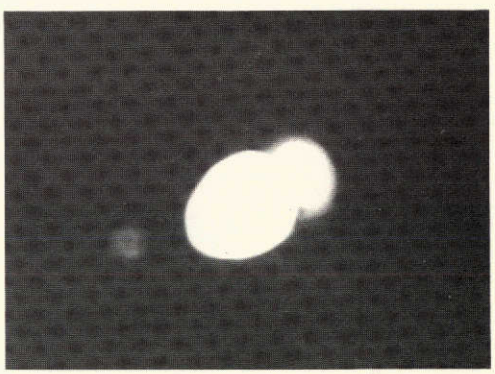

t = .290 (sec)

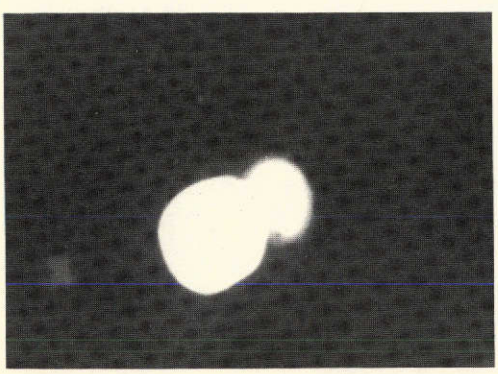

t = .295 (sec)

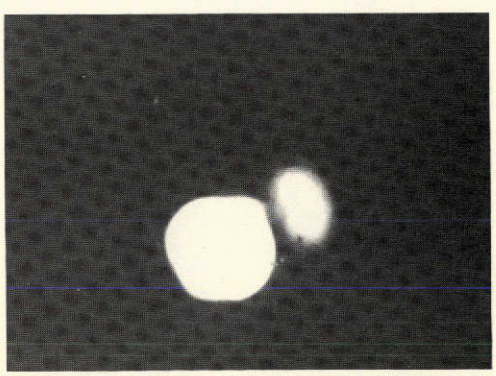

t = .310 (sec)

FIGURE 46. TRAJECTORY SEQUENCE – MARCH 1972 KC-135 FLIGHT (NICKEL) (CONTINUED)

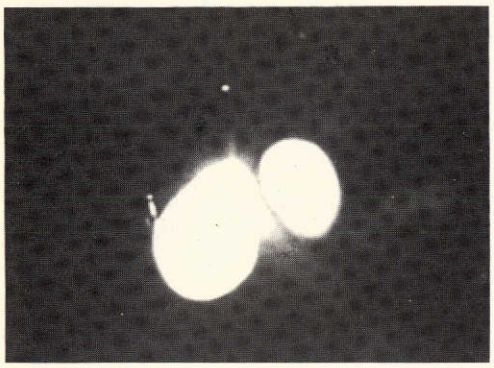

t = .325 (sec)

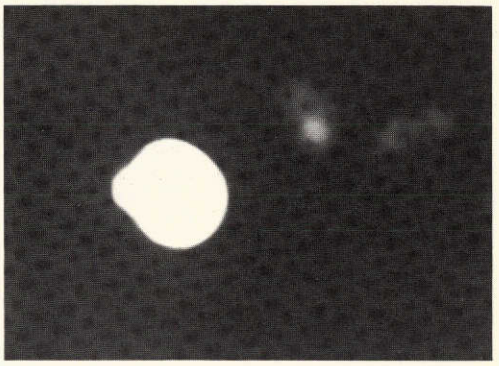

t = .360 (sec)

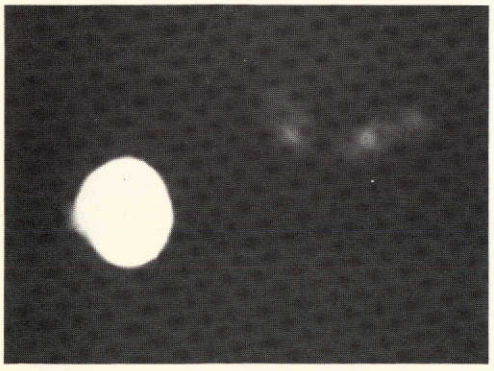

t = .395 (sec)

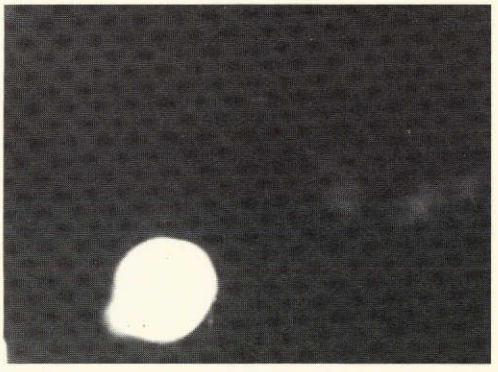

t = .400 (sec)

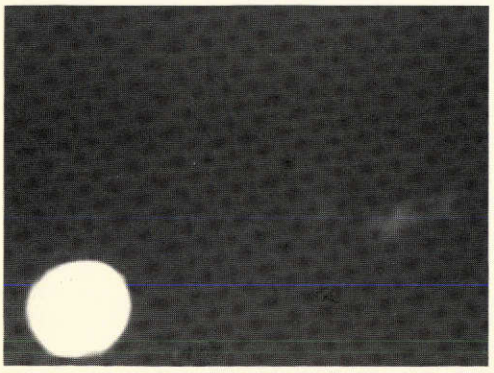

t = .450 (sec)

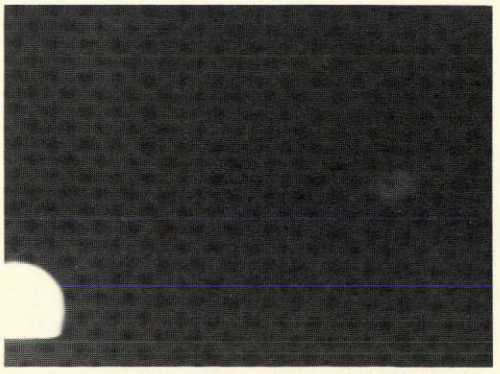

t = .515 (sec)

FIGURE 46. TRAJECTORY SEQUENCE (CONCLUDED)

G. SOLIDIFICATION PATTERNS

The theoretical preferential solidification pattern can be determined by determining the order that the individual nodes reach the solidification temperature on the cooldown cycle. For deployed specimens it has been shown that isothermal layers develop within one second after eb cutoff and as shown in Figure 31. Solidification occurs from this outer layer inward as expected. The time that solidification begins on the surface is seen to be 10.5 seconds compared to 10.7 seconds for the center of the sphere as there are only a few degrees difference between the outer and inner portion from 4 to 10 seconds after eb cutoff. However, the retained specimen exhibits an entirely different phenomenon. The initial solidification point is the sting as expected. The pattern develops (namely, solidifying from the outside in) as areas 1-2-8, 3-4-8 and 5-6-8 begin to solidify. As areas 7 and 8 reach the solidification temperature, area 9 is still superheated; area 11 is, however, molten at this point and no shrinkage should occur. The same is true of area 10-11-8, but as area 12-13-8 approaches the solidification temperature at area 13, shrinkage could occur as this is the last region to begin the solidification process – thus a possible void. This occurs as a result of the relatively large vaporization losses in the vicinity of the eb impingement, giving rise to large cooling rates.

These calculations were made with the eb impingement location corresponding to actual operating procedures. This corresponds to only one-half of the beam impinging on the surface in the region of area 10-12 in Figure 47. Additional calculations were made with full eb impingement in the center of the specimen 7-5. It was found that, depending on the power (or beam duration after sting release), the region opposite the heat addition point (lower left of specimen in Figure 47) would not melt before deployment. Then depending on the amount of superheat the remaining solid could melt in the free-float condition. Alternately, if eb impingement was lower than the center and sting release occurred early in the melt cycle, a large unmelted portion would remain in the final product. As stated previously if eb impingement is near the "one-o'clock" position, a fully molten specimen will result.

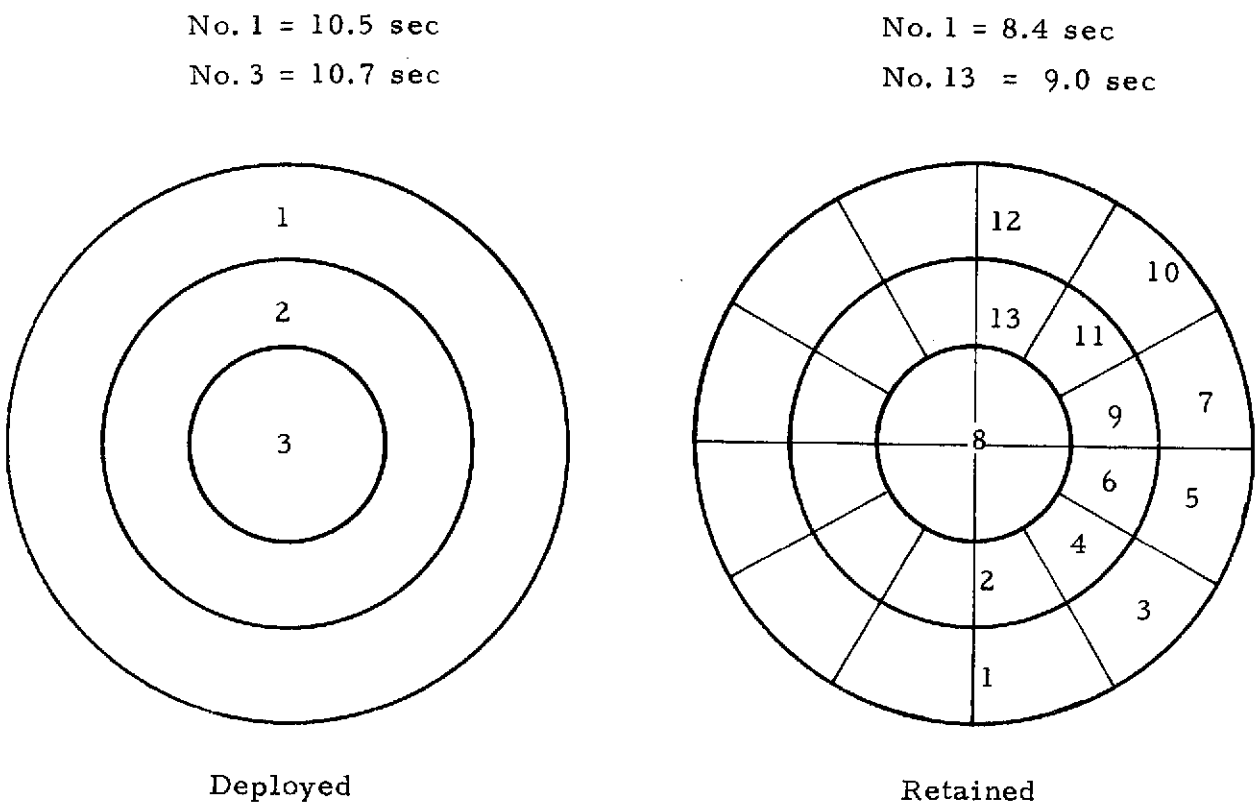

FIGURE 47. SPHERE SOLIDIFICATION SEQUENCE (PURE NICKEL)

SECTION V. CONCLUSIONS AND RECOMMENDATIONS

Analyses of both flight and ground-based tests of the M551 metals melting experiment indicated no definite trends in the effects of gravity on the test results. The beading phenomenon which appears in the stainless steel and tantalum specimens is shown to exhibit a remarkable similarity to vortex shedding. The bead spacing distance predicted from vortex shedding theory was found to be in almost exact agreement with test results for the stainless steel specimens and within about a half order of magnitude for the tantalum specimens.

In the M553 sphere forming experiment, the predicted temperature histories compared very closely to ground-based test results. This experiment proved to be more difficult to achieve satisfactory results than the M551 experiment. Some of the sphere specimens did not deploy from the sting, and the intense localized heating and pressure from the electron beam induced non-uniform temperature distributions and surface oscillations. Also, the deployment mechanism and the pressure forces induced by the electron beam resulted in sizeable drift velocities. It is suggested that future improvements in experiment design for this type of study might include induction heating to provide a more uniform temperature distribution and to eliminate surface deforming pressures, and magnetic confinement to eliminate drifting of the specimen into the chamber wall.

REFERENCES

1. Gibbs, J. W.: The Collected Works of J. Willard Gibbs, Vol. I, Thermodynamics, Yale University Press, New Haven, Conn., 1928, p. 314.

2. Shuttleworth, R.: Proc. Phys. Soc., London, Vol. A63, 1950, p. 444.

3. Pethica, B. A., and Pethica, T. J. P.: The Constant Angle Equilibrium, 2nd International Congress of Surface Activity, Vol. III, Academic Press, New York, N. Y., 1957, p. 131.

4. Bikerman, J. J.: Solid Surfaces, 2nd International Congress of Surface Activity, Vol. III, Academic Press, New York, N. Y., 1957, p. 125.

5. Johnson, R. E., Jr.: Conflicts Between Gibbsian Thermodynamics and Recent Treatments of Interfacial Energies in Solid-Liquid-Vapor Systems, J. Phys. Chem., Vol. 63, 1959, p. 1655.

6. Li, T.: Hydrostatics in Various Gravitational Fields, J. Chem. Phys., Vol. 36, No. 9, 1962, p. 2369.

7. Tong, H., and Giedt, W. H.: Interpretation of the Observed Oscillation of an Electron Beam Welding Cavity, in Electron and Ion Beam Science and Technology, Fourth International Conference (Robert Bakish, ed.), The Electrochemical Society, N. Y., 1970.

8. Johnson, P. C., Peters, C. T. and Wechsler, A. E.: M553 Sphere Forming Experiment, Phase B Report, Contract NAS8-28723, Arthur D. Little, Inc., Cambridge, Mass., July 1973.

9. Parker, J. W., and Gatewood, E.: Sphere Float Time and Path for Skylab M553 Sphere Floating Experiment, NASA TM X (Preliminary).

10. Brashears, M. R.: Materials Processing in Space (M512), Monthly Progress Report, LMSC-HREC PR D306360, Lockheed Missiles & Space Company, Huntsville, Ala., December 1972.

11. Brashears, M. R.: Science and Engineering Information for M551 and M553 Experiments, LMSC-HREC TN D306615, Lockheed Missiles & Space Company, Inc., Huntsville, Ala., April 1973.

Appendix A

SCIENCE AND ENGINEERING INFORMATION FOR M551 AND M553 EXPERIMENTS

TECHNICAL NOTE

LOCKHEED
Huntsville Research & Engineering Center

Contract NAS8-28729 Date 30 April 1973 Doc. LMSC-HREC TN D306615

Title: SCIENCE AND ENGINEERING INFORMATION FOR M551 AND M553 EXPERIMENTS

FOREWORD

This technical note was prepared by the Fluid Mechanic Applications Group, Aero-Mechanics Section of the Lockheed-Huntsville Research & Engineering Center for the Process Engineering Laboratory of Marshall Space Flight Center under Contract NAS8-28729. This task was prepared at the request of Mr. Paul H. Schuerer, S&E-PE-MX.

INTRODUCTION

The information contained herein is for the purpose of updating the documentation for Skylab experiments M551 and M553. To incorporate the latest observations and opinions of contractors supporting development of the experiments and evaluation of resulting specimens and data, the following questions are asked:

1. What do you consider to be the most significant results of your studies to date?
2. What are your projections for variations-in-sample properties, composition, structure and experiment data attributable to "zero gravity effects"?
3. What specific properties or effects will you be concentrating your efforts on in evaluating the flight samples and data?
4. How can the proposed variations noted in (2) above be used to structure additional experiments, improve commercial materials and processes and develop new materials? List specific examples.
5. What particular statements should be included in the experiment objectives as a result of your specific studies and projections of zero-g effects?

Each question is answered for both the M551 metals melting and the M553 sphere forming experiments.

DISCUSSION

Question 1

General: Lockheed-Huntsville is responsible for all process phenomena with particular attention given to adhesion-cohesion studies with emphasis on the fluid dynamics of the molten metal. The effects of cohesion of the molten metals and their capability of relating their shapes have been interrelated with the adhesive influence of the molten metals in contact with ceramics and metals in a low-gravity environment.

Also the importance of fluid dynamic considerations has been established in that all expected variations in terrestrial versus space processing are created as a result of the dominance of capillary motion (instead of gravity-induced flow), minimal segregation (sedimentation) and a decrease in hydrostatic pressure gradient – all hydrodynamic phenomena. This conclusion can be restated that gravity has no direct effect on grain structure or any other property of the solidified material. The gravity effects all occur as a result of differing fluid motion.

- M551
  - Establishment of the role of vaporization in the cavity shape
  - Performance of three-dimensional temperature calculations for weld and dwell modes of melting for multi-component variable property material
  - Establishment of magnitude and direction of gravity during actual Skylab mission to allow meaningful conclusions to be drawn from micrographs about zero-gravity effects.
- M553
  - Identification of physical forces affecting the trajectory of the molten sphere
  - Development of unifying calculational technique to predict trajectory of molten spheres during free-float condition
  - Development of three-dimensional thermal model to predict temperature history of sphere during melting

- Establishment of the role of vaporization on temperature history and motion of sphere
- Establishment of the magnitude and qualitative motion of surface dynamics
- Performance of detailed analysis of KC-135 flight data and ground-based experimental tests.

Question 2

General: As discussed previously, the only expected differences in zero-g versus one-g processing are the dominance of capillary motion instead of gravity-induced flow, the absence of segregation and a decrease in hydrostatic pressure. There are, however, many indirect effects (advantages) due to a lack of gravity. In general, the factors affecting the final sample properties, composition and structure can be divided into three major categories, i.e.,

- Nucleation
- Growth
- Reaction kinetics.

The absense of gravity might allow better control of the independent variables affecting each category; this occurs directly through the three aforementioned fluid dynamic effects and indirectly through other mechanisms that are a function of fluid motion (gas content, composition, foreign particles, imperfections, cooling rate, nucleation rate, etc.)

- M553
  - Less heterogeneous nucleation will occur due to foreign particles as segregation effects will be minimal.
  - If the material has any gas content that comes out of solution during solidification, an increase in porosity may result as there will be minimal tendency for the gas pockets to surface (except for convection effects).

- For the materials with high vaporization rates (Ni-12% Sn, and Ni-30% Cu), a substantial increase in surface cooling occurs — thus greater nucleation and surface tension gradients.

- Even though the cooling rate is dependent on the amount of convection, the cooling rate will be determined by radiation considerations only as the sphere reaches isothermal superheat conditions in approximately a second. This in turn dictates the solidification rate.

- Since solid formations in polycrystalline materials is highly dependent on the distribution of foreign particles and the liquid motion, the associated differences should be discernable (homogeneous nucleation).

- M551

  - Since all fluid mechanic phenomena require a finite time to occur (due to inertia considerations) an effect due to gravity during the weld portion of the experiment may not occur (except for a more spherical bead when beading occurs) as large cooling rates are available via conduction.

  - A more homogeneous dwell structure will occur due to lack of sedimentation.

  - The liquid cavity shape will be determined by vaporization effects and should be nearly symmetric (different temperature gradients do exist in positive and negative radial directions).

  - If degassing is the cause for the splattering as noted in color films of the process, porosity may result in the zero-gravity dwell as the driving force for the pockets to surface is less.

Question 3

- M551 and M553

  - The flight films will be analyzed in detail and compared with KC-135 and ground-based results.

  - Observations from other contractors will be analyzed and compared with expected and predicted phenomena.

  - Correlation of actual gravity direction during Skylab experiments with experimental observations and results.

Question 4

- M553

To achieve the objectives of the current M553 experiment for all the selected materials, free-float times on the order of 60 seconds are required. Since it is highly unlikely that all of the physical forces will add in such a fashion to negate each other (as the system was not designed to do so), actual float times will be much less (probably less than 20 seconds). However, the concept of the sphere forming experiment is extremely exciting as the production of a nearly perfect homogeneously structured spherical specimen has important terrestrial applications.

  - Future experiment design should emphasize non-mechanical deployment, uniform heating and cooling and filming rates of at least 3000 pps.

- M551

  - The results of the weld portion of the experiment will establish the feasibility of "space repair."
  - Additional experiments with the same unit with high-speed color movies (3000 pps) with a different lens system should allow the fluid mechanics of welding to be analyzed in sufficient detail to answer many currently unresolved problems.

Question 5

- M553

  - Emphasis should be placed on fluid mechanic consideration as outlined previously.
  - Study of deployment dynamics as experiment success and final product are both dependent on this important phase of the experiment.
  - Role of temperature history on the final product.

- M551

  - Role of temperature history on the final product.

M. R. Brashears, Ph.D.
Fluid Mechanic Applications Group

Approved

B. Hobson Shirley, Supervisor
Aero-Mechanics Section

Appendix B

THERMAL HISTORY RESULTS FOR ALUMINUM AND TANTALUM DISKS

Appendix B

Temperature calculations were made for the aluminum and tantalum disks in the same manner as for the stainless steek disks described in Section 3. The disk configuration (thickness, etc.), for all disks was assumed to be identical. The resulting temperature plots are given in Figs. B-1 through B-20. The maximum calculated temperatures for all three disk materials are compared in Table B-1.

Table B-1

COMPARISON OF CALCULATED MAXIMUM TEMPERATURES FOR STAINLESS STEEL, ALUMINUM AND TANTALUM DISKS

Node No.	Maximum Temperatures, ^{o}C		
	Stainless Steel	Aluminum	Tantalum
317	322	697	879
315	236	669	880
223	330	198	126
221	332	201	126
219	37	220	117
135	725	1010	1061
133	725	1092	1060
131	41	218	152
35	818	1256	2056
33	819	1278	2060
31	58	219	157

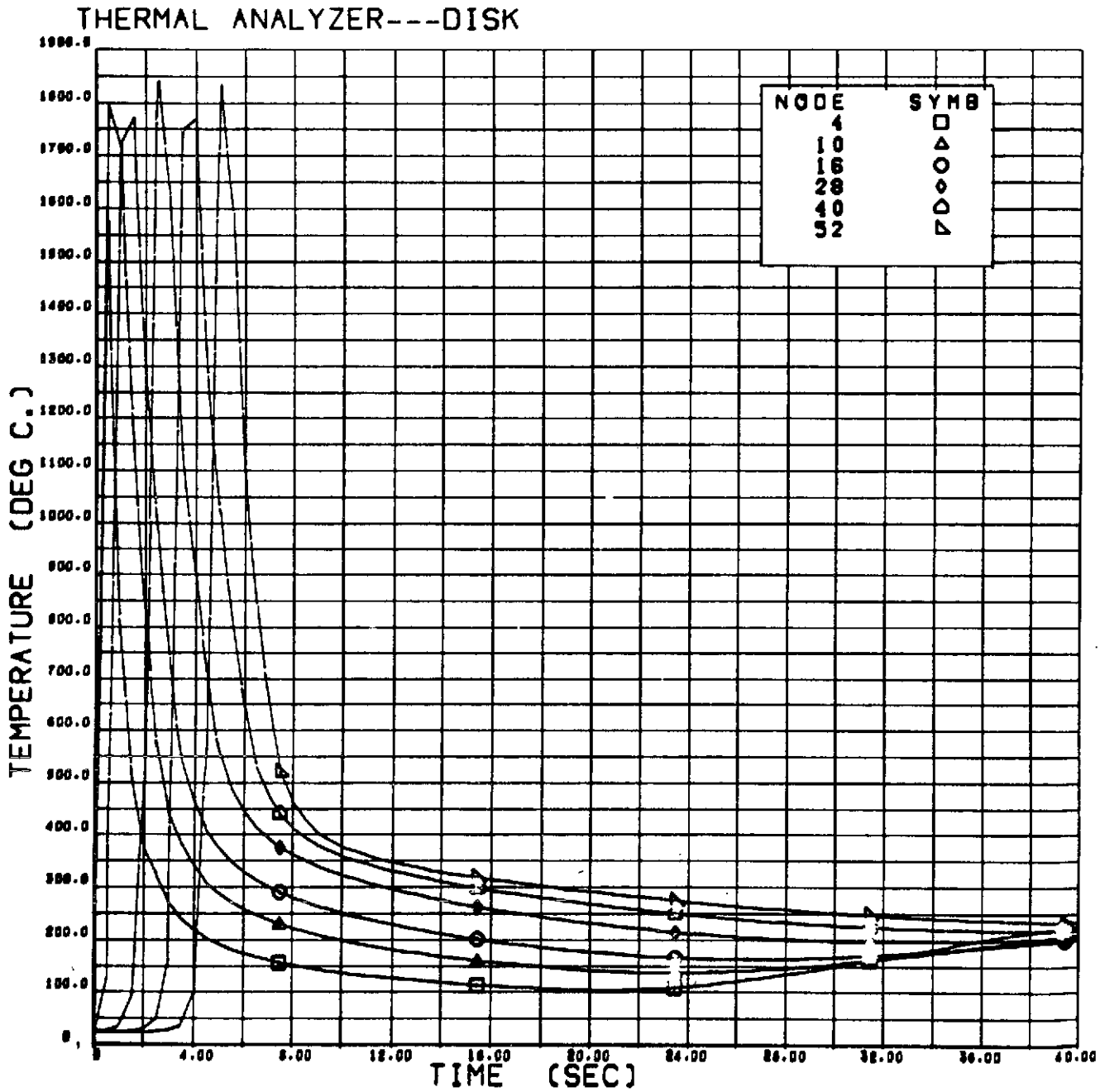

FIGURE B-1. THERMAL HISTORY FOR A 0.02-INCH ALUMINUM DISK (NODES 4, 10, 16, 28, 40 AND 52)

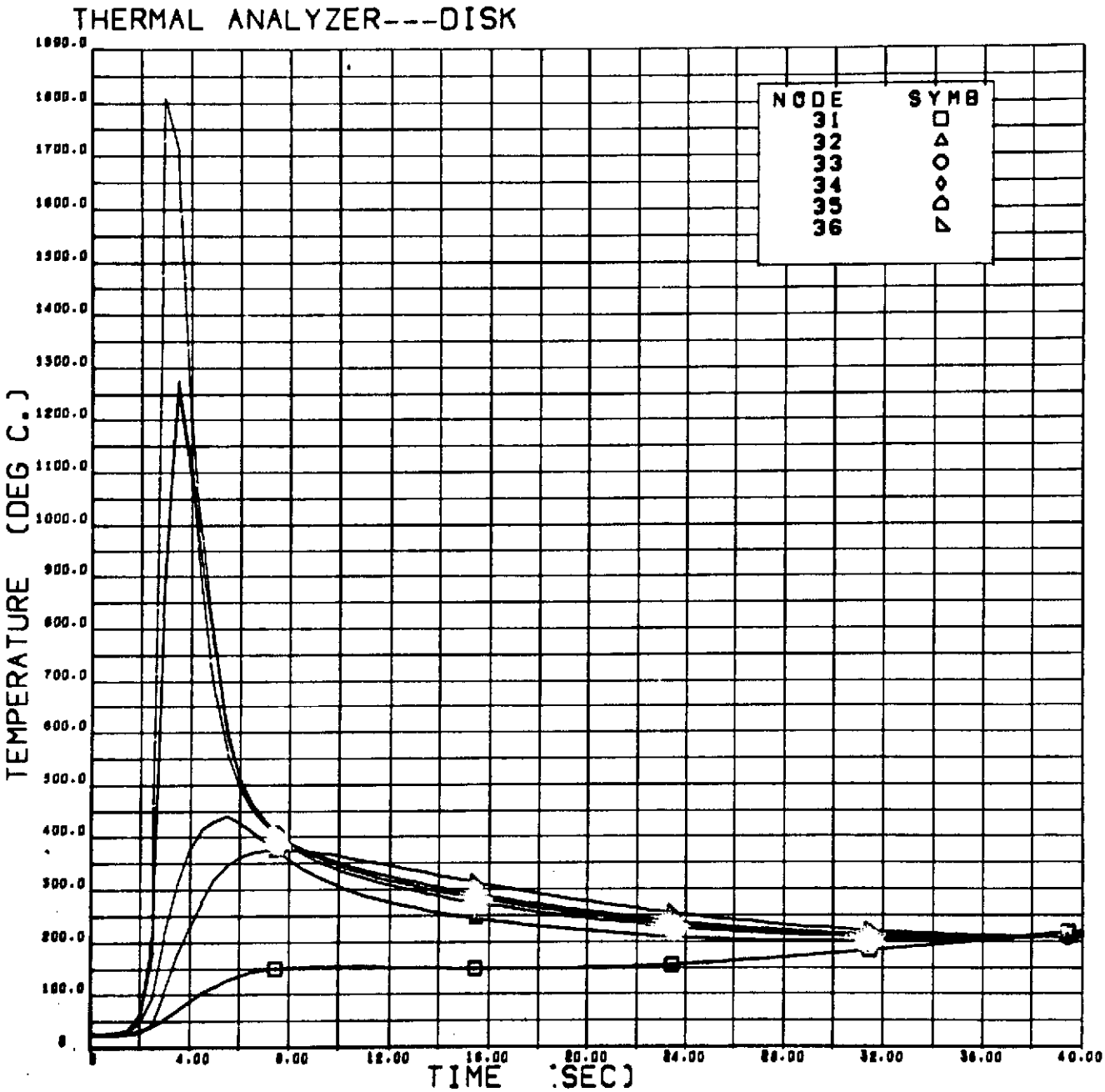

FIGURE B-2. THERMAL HISTORY FOR 0.02-INCH ALUMINUM DISK (NODES 31 THROUGH 36)

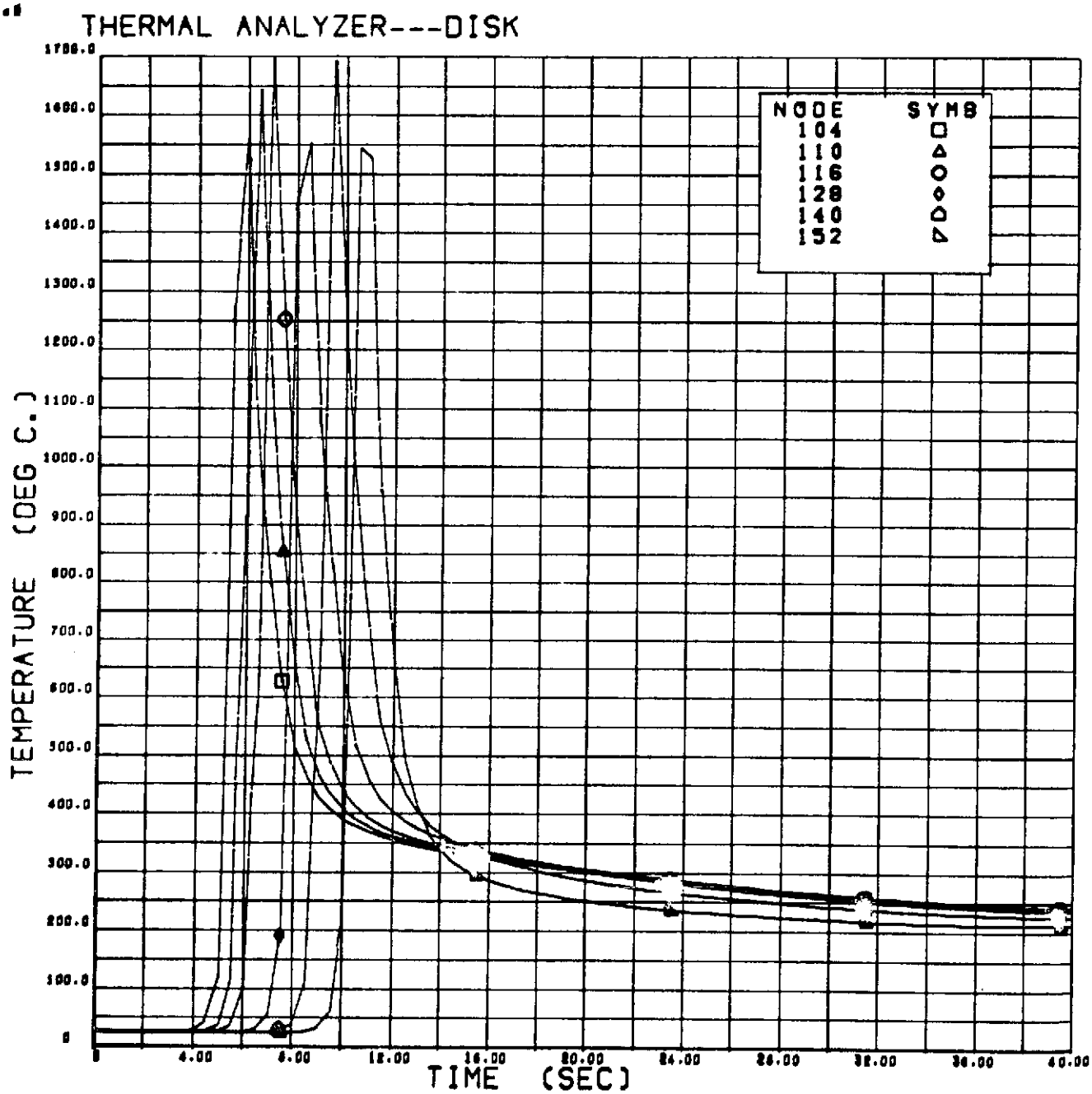

FIGURE B-3. THERMAL HISTORY FOR 0.05-INCH ALUMINUM DISK (NODES 104, 110, 116, 128, 140 AND 152)

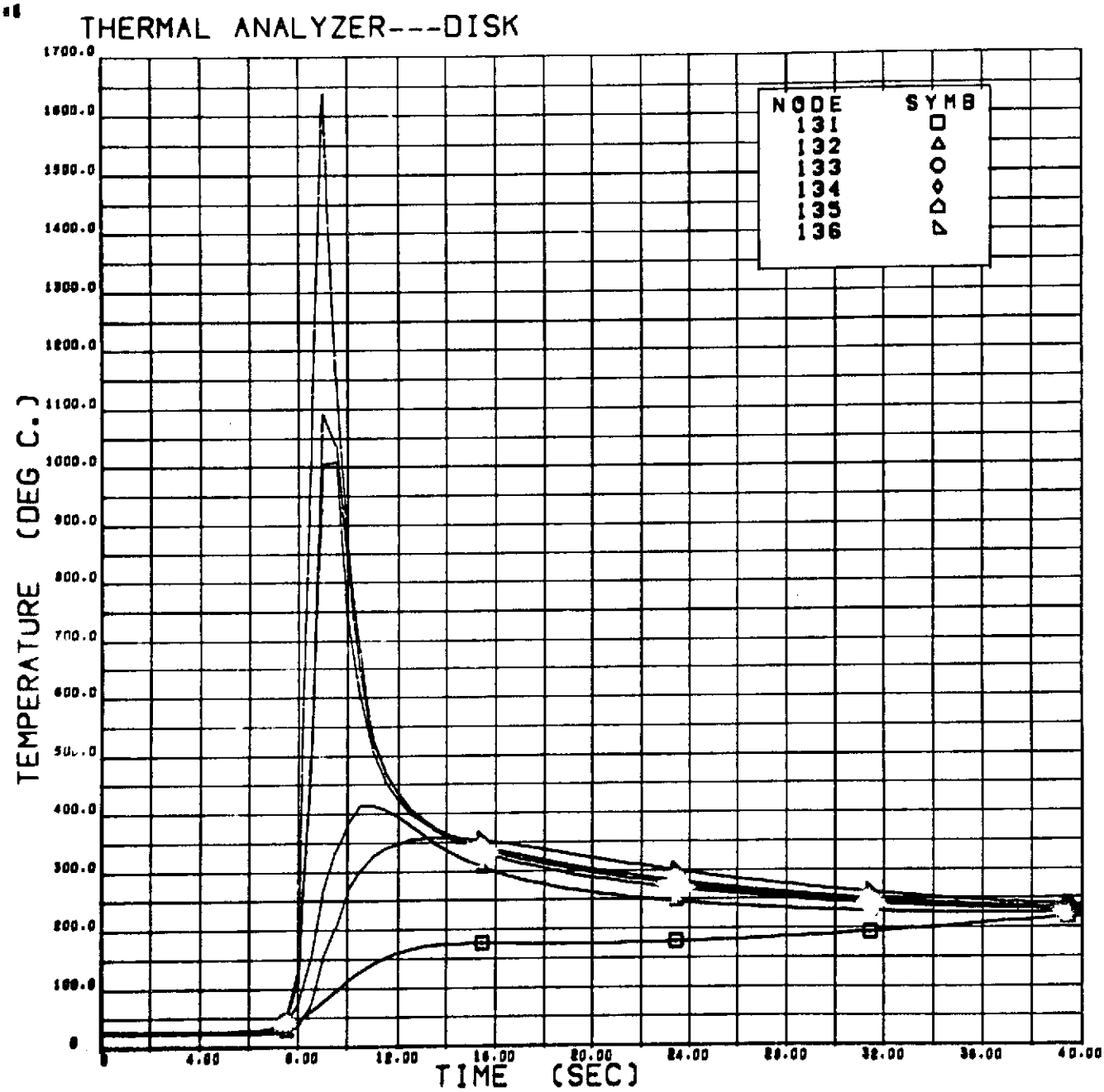

FIGURE B-4. THERMAL HISTORY FOR 0.05-INCH ALUMINUM DISK (NODES 131 THROUGH 136)

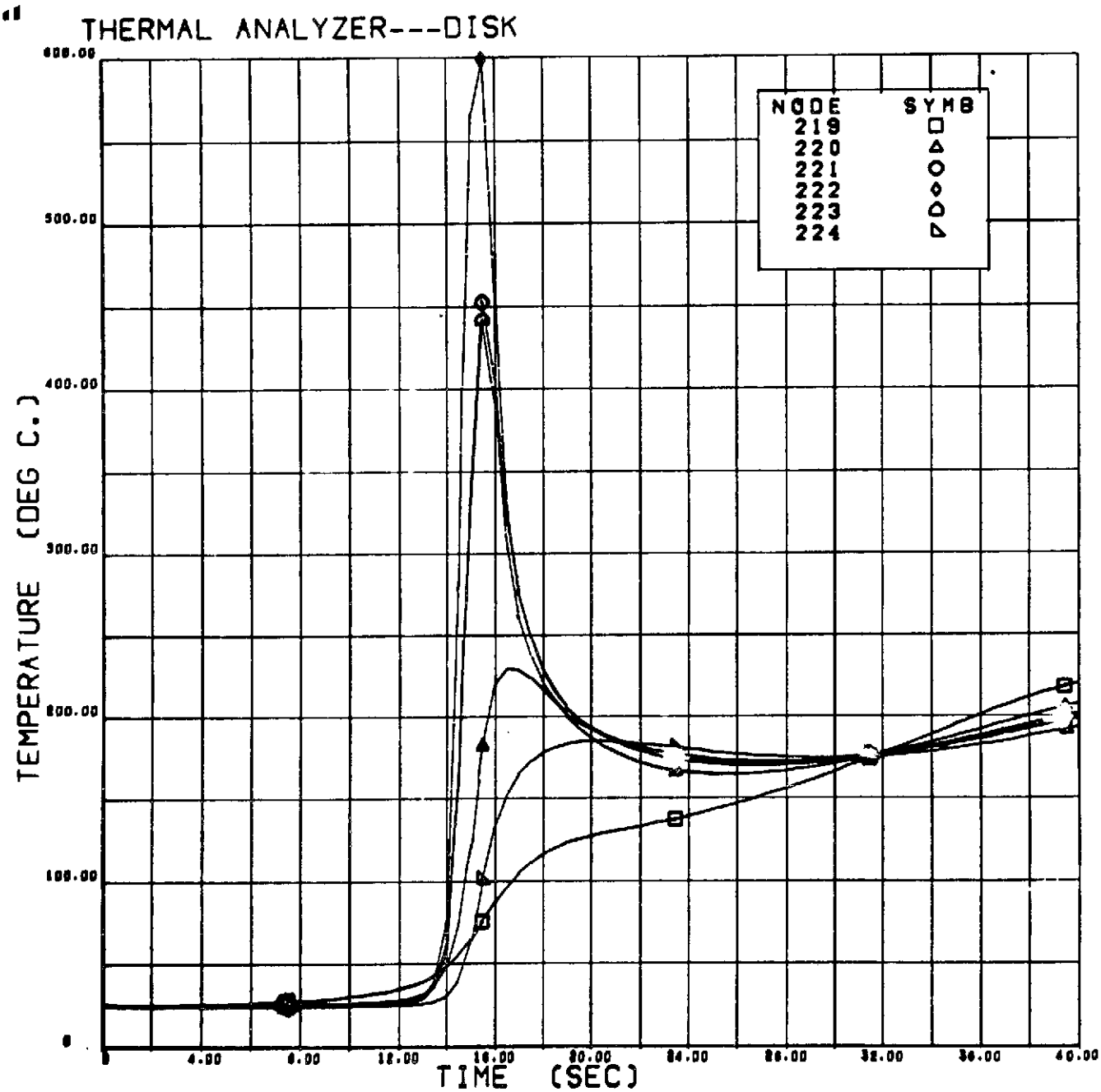

FIGURE B-5. THERMAL HISTORY FOR 0.125-INCH ALUMINUM DISK (NODES 219 THROUGH 224)

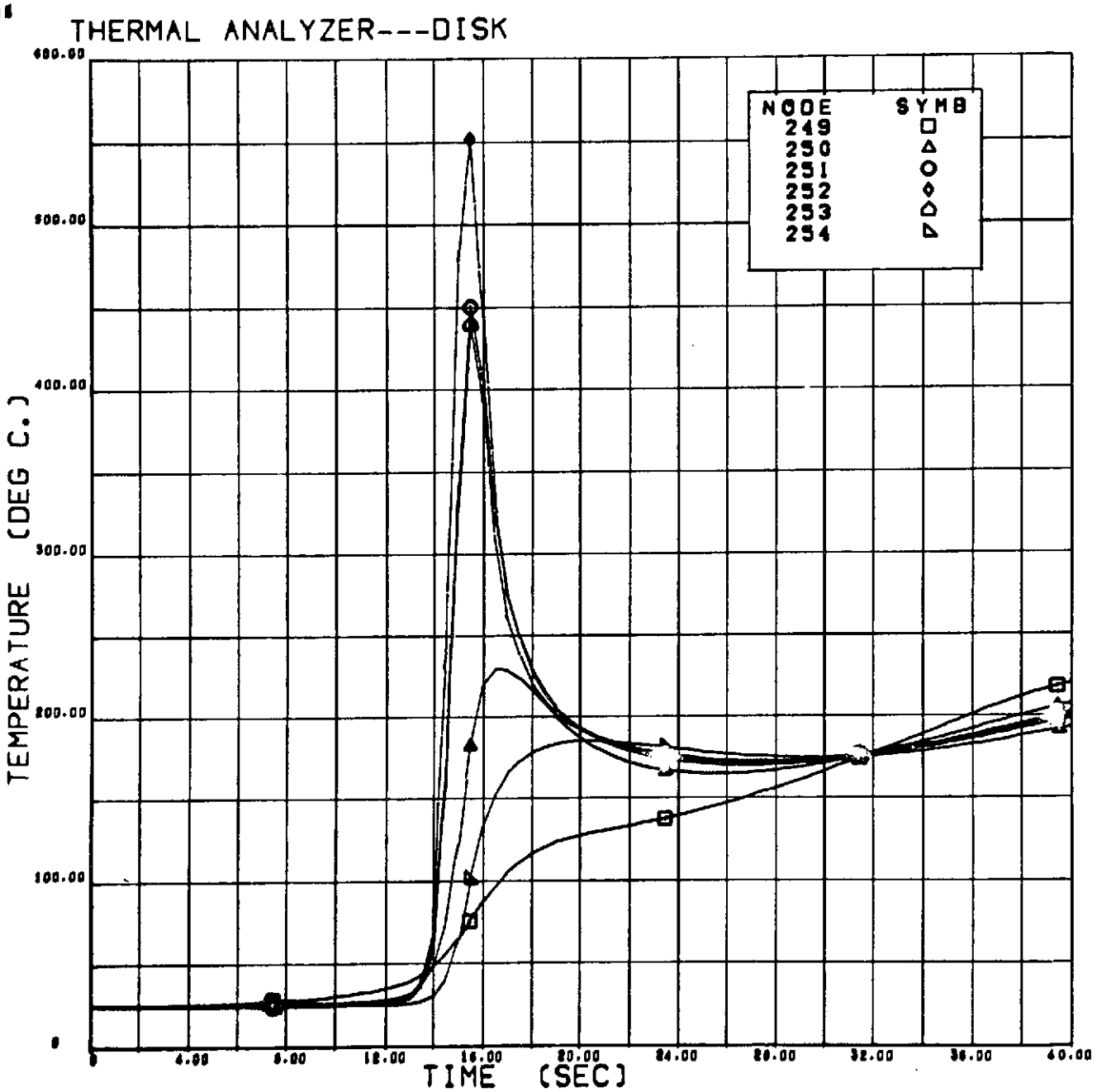

FIGURE B-6. THERMAL HISTORY FOR 0.125-INCH ALUMINUM DISK (NODES 249 THROUGH 254)

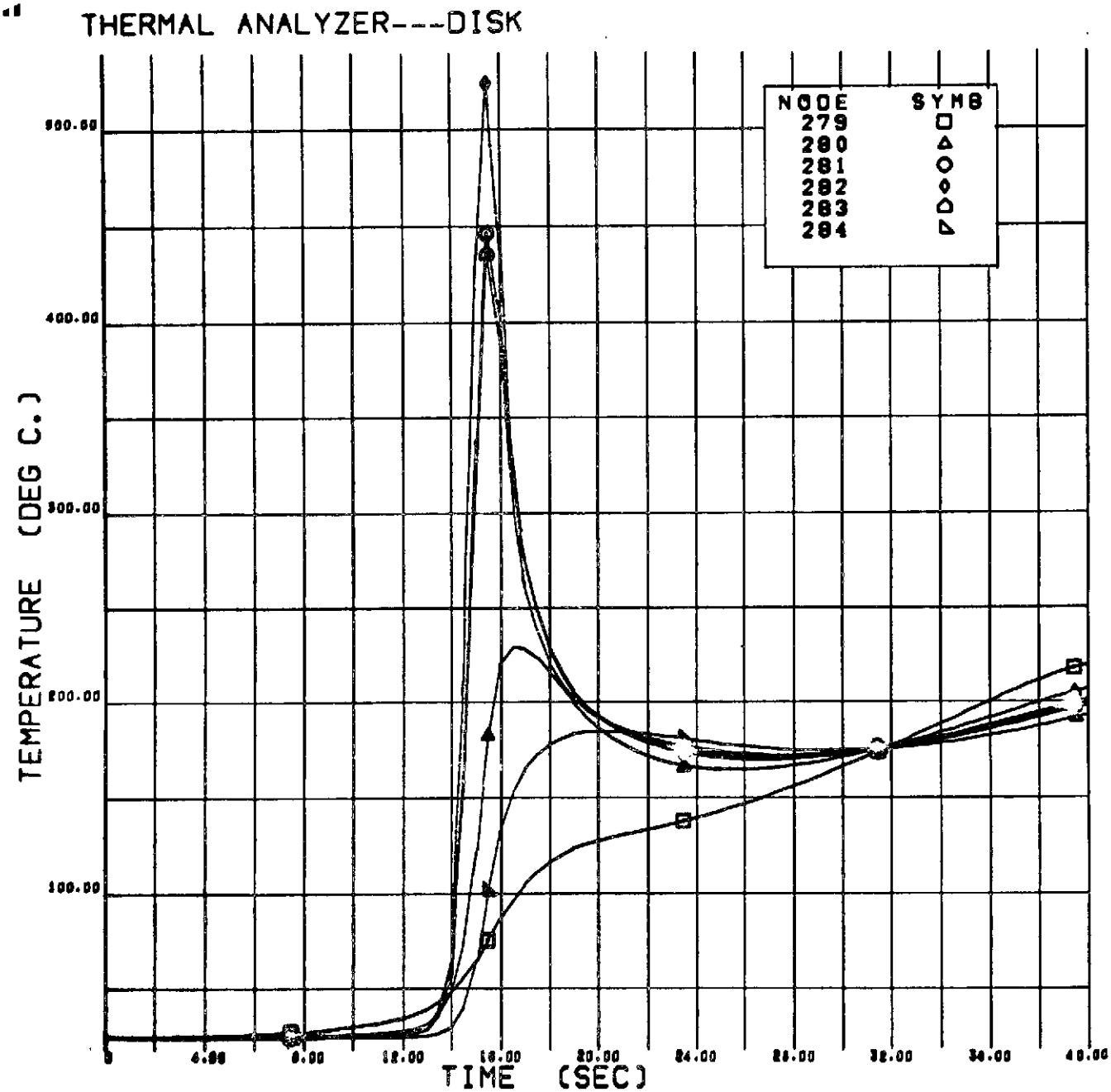

FIGURE B-7. THERMAL HISTORY FOR 0.125-INCH ALUMINUM DISK (NODES 279 THROUGH 284)

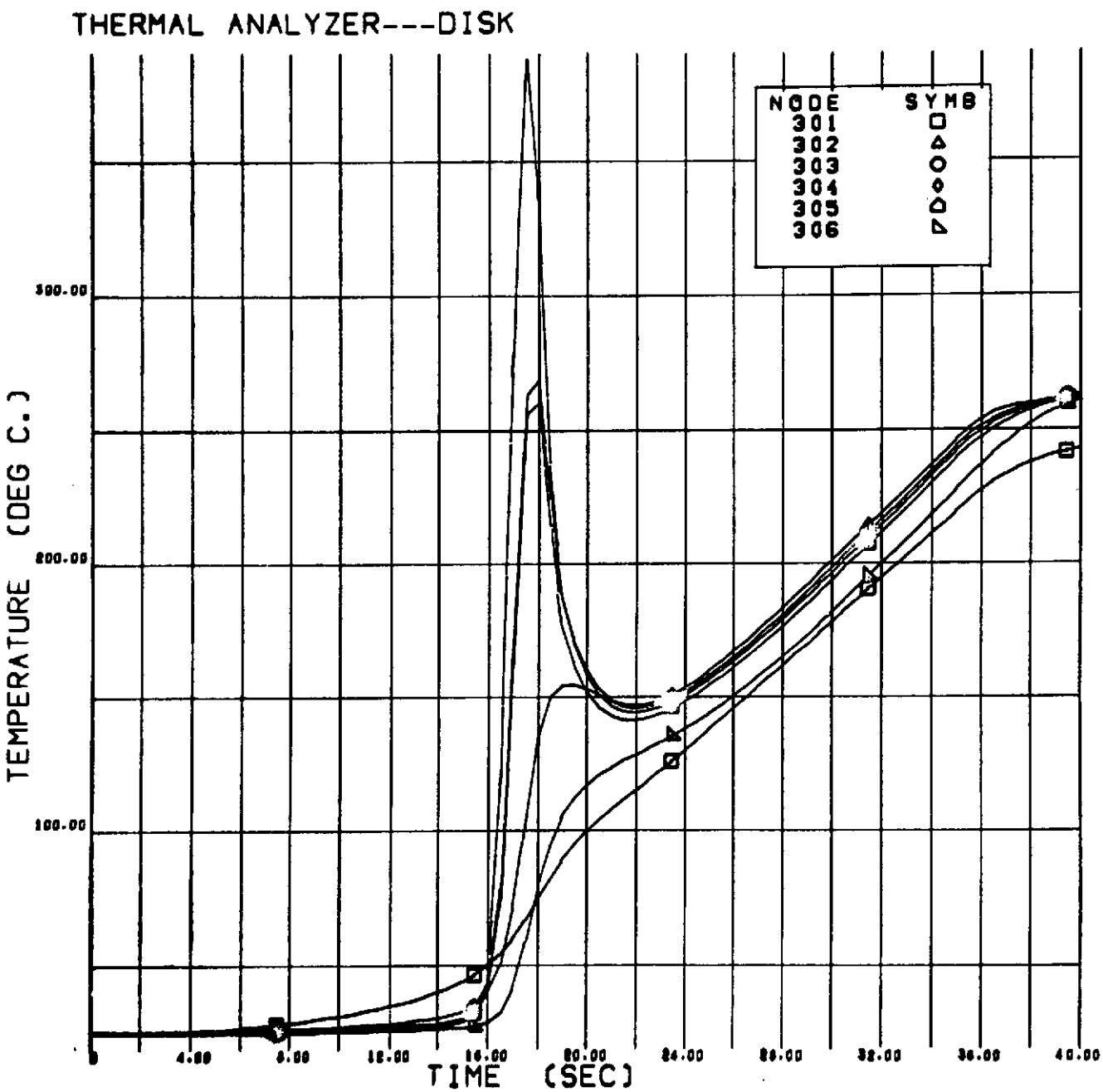

FIGURE B-8. THERMAL HISTORY FOR 0.125-INCH ALUMINUM DISK (NODES 301 THROUGH 306)

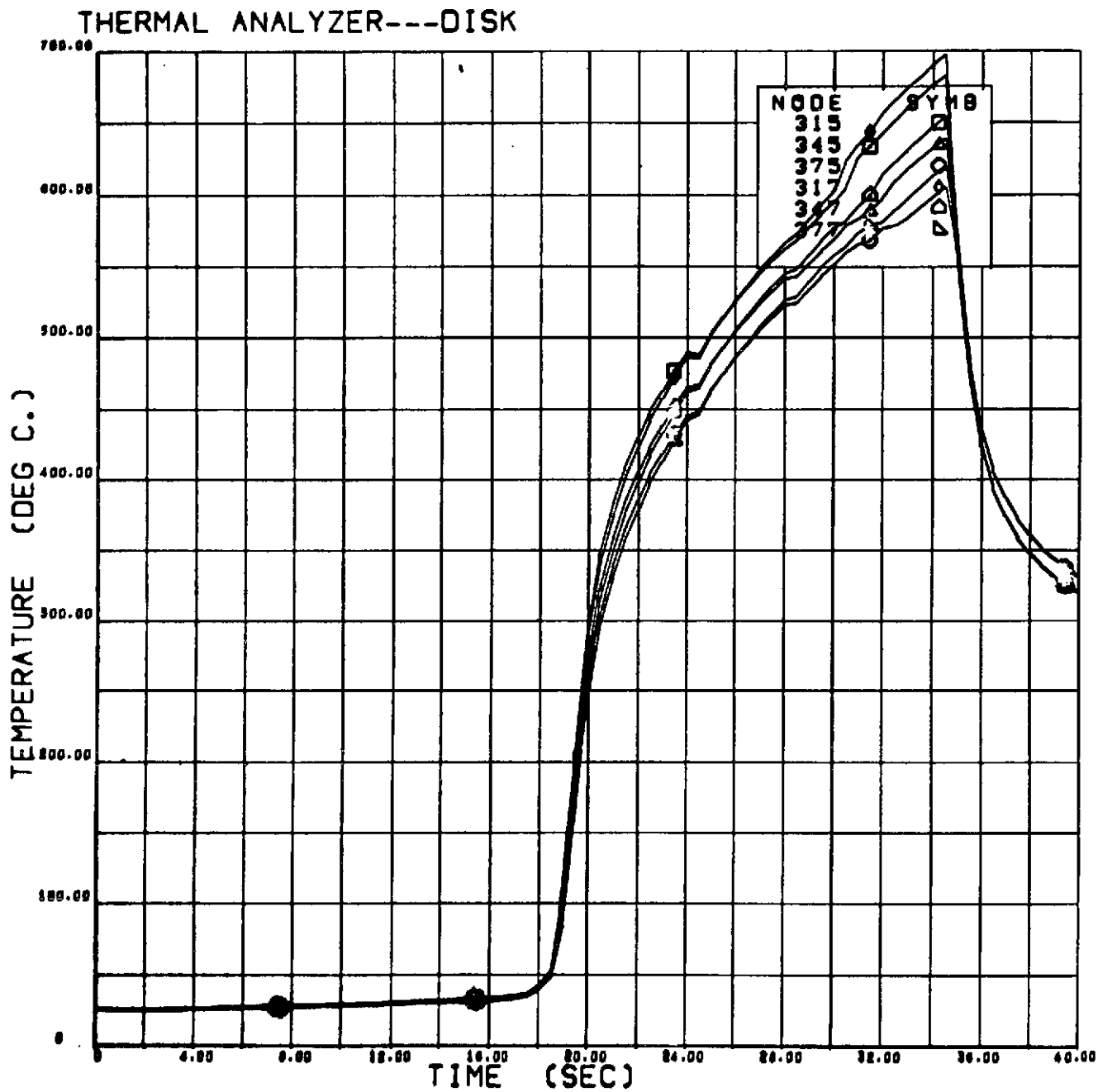

FIGURE B-9. THERMAL HISTORY FOR 0.250-INCH ALUMINUM DISK (NODES 315, 345, 375, 317, 347 AND 377)

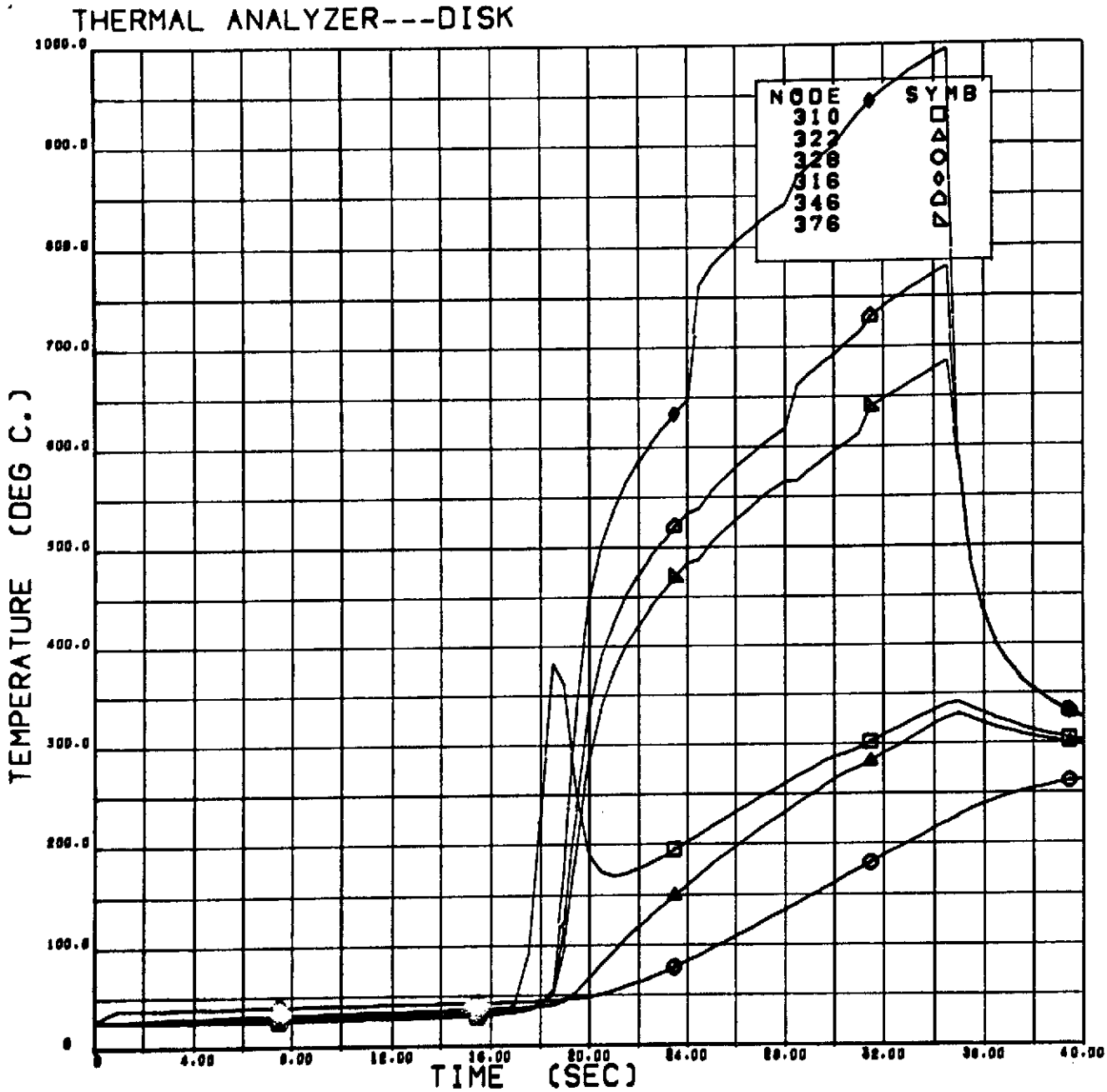

FIGURE B-10. THERMAL HISTORY FOR 0.250-INCH ALUMINUM DISK (NODES 310, 322, 328, 316, 346 AND 376)

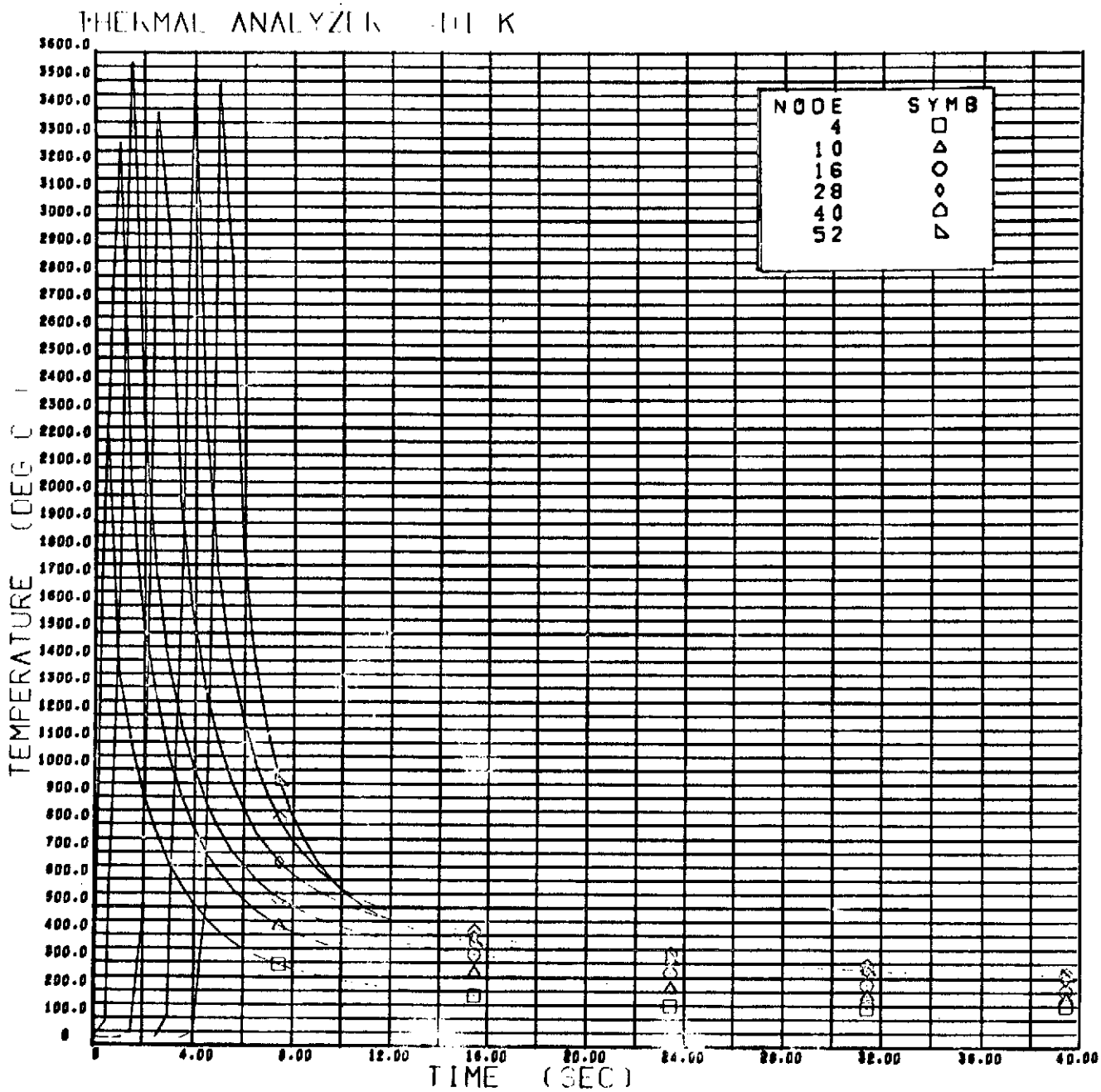

FIGURE B-11. THERMAL HISTORY FOR 0.02-INCH TANTALUM DISK (NODES 4, 10, 16, 28, 40 AND 52)

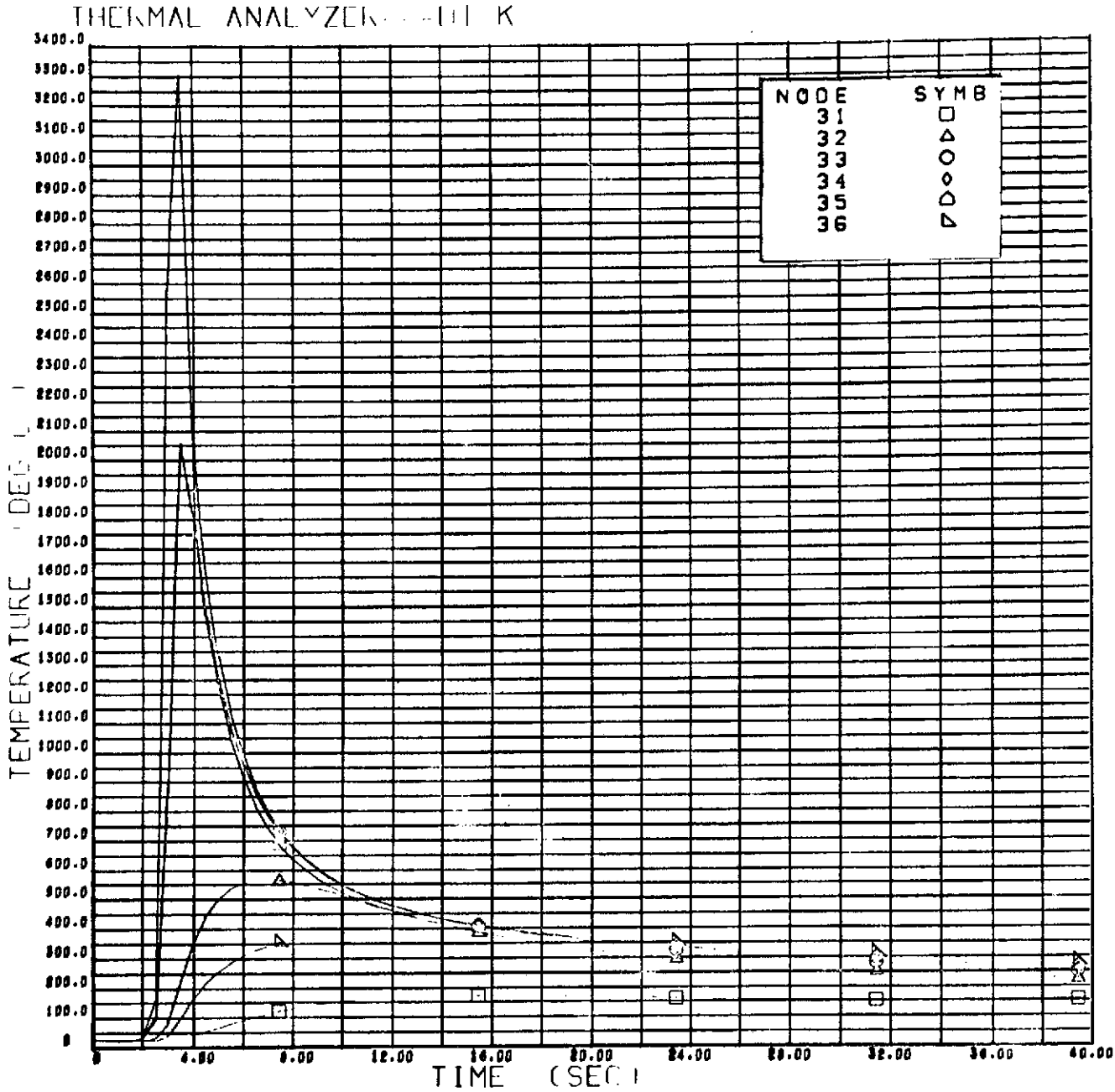

FIGURE B-12. THERMAL HISTORY FOR 0.02-INCH TANTALUM DISK (NODES 31 THROUGH 36)

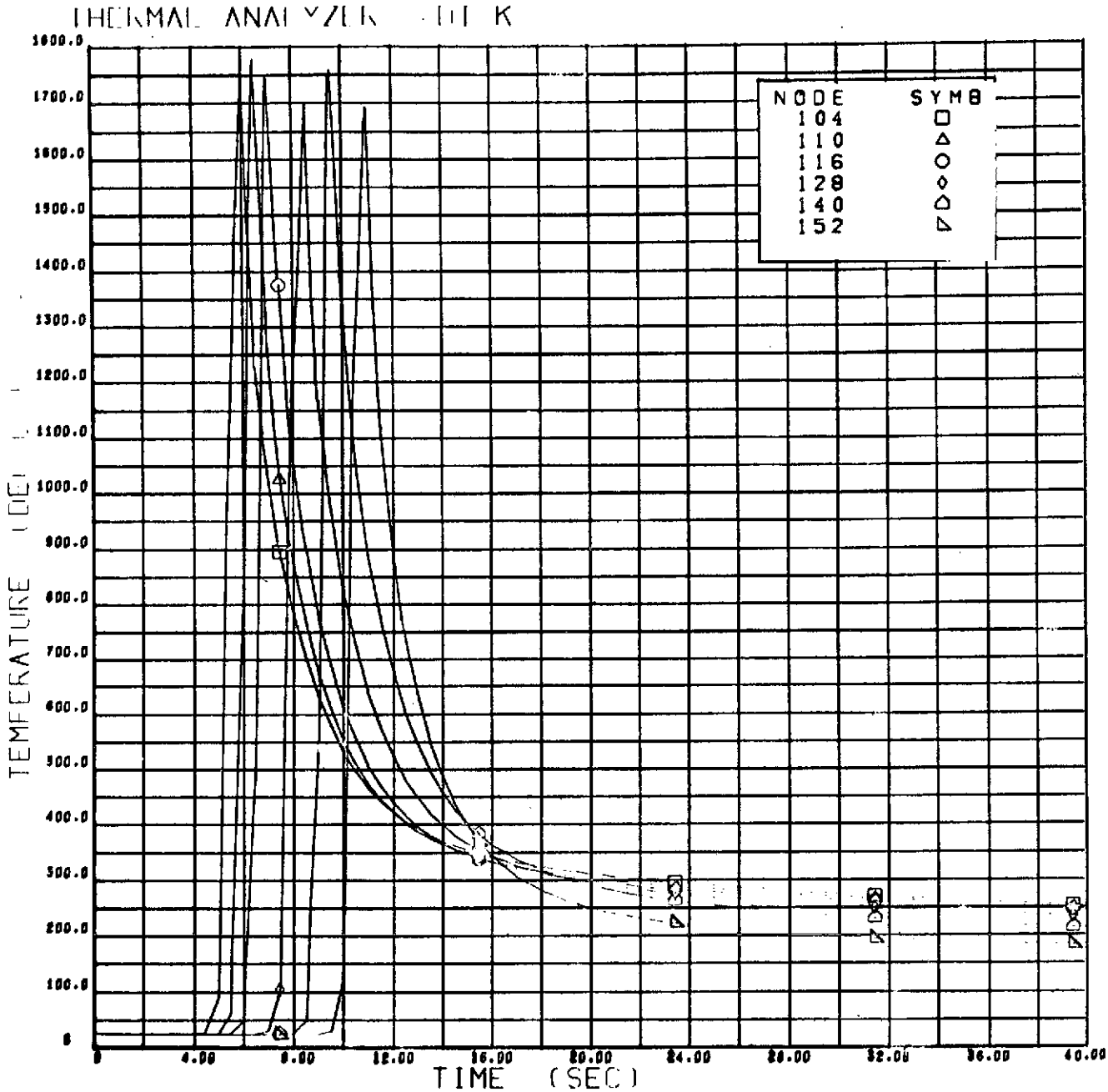

FIGURE B-13. THERMAL HISTORY FOR 0.05-INCH TANTALUM DISK (NODES 104, 110, 116, 128, 140 AND 152)

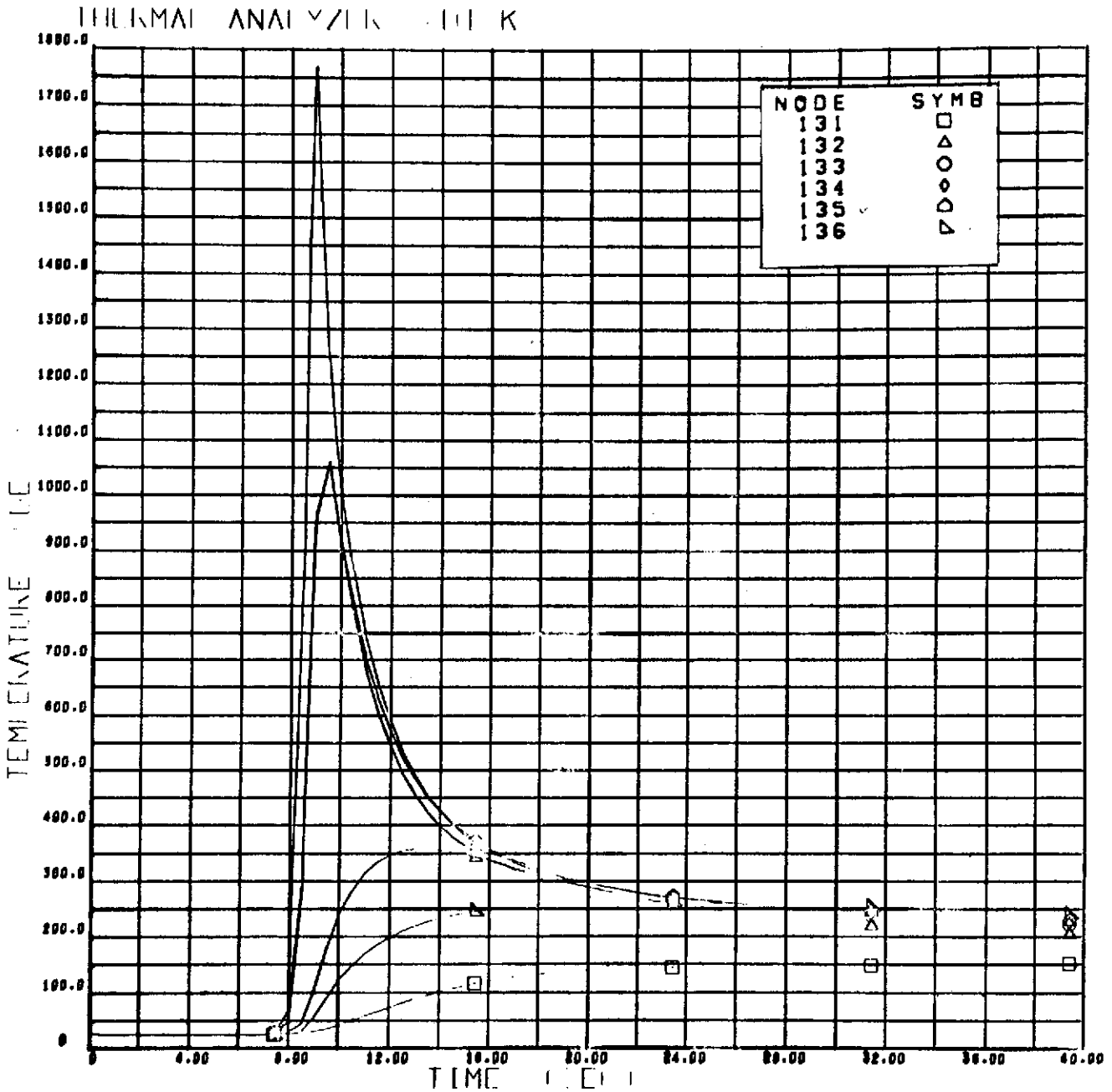

FIGURE B-14. THERMAL HISTORY FOR 0.05-INCH TANTALUM DISK (NODES 131 THROUGH 136)

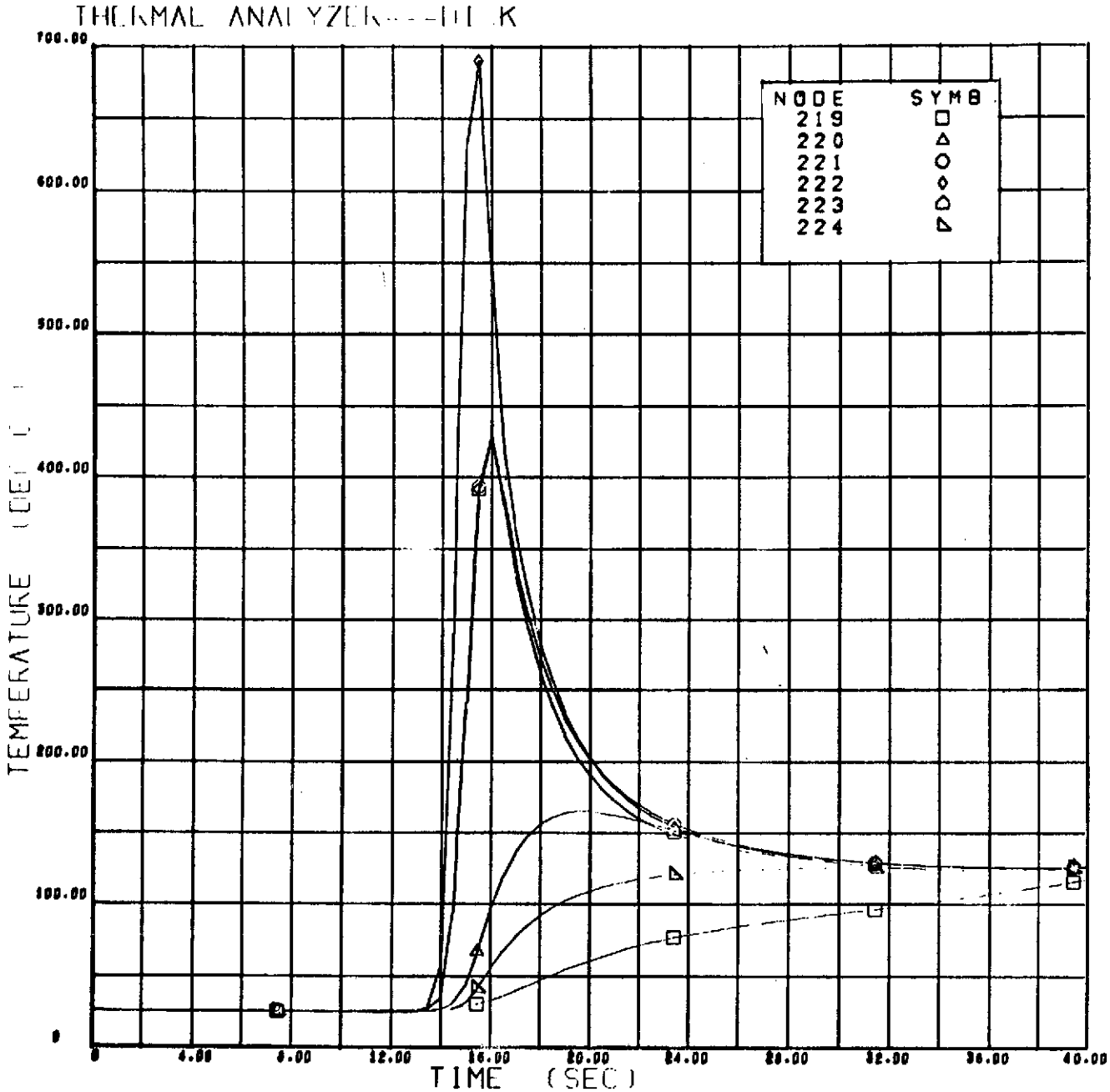

FIGURE B-15. THERMAL HISTORY FOR 0.125-INCH TANTALUM DISK (NODES 219 THROUGH 224)

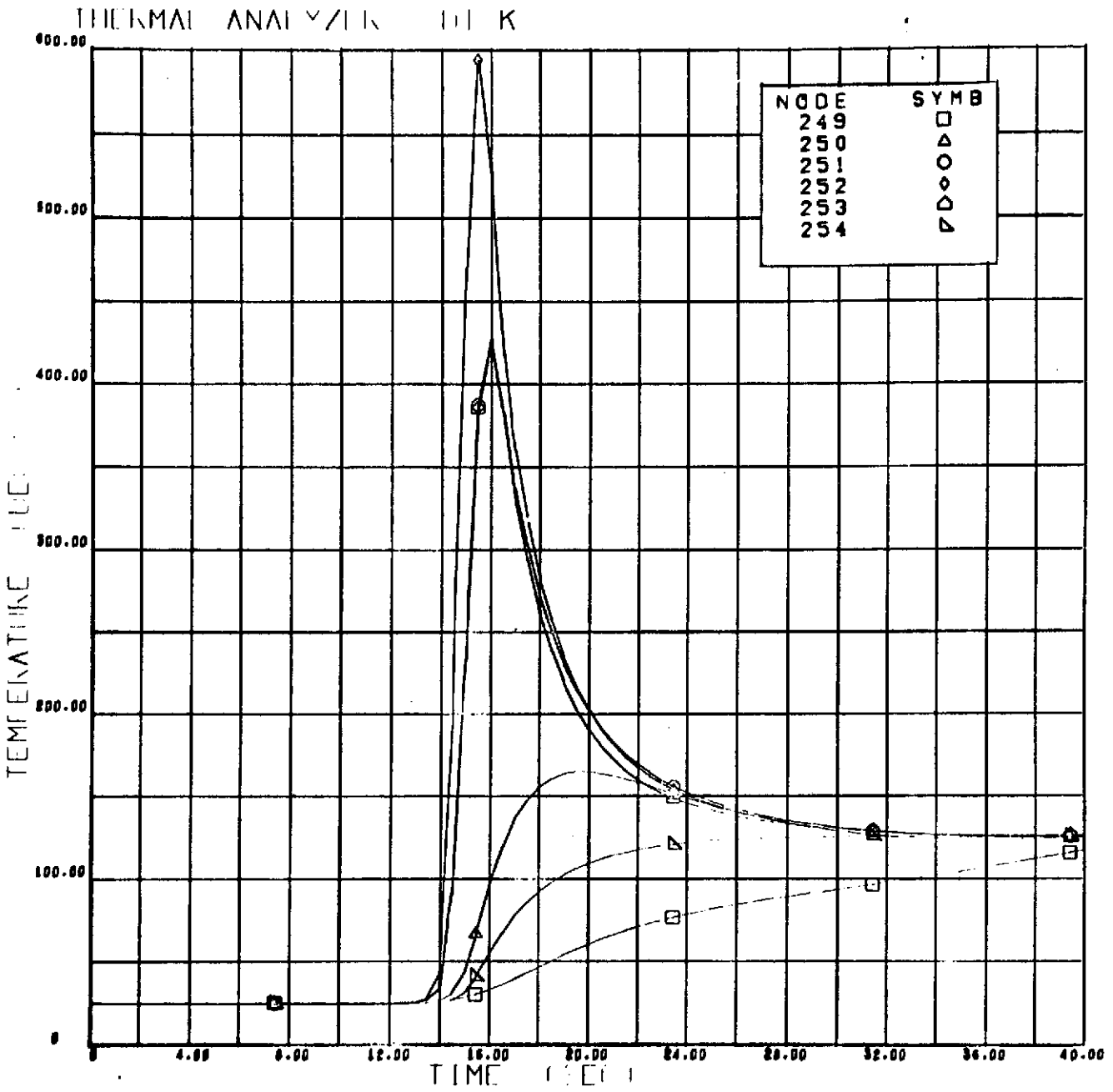

FIGURE B-16. THERMAL HISTORY FOR 0.125-INCH TANTALUM DISK (NODES 249 THROUGH 254)

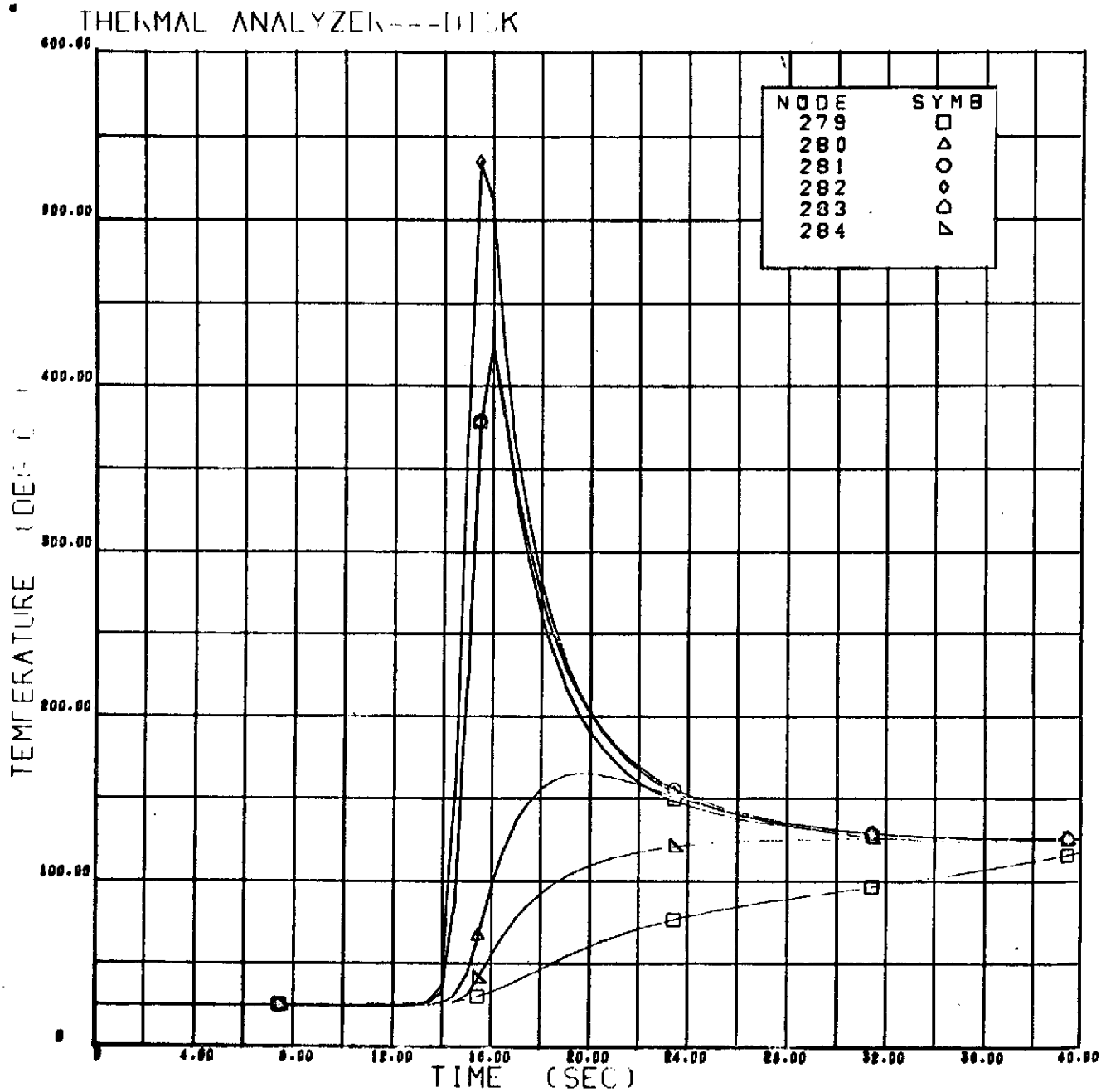

FIGURE B-17. THERMAL HISTORY FOR 0.125-INCH TANTALUM DISK (NODES 279 THROUGH 284)

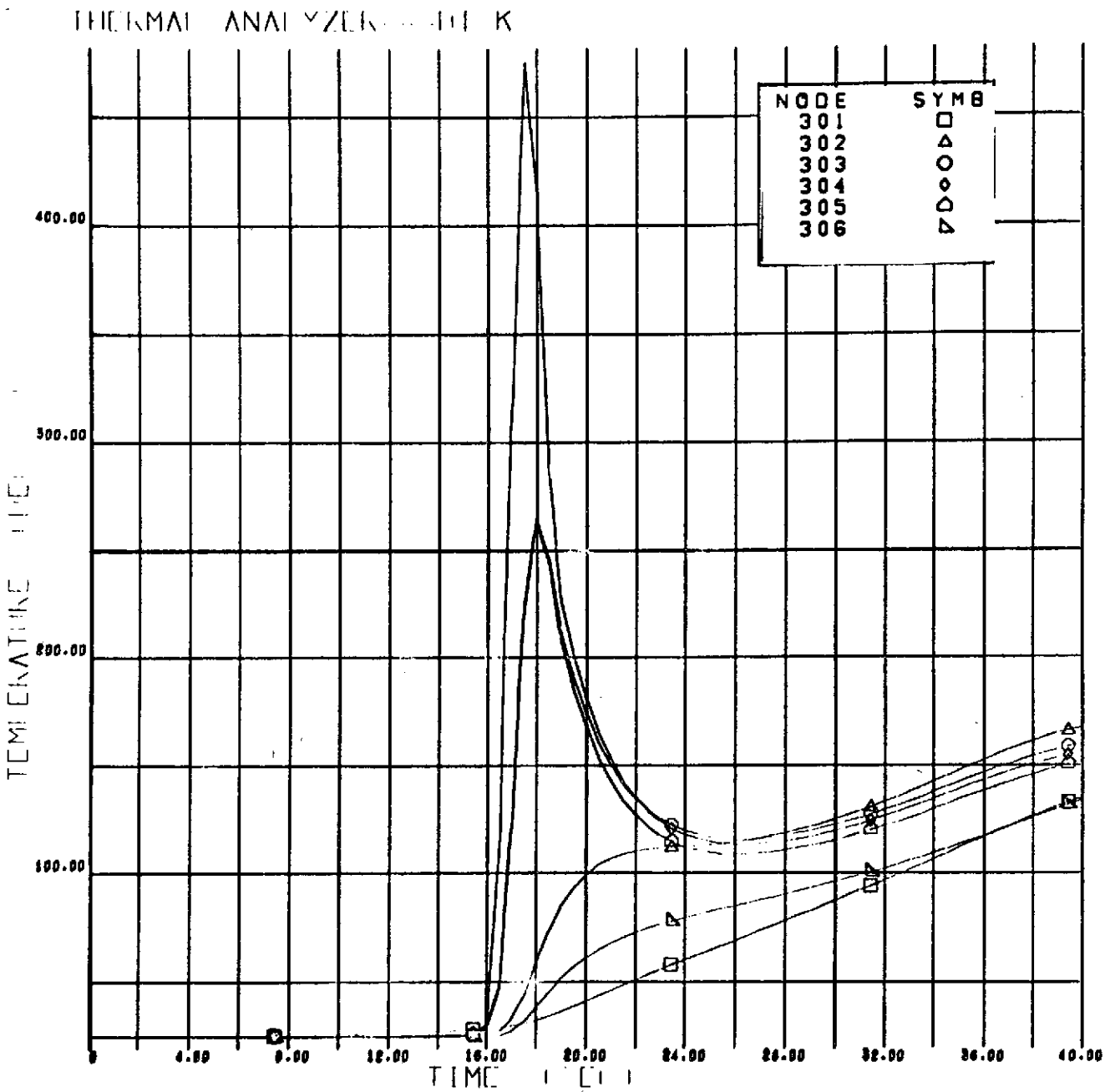

FIGURE B-18. THERMAL HISTORY FOR 0.250-INCH TANTALUM DISK (NODES 301 THROUGH 306)

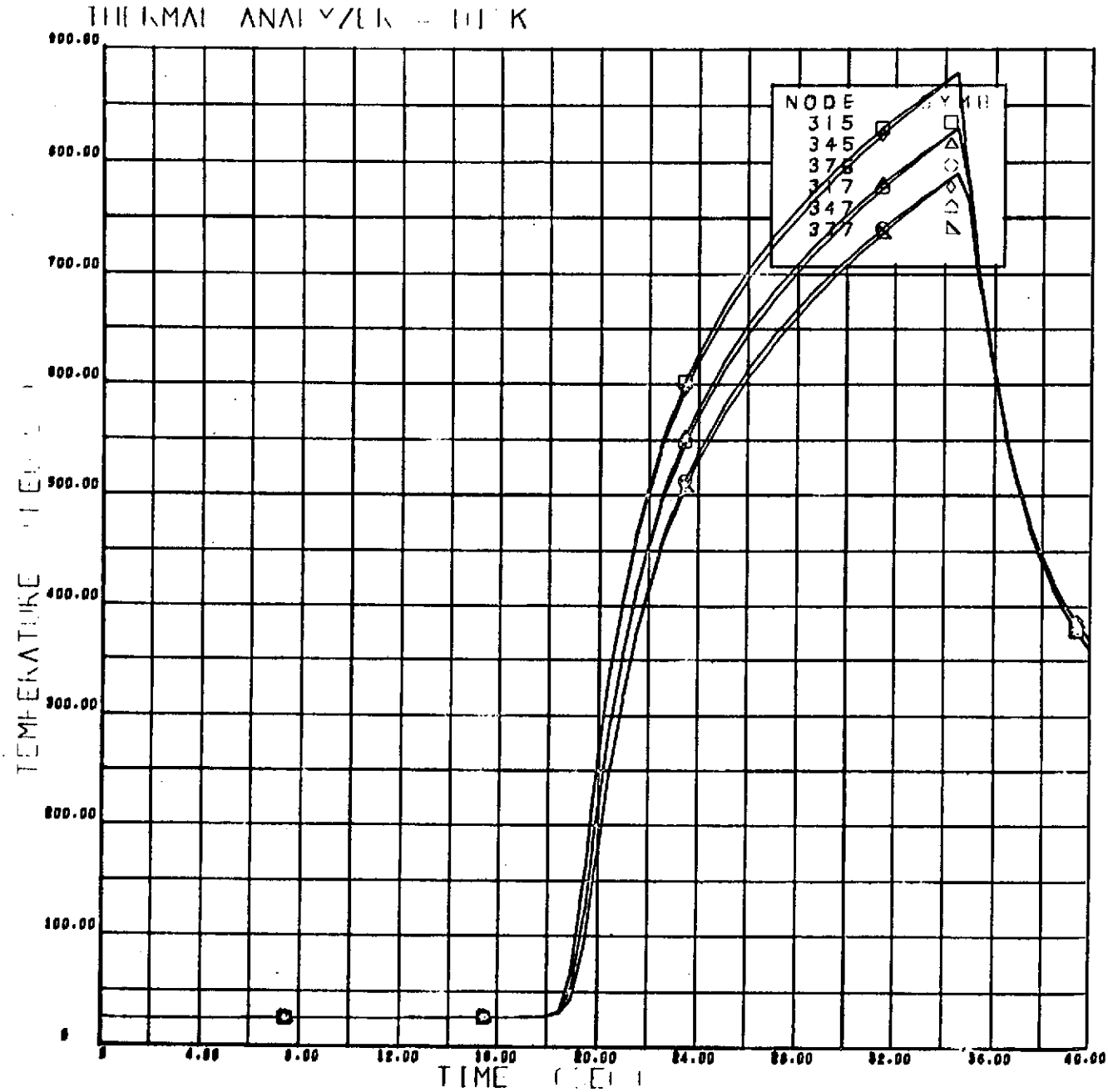

FIGURE B-19. THERMAL HISTORY FOR 0.250-INCH TANTALUM DISK (NODES 315, 345, 375, 317, 347 AND 377)

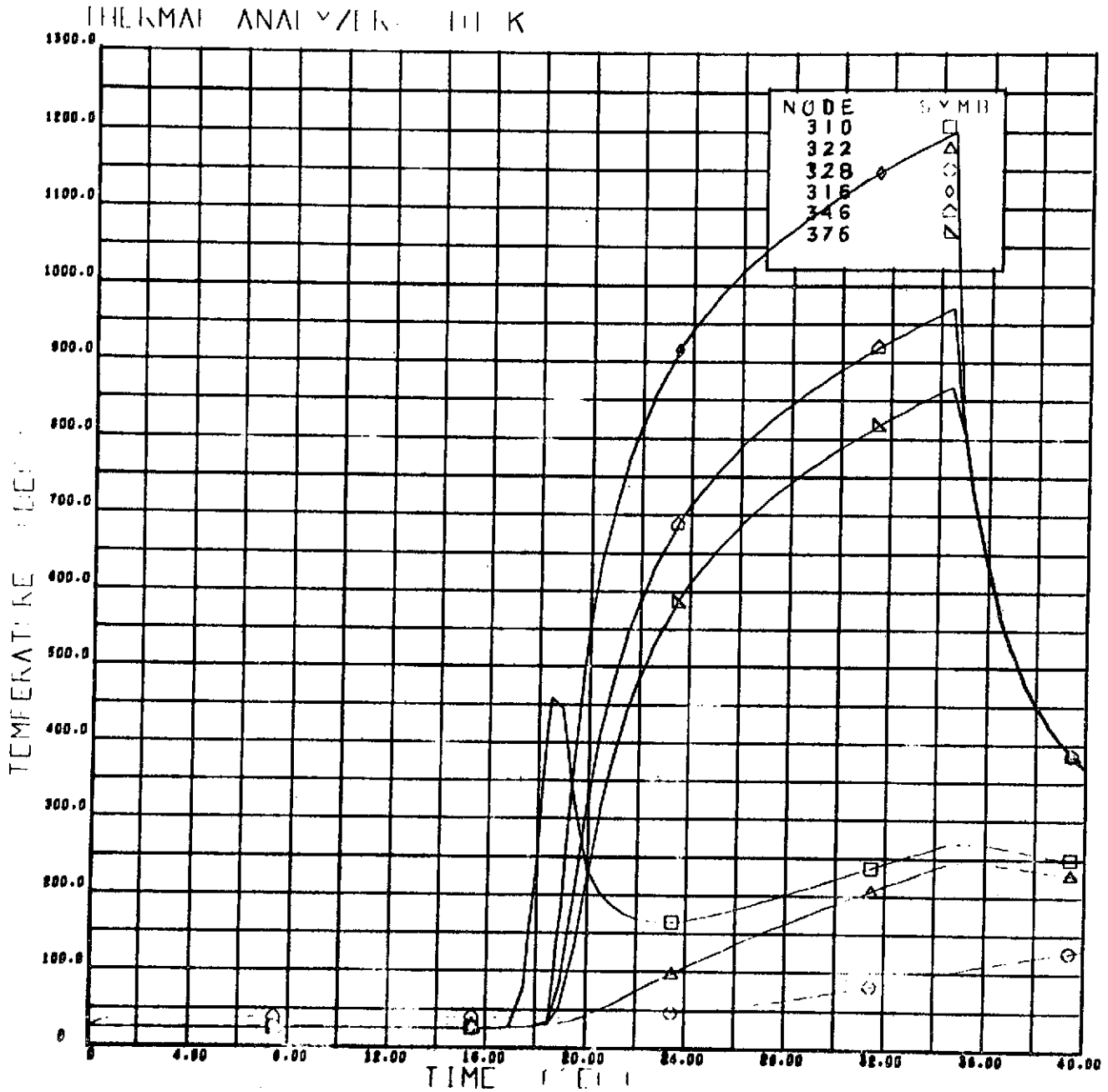

FIGURE B-20. THERMAL HISTORY FOR 0.250-INCH TANTALUM DISK (NODES 310, 322, 328, 316, 346 AND 376)